AN ABSTRACT OF THE DISSERTATION OF

Dustin Zachary Austin for the degree of Doctor of Philosophy in Electrical and Computer Engineering presented on May 19, 2017.

Title: Atomic Layer Deposition of Multi-Insulator Metal-Insulator-Metal Capacitors.

Abstract approved: ____

John F. Conley Jr.

Back end of line (BEOL) metal-insulator-metal capacitors (MIMCAPs) have become a core passive component in modern integrated circuits. International Technology Roadmap for Semiconductors (ITRS) projections for scaling of analog/mixed-signal MIMCAP applications require simultaneously increasing capacitance density while maintaining low leakage current density and low voltage nonlinearity (characterized by the quadratic voltage coefficient of capacitance, α_{VCC}). In addition to these conflicting performance requirements, BEOL processing allows for temperatures of no more than 400°C.

In this work, atomic layer deposition (ALD) of both dielectrics and metals have been investigated to develop complementary multi-insulator MIMCAPs to meet future ITRS requirements. Initially Al_2O_3/SiO_2 bilayers are assessed for targeting the ITRS 2020 node. These oxides are attractive due to their large metal-insulator barrier heights, high dielectric breakdown strength, and common usage in IC fabrication. SiO_2 is one of only a few materials to exhibit a negative α_{VCC}, which in combination with the positive α_{VCC} of Al_2O_3 enables ultra-low device α_{VCC} through the "canceling" effect. ALD for these ultra-thin insulators has become the preferred deposition method due to the inherent low deposition temperatures, precise film thickness control, and excellent film quality.

Next, to support scaling beyond the 2020 node, novel ALD processes are developed for bismuth oxide (Bi_2O_3), ruthenium oxide (RuO_2), and ruthenium metal (Ru). RuO_2 is a promising electrode material due to its high work function of ~5.1 eV and ability to template the high-κ rutile phase of TiO_2. Rutile TiO_2 is known to exhibit a negative α_{VCC} with a high-κ of ~100, which makes it a potential replacement for SiO_2 and a complementary material to Al_2O_3. Thus, using RuO_2 as the lower electrode, TiO_2/Al_2O_3 multi-insulator MIMCAPs are demonstrated to significantly enhance capacitance density while maintaining low leakage current density and relatively low α_{VCC}.

Finally, various low enthalpy of oxide formation (ΔH_{ox}) metals are investigated as a function of ALD Al_2O_3 and HfO_2 dielectric thickness (d_{ox}) to examine the mechanism of the influence from the top metal electrode on α_{VCC}, in the absence of an interfacial oxide layer. It is found for each low ΔH_{ox} metal that a different α_{ECC}, quadratic electric field coefficient of capacitance, value is measured for an otherwise identical device structure. Differences between the metals become more pronounced as the d_{ox} decreases,

which indicates an interaction at the metal/dielectric interface. To explain these differences, we propose interacting stresses due to applied bias and edge dislocations from lattice mismatch, which modulate the voltage nonlinearity. This new understanding of the impact from metal electrodes on nonlinearity should aid in rapid scaling optimization of low α_{VCC} MIMCAPs.

©Copyright by Dustin Zachary Austin

May 19, 2017

All Rights Reserved

Atomic Layer Deposition of Multi-Insulator Metal-Insulator-Metal Capacitors

by
Dustin Zachary Austin

A DISSERTATION

submitted to

Oregon State University

in partial fulfillment of
the requirements for the
degree of

Doctor of Philosophy

Presented May 19, 2017
Commencement June 2017

Doctor of Philosophy dissertation of Dustin Zachary Austin presented May 19, 2017.

APPROVED:

Major Professor, representing Electrical and Computer Engineering

Director of the School of Electrical Engineering and Computer Science

Dean of the Graduate School

I understand that my dissertation will become part of the permanent collection of Oregon State University libraries. My signature below authorizes release of my dissertation to any reader upon request.

Dustin Zachary Austin, Author

ACKNOWLEDGEMENTS

I would like to thank Dr. Conley; this dissertation would not have been possible without his support and guidance every step of the way. Also to the committee members Dr. Plant, Dr. Cheng, Dr. Cann, and Dr. Xu for their advice has been invaluable to this research. To Chris Tasker and Rick Presley, thank you for supporting all the cleanroom tools and projects that made this research possible. To Derryl Allman and the group at ON Semiconductor, thank you for the support of this project. Also, thank you to the cleanroom community past and present. Finally, my deepest appreciations go to Catharine, my parents, and sisters for their unwavering support.

CONTRIBUTION OF AUTHORS

Derryl Allman, David Price, and Sallie Hose from ON Semiconductor for supplying substrates of TaN and assistance with analytical analysis of ALD films in chapters 2, 3, and 4. Mark Saly from SAFC Hitech for development of ALD Bi precursor and TGA data in chapter 3. Chuck Dezelah from EMD Performance Materials for development of ALD Ru precursor and TGA data in chapter 4. John McGlone from Prof. John Wager's research group for AFM characterization in chapter 4. Melanie Jenkins for assistance with ALD processing in chapter 4. Michael Hayes for assistance with XRD in chapter 5. Konner Holden and Josh Hinz for processing and electrical characterization in chapter 6.

TABLE OF CONTENTS

Page

1 Introduction 1

1.1 References 7

2 Plasma Enhanced Atomic Layer Deposition of Al_2O_3/SiO_2 MIM Capacitors 11

2.1 Introduction 12

2.2 Experimental 13

2.3 Results and Discussion 14

2.4 Conclusions 18

2.5 Acknowledgments 19

2.6 References 20

3 Atomic Layer Deposition of Bismuth Oxide using $Bi(OCMe_2{}^iPr)_3$ and H_2O 22

3.1 Introduction 23

3.2 Experimental 24

3.3 Results and Discussion 25

3.3.1 Structural and Thermal Properties of $Bi(OCMe_2{}^iPr)_3$ 25

3.3.2 $Bi(OCMe_2{}^iPr)_3$ Pulse Time and Growth per Cycle 26

3.3.3 The Effect of Deposition Temperature on Bi_2O_3 Properties 28

3.3.4 Substrate Impact on Film Morphology 34

3.3.5 Impact of Annealing 35

3.4 Conclusions 36

3.5 Acknowledgments 37

3.6 References 38

4 Atomic Layer Deposition of Ruthenium and Ruthenium Oxide Using a Zero Oxidation State Precursor 41

4.1 Introduction 42

4.2 Experimental Procedure 44

4.3 Results 46

4.3.1 ALD Ru 46

4.3.2 ALD RuO_2 50

4.4 Discussion 54

4.4.1 Ru Process 54

4.4.2 RuO_2 Process 57

4.4.3 Comparing Ru and RuO_2 Processes 58

4.5 Summary and Conclusions 61

4.6 Acknowledgments 62

4.7 References 63

5 Atomic Layer Deposition of TiO_2/Al_2O_3 Metal-insulator-metal Capacitors 67

5.1 Introduction 68

5.2 Experimental 70

5.3 Results and Discussion 71

5.4 Conclusions 80

5.5 Acknowledgments 80

5.6 References 82

6 Electrode Modulated Capacitance-Electric Field Nonlinearity in Metal-Insulator-Metal Capacitors 85

6.1 Introduction 86

6.2 Experimental 87

6.2 Results and Discussion 88

6.3 Summary and Conclusions 98

6.4 Acknowledgments 100

6.5 References 101

7 Conclusion 104

7.1 References 109

LIST OF FIGURES

Figure Page

Figure 2.1: Plot of α_{VCC} for Al_2O_3 (blue squares) and $|\alpha_{VCC}|$ for SiO_2 (green diamonds) vs. film thickness (d_{ox}). Dashed lines indicate power law fits....................................... 15

Figure 2.2: Forward (blue) and reverse (green) sweeps of capacitance density vs. voltage for TaN/Al_2O_3/SiO_2/Al stacks targeting ITRS 2020. Inset: the effective dielectric constant vs. frequency for the 3.7nm/1.9nm device. 16

Figure 2.3: Current density vs. voltage sweeps for TaN/Al_2O_3/SiO_2/Al stacks targeting various ITRS nodes. The estimated thickness and number of PEALD cycles for each insulator pair are included in the legend. 17

Figure 2.4: Capacitance variation vs. positive constant voltage stress time. Inset shows plot of voltage ramped breakdown for positive and negative polarity. 18

Figure 3.1: TGA and molecular structure of $Bi(OCMe_2{}^iPr)_3$. 26

Figure 3.2: Film thickness wafer map for a 2 s pulse time of $Bi(OCMe_2{}^iPr)_3$ (measured in units of nm). 26

Figure 3.3: Bi_2O_3 film thickness (blue diamonds) and non-uniformity (red squares) as a function of $Bi(OCMe_2{}^iPr)_3$ pulse time. 27

Figure 3.4: Bi_2O_3 film thickness vs. number of cycles for a 2 s $Bi(OCMe_2{}^iPr)_3$/120 s N_2/0.1 s H_2O/120 s N_2 sequence. 28

Figure 3.5: GIXRD spectra of Bi_2O_3 films with deposition temperatures between 90 and 270°C. Dashed vertical lines indicate various peaks of Bi_2O_3 β phase (PDF: 00-027-0050). 29

Figure 3.6: (a) Extracted film thickness (blue diamonds, left axis), density (red squares, right axis), and interfacial roughness (green triangles, right axis) plotted as a function of deposition temperature. (b) XRR spectrum of Bi_2O_3 films with deposition temperatures between 90 and 270°C. 30

Figure 3.7: HRTEM of Bi_2O_3 films deposited at (a) 150°C and (b) 270°C. 31

Figure 3.8: Index of refraction vs. wavelength for Bi2O3 films with deposition temperatures between 90 and 270°C. 32

Figure 3.9: (a) Absorption coefficient (a) vs. energy and (b) band gap estimation, $(\alpha h\nu)^{1/2}$ vs. energy, of Bi_2O_3 films deposited between 90 and 270°C. 32

Figure 3.10: Elemental content obtained from RBS of Bi_2O_3 films deposited at 150°C. 34

Figure 3.11: GIXRD spectra of Bi_2O_3 films deposited on Si_3N_4, TaN, and TiN substrates. The dashed vertical line indicates (201) peak of Bi_2O_3 β phase (PDF: 00-027-0050). 35

Figure 3.12: GIXRD spectra of as-deposited and annealed Bi_2O_3 films. Dashed vertical blue line indicates Bi_2O_3 β phase (PDF: 00-027-0050); solid vertical black lines indicate Bi_2O_3 α phase (PDF: 01-071-0465)....36

Figure 3.13: HRTEM of 450°C annealed Bi_2O_3....36

Figure 4.1: (a) Vapor pressure vs. temperature for $Ru(DMBD)(CO)_3$ with the inset showing molecular structure. (b) TGA % weight remaining vs. temperature and derivative for $Ru(DMBD)(CO)_3$....45

Figure 4.2: Film thickness and resistivity vs. deposition temperature for ALD Ru metal. 47

Figure 4.3: Film thickness vs. (a) $Ru(DMBD)(CO)_3$ pulse time and (b) O_2 pulse time for ALD Ru metal....48

Figure 4.4: Film thickness vs. the number of ALD cycles for ALD Ru metal....48

Figure 4.5: High-resolution XPS spectrum of Ru $3d_{5/2}$ and Ru $3d_{3/2}$ ionizations for ALD Ru metal film with an inset of high-resolution AES regions for C KLL and Ru MNN....49

Figure 4.6: GIXRD plot of log intensity vs. 2θ for an 8 nm thick ALD Ru metal film deposited at 320°C with a reference card pattern overlay....50

Figure 4.7: AFM surface roughness measurements of an 8 nm thick ALD Ru metal film deposited at 320°C....50

Figure 4.8: Film thickness and resistivity vs. deposition temperature for (a) thermal ALD and (b) PEALD of RuO_2....51

Figure 4.9: (a) $Ru(DMBD)(CO)_3$ pulse time saturation curve for thermal ALD (green squares) and PEALD (blue triangles) of RuO_2 and (b) O_2 pulse time saturation curve for thermal ALD of RuO_2....52

Figure 4.10: Film thickness vs. the number of ALD cycles for thermal ALD (green squares) and PEALD (blue triangles) of RuO_2....52

Figure 4.11: High-resolution XPS spectrum of Ru $3d_{5/2}$ and Ru $3d_{3/2}$ ionizations of an ALD RuO_2 film with an inset of the high-resolution AES region for C KLL and Ru MNN....53

Figure 4.12: GIXRD plots of log intensity vs. 2θ for 12 nm thick RuO_2 films via thermal ALD (green squares) and PEALD (blue triangles) deposited at 240 and 230°C, respectively....54

Figure 4.13: AFM images of 12 nm thick (a) thermal ALD and (b) PEALD RuO_2 films deposited at 240 and 230°C, respectively....54

Figure 4.14: Comparison of GPC and resistivity vs. temperature for Ru and RuO_2 thermal ALD processes. The 20 s O_2 pulses are shown as green circles (GPC) and green triangles (resistivity) and the 2 s O_2 pulses as orange squares (GPC) and orange diamonds (resistivity)....60

Figure 5.1: GIXRD of annealed 400 cycle TiO_2 on either (a) TaN or (b) RuO_2 lower electrodes, with reference spectra included for each metal. 73

Figure 5.2: (a) Capacitance density vs. voltage and (b) Leakage current density vs. electric field for 400 PEALD cycles of annealed TiO_2 on either RuO_2 or TaN lower electrodes. 74

Figure 5.3: (a) Capacitance density vs. voltage for bi-layer stacks of TiO_2/Al_2O_3 with varying Al_2O_3 thicknesses and (b) Normalized capacitance (β_{VCC} removed) of the 400c/70c device clearly illustrating the 'w' curvature. 76

Figure 5.4: Leakage current density vs. voltage for bi-layer stacks of TiO_2/Al_2O_3 on RuO_2 lower electrodes. 77

Figure 5.5: Capacitance density vs. voltage for the same TiO_2/Al_2O_3 (400 cycles / 75 cycles) device tested on the same day as deposition and again after two weeks. 79

Figure 5.6: GIXRD of 400c/75c TiO_2/Al_2O_3 with device test same day as deposition and 2 weeks later. 79

Figure 6.1: Baseline adjusted (β term removed) normalized capacitance density vs. (a) voltage and (b) electric field for various thickness Al_2O_3 devices with ~320 nm Ag top contacts. 89

Figure 6.2: CET (zero-bias) versus measured optical thickness for TaN/Al_2O_3/Ag devices. 90

Figure 6.3: α_{ECC} versus dielectric film thickness for ALD (a) Al_2O_3 and (b) HfO_2 with various ~320 nm thick low ΔH_{ox} metal electrodes. 91

Figure 6.4: Normalized capacitance and calculated decrease in dielectric film thickness vs. electric field for (a) 10 nm Al_2O_3 and (b) 11 nm HfO_2 with various ~320 nm thick low ΔH_{ox} top metal electrodes. 92

Figure 6.5: Cross sectional schematic illustrating elastic deformation (exaggerated) as result of applied bias to a positive α_{VCC} (α_{ECC}) dielectric. Dashed blue lines represent lateral expansion of the dielectric. 94

Figure 6.6: Schematic of residual stress and edge dislocations at a metal-oxide interface due to lattice mismatch. 96

Figure 6.7: α_{ECC} vs. lattice mismatch for Al_2O_3 and HfO_2 with various top metal electrodes. 97

LIST OF TABLES

Table Page

Table 2.1: Comparison of Al_2O_3/SiO_2 Stacks Meeting Incremental ITRS Nodes 17

Table 2.2: Comparison of Low Voltage Nonlinearity MIIM Capacitors 18

Table 3.1: Tabulated Values for Optical and Physical Properties of Bi_2O_3 films. 33

Table 4.1: Comparison of Ruthenium Precursors for Thermal ALD Ru Processes Using O_2 as a Co-Reactant 56

Table 4.2: Comparison of Ruthenium Precursors for RuO_2 58

Table 5.1: Summary of Devices Measurements 77

Table 5.2: TiO_2/Al_2O_3 Stability 79

Table 6.1: f, α_{ECC}, and ΔH_{ox} for Al_2O_3 and HfO_2 for Various Metals Electrodes. 97

1 INTRODUCTION

Metal-insulator-metal capacitors (MIMCAPs) are fundamental back-end-of-line (BEOL) devices for analog and mixed signal (AMS) applications including analog-to-digital converters, analog noise filters, DC voltage decoupling, and electrostatic discharge (ESD) protection, to name a few. Projected device requirements are given by the International Technology Roadmap for Semiconductors (ITRS), which suggests scaling of AMS MIMCAPs necessitates an increased capacitance density (C) while simultaneously maintaining low leakage current density (J) and low voltage nonlinearity (characterized by the quadratic voltage coefficient of capacitance, α_{VCC}).[1] The α_{VCC} is empirically determined by fitting a parabolic expression to the capacitance versus voltage measurement:

$$\Delta C/C_0 = \alpha_{VCC} V^2 + \beta_{VCC} V, \tag{1.1}$$

where C_0 is the capacitance density at 0 V, $\Delta C = C(V) - C_0$ is the change in capacitance at a given applied bias, and β_{VCC} is the linear voltage coefficient of capacitance. C_0 is characterized by the parallel plate capacitor equation, $C_0 = \frac{\varepsilon_0 \kappa}{d_{ox}}$, where ε_0 is the permittivity of vacuum, κ is the dielectric constant, and d_{ox} is the dielectric thickness. Additionally, BEOL processing requires temperatures of no more than 400ºC.[2]

Increased C_0 can be achieved by two primary methods of either reducing the d_{ox} or changing the insulator to a high-κ material. However, neither option is ideal, as both typically result in increased J and increased α_{VCC}. In the first method, reducing the d_{ox} in ultra-thin films significantly increases the electric field (E) for a given voltage, and results in high J from reduced tunneling distances as well as increased α_{VCC} from a d_{ox}^{-2} dependence.[3–5] Then in the second method, high-κ dielectrics typically exhibit a large

density of oxygen vacancies, small bandgap, and small barrier height, which increases conduction thermally over a small barrier or through trap sites in the bulk.[6,7] Additionally, α_{VCC} has a linear relationship with κ, which results in high-κ MIMCAPS exhibiting relatively large α_{VCC}.[3,8] As result of these competing requirements, single insulator devices are unable to simultaneously meet all three performance projections for future ITRS nodes.[5,9,10]

One successful approach for simultaneously meeting these competing requirements is to use multiple insulators with complementary material properties, each targeting one or more device attributes.[5,11–16] Using this approach, increased C with low J can be obtained while enabling minimization of α_{VCC} through the "cancelling effect".[11] The cancelling technique uses two or more dielectrics in a stack with opposing sign α_{VCC}. The overall device nonlinearity may be minimized by carefully controlling the thickness of each dielectric layer so that their individual contributions to α_{VCC} cancel one another.

In this work, atomic layer deposition (ALD) of both dielectrics and metals have been investigated to develop complementary multi-insulator stacks to meet future ITRS requirements. ALD for these ultra-thin insulators has become the preferred deposition method due to the inherent low deposition temperatures, precise film thickness control, and excellent film quality, which is critical for optimizing the α_{VCC} via the cancelling effect. In chapter 2, the cancelling effect is implemented with complementary bilayer stacks of ultra-thin PEALD Al_2O_3/SiO_2 MIMCAPs.[5] These oxides are attractive due to their large metal-insulator barrier heights, high dielectric breakdown strength, and common usage in IC fabrication. SiO_2 is a recently developed plasma enhanced atomic layer deposition (PEALD) process[17] and is one of the few materials to exhibit a negative

α_{VCC},[18] which in combination with the positive α_{VCC} of Al_2O_3 enables ultra-low device α_{VCC} through the "canceling" effect. However, the scaling limit for this stack, via d_{ox} reduction, is determined to be the IRTS 2020 node, which leads to a need for replacement complementary high-κ dielectrics and high work function metals to increase C while maintaining low J and low α_{VCC}.

Therefore, to support scaling beyond the 2020 node, novel ALD processes are developed for bismuth oxide (Bi_2O_3) via Bi(dimethyl-methylpropoxide)$_3$ [Bi(OCMe$_2$^{i}Pr)$_3$] precursor,[19] as well as ruthenium metal (Ru) and ruthenium oxide (RuO_2) via η^4-2,3-dimethylbutadiene ruthenium tricarbonyl [Ru(DMBD)(CO)$_3$] precursor,[20] characterized in chapters 3 and 4, respectively. Bi_2O_3 has potential use in multi-component high-κ dielectrics such as $BiTaO_4$ or $Bi_2Ti_2O_7$, which exhibit κ of ~45.[21–23] Then, Ru metal and RuO_2 are promising electrode materials due to their high work functions of 4.7 eV and 5.1 eV as well as low bulk resistivity of 7.1 μΩ·cm and 46 μΩ·cm, respectively.[24–27] Additionally, RuO_2 is a conductive oxide which is less likely to form an interfacial layer oxide (ILO) during ALD than commonly used TaN or TiN electrodes.

In chapter 5, rutile RuO_2 has been found to aid in obtaining the high-κ rutile phase of TiO_2 at lower deposition temperatures by possibly templating the initial stages of growth.[25–27] Rutile TiO_2 exhibits a negative α_{VCC} with a high-κ of 89, which makes it a potential replacement for SiO_2 and a complementary material to Al_2O_3. Therefore, improving on the initial Al_2O_3/SiO_2 bilayers, complementary multi-insulator MIMCAPs of TiO_2/Al_2O_3 using rutile RuO_2 lower electrodes are developed. Bi-layer devices are found to meet C_0 and J for ITRS 2024 node, but due to a higher order polynomial fit, “w”

shape, the capacitance versus voltage sweep exceeds the α_{VCC} requirement. Additionally, a capacitance instability is measured likely due to an instability in the TiO_2 morphology but found to meet ITRS 2020 node after stabilizing to a lower C_0.

Finally, to examine the mechanism of the influence from the top metal electrode on α_{VCC}, in the absence of an ILO, various low enthalpy of oxide formation (ΔH_{ox}) metals are investigated as a function of d_{ox} with ALD Al_2O_3 and HfO_2, in chapter 6. It is found for each low ΔH_{ox} metal that a different α_{ECC}, quadratic electric field coefficient of capacitance, value is measured for an otherwise identical device structure. Ag exhibits the lowest α_{ECC}, followed in increasing order by Au, Pd, and Ni. Additionally, the difference between these metals becomes more pronounced as the d_{ox} decreases, which indicates an interaction at the interface between the metal and dielectric. Current models of nonlinearity consider only the influence of the "bulk" dielectric and any ILOs that may be present.[3,4,6,28–36] They typically do not focus on the direct influence of the electrodes. Thus, to explain these differences in positive α_{VCC} materials, we propose a theory that considers the physical properties of metal/dielectric interface. As result of applied bias, a vertical compression of the dielectric induces an expansion in-plane of the dielectric to maintain volume, but is restricted by the metal electrodes and causes a stress concentrated near the interface.[37–39] However, interfaces with larger lattice mismatch contain a greater density of edge dislocations that provide increased localized stress relief, which results in a greater cumulative reduction in global interfacial stress and allows for increased lateral expansion of the dielectric under applied bias.[40,41] Therefore, a trend is measured that correlates well for a lattice-mismatch-dependent voltage nonlinearity, in the absence of

an ILO. This new understanding of the impact from metal electrodes on nonlinearity should aid in rapid scaling optimization of low α_{VCC} MIMCAPs.

1.1 References

[1] The International Technology Roadmap for Semiconductors (ITRS), On-Chip Passives Technology Requirements (Semiconductor Industry Association, 2013).

[2] A. Farcy, J.-F. Carpentier, M. Thomas, J. Torres, and P. Ancey, Microelectron. Eng. 85, 1940 (2008).

[3] C. Wenger, G. Lupina, M. Lukosius, O. Seifarth, H.-J. Müssig, S. Pasko, and C. Lohe, J. Appl. Phys. 103, 104103 (2008).

[4] S. Bécu, S. Crémer, and J.-L. Autran, Appl. Phys. Lett. 88, 052902 (2006).

[5] D.Z. Austin, D. Allman, D. Price, S. Hose, and J.F. Conley Jr., IEEE Electron Device Lett. 36, 496 (2015).

[6] P. Gonon and C. Vallée, Appl. Phys. Lett. 90, 142906 (2007).

[7] T. Tung, Appl. Phys. Rev. 1, 011304 (2014).

[8] M.D. Groner, J.W. Elam, F.H. Fabreguette, and S.M. George, Thin Solid Films 413, 186 (2002).

[9] X. Yu, C. Zhu, H. Hu, A. Chin, M.F. Li, B.J. Cho, D.-L. Kwong, P.D. Foo, and M.B. Yu, IEEE Electron Device Lett. 24, 63 (2003).

[10] S.-Y. Lee, H. Kim, P.C. McIntyre, K.C. Saraswat, and J.-S. Byun, Appl. Phys. Lett. 82, 2874 (2003).

[11] S.J. Kim, B.J. Cho, M.-F. Li, S.-J. Ding, C. Zhu, M.B. Yu, B. Narayanan, A. Chin, and D.-L. Kwong, IEEE Electron Device Lett. 25, 538 (2004).

[12] J.-J. Yang, J.-D. Chen, R. Wise, P. Steinmann, Y.-C. Yeo, and C. Zhu, IEEE Electron Device Lett. 30, 1033 (2009).

[13] T.H. Phung, D.K. Srinivasan, P. Steinmann, R. Wise, M.-B. Yu, Y.-C. Yeo, and C. Zhu, J. Electrochem. Soc. 158, H1289 (2011).

[14] J.H. Lee, Y.C. Lin, B.H. Chen, and C.Y. Tsai, in Solid-State Integr. Circuit Technol. ICSICT 2010 10th IEEE Int. Conf. On (IEEE, 2010), pp. 1024–1026.

[15] C.-C. Lin, Y.-H. Wu, R.-S. Jiang, and M.-T. Yu, IEEE Electron Device Lett. 34, 1418 (2013).

[16] S.-U. Park, C.-Y. Kang, H.-M. Kwon, B.-S. Park, W.-H. Choi, I.-S. Han, G. Bersuker, R. Jammy, and H.-D. Lee, Microelectron. Eng. 88, 3389 (2011).

[17] G. Dingemans, C. Van Helvoirt, M.C.M. Van de Sanden, and W.M. Kessels, in (2011), pp. 191–204.

[18] S. Van Huylenbroeck, S. Decoutere, R. Venegas, S. Jenei, and G. Winderickx, Electron Device Lett. IEEE 23, 191 (2002).

[19] D.Z. Austin, D. Allman, D. Price, S. Hose, M. Saly, and J.F. Conley Jr., J. Vac. Sci. Technol. Vac. Surf. Films 32, 01A113 (2014).

[20] D.Z. Austin, M.A. Jenkins, D. Allman, S. Hose, D. Price, C.L. Dezelah, and J.F. Conley Jr., Chem. Mater. 29, 1107 (2017).

[21] L. Goux and D.J. Wouters, J. Appl. Phys. 100, 126103 (2006).

[22] L. Goux, H. Vander Meeren, and D.J. Wouters, J. Electrochem. Soc. 153, F132 (2006).

[23] G.W. Hwang, W.D. Kim, Y.-S. Min, Y.J. Cho, and C.S. Hwang, J. Electrochem. Soc. 153, F20 (2006).

[24] M.W. Lane, C.E. Murray, F.R. McFeely, P.M. Vereecken, and R. Rosenberg, Appl. Phys. Lett. 83, 2330 (2003).

[25] J.H. Han, S. Han, W. Lee, S.W. Lee, S.K. Kim, J. Gatineau, C. Dussarrat, and C.S. Hwang, Appl. Phys. Lett. 99, 022901 (2011).

[26] B. Hudec, K. Hušeková, E. Dobročka, J. Aarik, R. Rammula, A. Kasikov, A. Tarre, A. Vincze, and K. Fröhlich, J. Vac. Sci. Technol. B Microelectron. Nanometer Struct. 29, 01AC09 (2011).

[27] K. Frohlich, B. Hudec, M. Tapajna, K. Husekova, A. Rosova, P. Elias, J. Aarik, R. Rammula, A. Kasikov, T. Arroval, L. Aarik, K. Murakami, M. Rommel, and A.J. Bauer, ECS Trans. 50, 79 (2013).

[28] S. Blonkowski, Appl. Phys. Lett. 91, 172903 (2007).

[29] F. El Kamel, P. Gonon, and C. Vallée, Appl. Phys. Lett. 91, 172909 (2007).

[30] C. Vallée, P. Gonon, C. Jorel, and F. El Kamel, Appl. Phys. Lett. 96, 233504 (2010).

[31] S. Blonkowski, M. Regache, and A. Halimaoui, J. Appl. Phys. 90, 1501 (2001).

[32] S. Bécu, S. Crémer, and J.L. Autran, Microelectron. Eng. 83, 2422 (2006).

[33] C. Wenger, M. Lukosius, G. Weidner, H.-J. Müssig, S. Pasko, and C. Lohe, Thin Solid Films 517, 6334 (2009).

[34] C. Wenger, M. Lukosius, H.-J. Müssig, G. Ruhl, S. Pasko, and C. Lohe, J. Vac. Sci. Technol. B Microelectron. Nanometer Struct. 27, 286 (2009).

[35] T.H. Phung, P. Steinmann, R. Wise, Y.-C. Yeo, and C. Zhu, IEEE Electron Device Lett. 32, 1671 (2011).

[36] S.D. Park, C. Park, D.C. Gilmer, H.K. Park, C.Y. Kang, K.Y. Lim, C. Burham, J. Barnett, P.D. Kirsch, H.H. Tseng, R. Jammy, and G.Y. Yeom, Appl. Phys. Lett. 95, 022905 (2009).

[37] C.T. Campbell, Surf. Sci. Rep. 27, 1 (1997).

[38] T. Vreeland, A. Dommann, C.-J. Tsai, and M.-A. Nicolet, MRS Proc. 130, (1988).

[39] W.D. Callister, Materials Science and Engineering: An Introduction, 7th ed (John Wiley & Sons, New York, 2007).

[40] J.E. Ayers, T. Kujofsa, P. Rango, and J.E. Raphael, Heteroepitaxy of Semiconductors: Theory, Growth, and Characterization, Second edition (CRC Press/Taylor & Francis Group, Boca Raton, 2017).

[41] M. Liu, H. Ruan, L. Zhang, and A. Moridi, J. Mater. Res. 27, 2737 (2012).

2 PLASMA ENHANCED ATOMIC LAYER DEPOSITION OF Al_2O_3/SiO_2 MIM CAPACITORS

Dustin Z. Austin, Derryl Allman, David Price, Sallie Hose, and John F. Conley, Jr.

IEEE Electron Device Letters 36, 496-498 (2015)

2.1 Introduction

Back end of line (BEOL) metal-insulator-metal capacitors (MIMCAPs) reduce the need for discrete off-board components and have become core passive devices in integrated circuits (IC). Applications of MIMCAPs include analog-to-digital converters, analog noise filters, DC voltage decoupling, and electrostatic discharge protection. According to the 2020 node of the International Technology Roadmap for Semiconductors (ITRS), scaling the area of these devices for analog/mixed-signal ICs will require increasing capacitance density (to greater than 10 fF/μm^2) while simultaneously maintaining low voltage nonlinearity (less than 100 ppm/V^2, characterized by the quadratic voltage coefficient of capacitance, α_{VCC}) and low leakage current density (less than 10 nA/cm^2 at 1V).[1] In addition to these conflicting performance requirements, BEOL processing allows for temperatures of no more than 400ºC.[2]

Increasing capacitance density may be achieved either by decreasing the insulator film thickness or by introducing high dielectric constant (κ) materials. Simply decreasing the insulator film thickness leads to increased tunneling leakage as well as increased voltage nonlinearity.[3,4] On the other hand, most high-κ insulators also have drawbacks such as large positive α_{VCC}, small metal-insulator barrier heights, and increased conduction through defect levels.[5] Thus, single insulator devices have been unable to simultaneously meet all three performance projections of future ITRS nodes. A promising approach to meeting all of these competing performance needs is to use multi-layer insulator stacks to combine materials with complementary properties (e.g. a high-κ, positive α_{VCC} insulator with a low leakage, negative α_{VCC} insulator).[6-12] Previous reports of multi-insulator structures that meet or come close to meeting upcoming ITRS

projections are listed in Table 2.2. Note however that these previous studies employ either complex or uncommon materials, break vacuum between insulating layers, or are processed outside the specified BEOL temperature limit.

In the present work, Al_2O_3/SiO_2 bilayers are investigated for potential use in BEOL RF MIMCAPs. Al_2O_3 and SiO_2 are attractive due to their large metal-insulator barrier heights, high dielectric breakdown strength, and common usage in IC fabrication. In addition, SiO_2 is one of the few materials to exhibit a negative α_{VCC} and thus can be used in combination with the positive α_{VCC} of Al_2O_3 to target ultra-low device voltage nonlinearity through α_{VCC} canceling.[7] Plasma enhanced atomic layer deposition (PEALD) is used to deposit high quality pin-hole free nanolaminate Al_2O_3/SiO_2 stacks at low temperature without breaking vacuum. The self-limiting reactions of PEALD enable precise control over film thickness, which is critical for optimizing the α_{VCC} cancelling effect for ultra-thin films. The capacitance density, leakage current density, and α_{VCC} of Al_2O_3/SiO_2 MIIMCAPs are benchmarked against future ITRS projections.

2.2 Experimental

$Si/SiO_2/Ta/TaN$ substrates with the SiO_2 layer planarized via chemical mechanical polishing were used as the bottom electrodes. PEALD of Al_2O_3 and SiO_2 was performed at 200°C in a Picosun SUNALE R-200 reactor using alternating N_2-purge-separated pulses of O_2 and either trimethylaluminum (TMA) or bis(diethylamino)silane (BDEAS), respectively. TMA was held at 17°C and BDEAS held at 55°C. The deposition rates of Al_2O_3 and SiO_2 were approximately 0.10 nm/cycle and 0.11 nm/cycle, respectively. The Al_2O_3 layer was always deposited first. 250 µm diameter evaporated Al dot top contacts with areas of ~0.05 mm^2 were defined via shadow mask. The area of

each device was measured and used for area normalizations. The average error in the area measurement is found to be +/- 1.8%. Film thickness of select samples was measured using either an FEI Tecnai F20 high-resolution transmission electron microscope (TEM) or a J.A. Woollam M2000 spectroscopic ellipsometer. 100 kHz capacitance vs. voltage (CV) measurements were conducted using an Agilent E4980. Current vs. voltage (IV) measurements were taken using an Agilent B1500A. All electrical tests were conducted with the bottom electrode held at ground and performed in the dark at a controlled 25°C. CV measurements were swept to approximately one-half breakdown voltage to avoid excessive stress during testing. To reduce displacement current, CV and IV measurements were performed at sweep rates of 0.2 V/s.

2.3 Results and Discussion

The voltage nonlinearity of MIMCAPs can be described by the quadratic equation, $\Delta C/C0 = \alpha_{VCC} V^2 + \beta_{VCC} V$. Shown in Fig. 2.1, the α_{VCC} for Al_2O_3 and $|\alpha_{VCC}|$ for SiO_2 are plotted together as a function of single layer insulator thickness. A simple power law was found to fit well the thickness dependence of α_{VCC}. Combining the power law fits with the capacitive voltage divider equation, approximate layer thicknesses were estimated for Al_2O_3/SiO_2 bilayers that simultaneously meet ITRS projections for capacitance density and α_{VCC}.

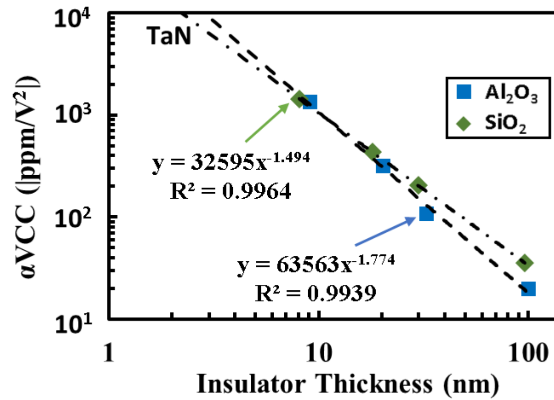

Figure 2.1: Plot of α_{VCC} for Al_2O_3 (blue squares) and $|\alpha_{VCC}|$ for SiO_2 (green diamonds) vs. film thickness (d_{ox}). Dashed lines indicate power law fits.

Shown in Fig. 2.2 are forward/reverse capacitance density vs. voltage sweeps for MIIM devices with 40c of Al_2O_3 and either 13c, 15c, or 17c of SiO_2, where "c" represents the number of PEALD cycles. As the difference in thickness between these ultra-thin film stacks is difficult to measure accurately, the number of PEALD cycles is used for identification. The 40c/17c Al_2O_3/SiO_2 MIIM devices (measured via TEM to be approximately 3.7 nm / 1.9 nm) were found to meet the ITRS 2020 projection for capacitance density with 10.1 fF/μm^2 and a minimized α_{VCC} of -20 ppm/V^2. Note that optimized α_{VCC} values are not exactly as predicted by simple theory which considers only "bulk" α_{VCC} mechanisms.[7] α_{VCC} mechanisms are not well understood[4] and the discrepancy is likely due to contributions of secondary nonlinearity mechanisms[12] such as electrode effects.[13,14] As shown in the inset, the effective dielectric constant of these devices shows little frequency dependence up to 1 MHz. A slight negative β can be observed for all of these devices, which might be attributed to the electrode work function difference. The thickness control of PEALD is a clear advantage for minimizing α_{VCC}. As seen in Fig. 2.2, the difference between the device with 300 ppm/V^2 (40c/15c) and the device with -20 ppm/V^2 (40c/17c), was only 2 PEALD cycles of SiO_2.

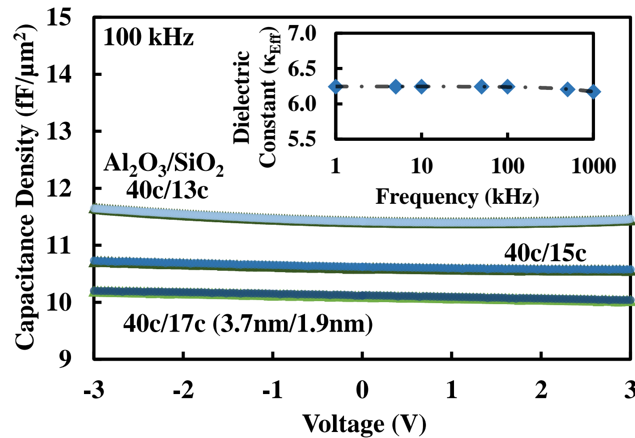

Figure 2.2: Forward (blue) and reverse (green) sweeps of capacitance density vs. voltage for TaN/Al_2O_3/SiO_2/Al stacks targeting ITRS 2020. Inset: the effective dielectric constant vs. frequency for the 3.7nm/1.9nm device.

Current density vs. voltage sweeps for Al_2O_3/SiO_2 stacks targeting future ITRS nodes are shown Fig. 2.3. The small asymmetry seen between positive and negative polarity likely arises from (i) the work function difference of Al (4.2 eV) vs. TaN (4.6 eV) electrodes and (ii) the presence of deep level defects in the SiO_2 which may enable trap-assisted-tunneling at low bias.[5] The intersection between the vertical and horizontal dashed lines indicates the ITRS maximum leakage limit of 10 nA/cm^2 at 1V. Results are summarized in Table 2.1. The 3.7 nm / 1.9 nm (40c/17c) Al_2O_3/SiO_2 device meets all ITRS 2020 projections with a low α_{VCC}/C_{ox}^2 of 0.2 µm^4/V^{2}fF^2 (a figure of merit proposed by Jorel *et al.*[6]). Targeting film thicknesses to meet the ITRS 2023 capacitance density requirement resulted in leakage current density exceeding the 10 nA/cm^2 limit at 1V. Reduced leakage, which would possibly allow further scaling of this stack, could likely be achieved either by either the use of larger work function electrodes to increase the metal-insulator barrier heights or annealing to reduce defect density. The use of low oxygen affinity (-ΔH_{OX}) metals may also reduce α_{VCC}.

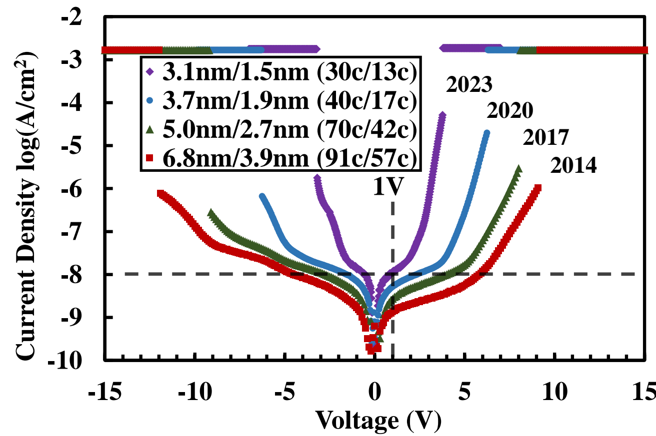

Figure 2.3: Current density vs. voltage sweeps for TaN/Al_2O_3/SiO_2/Al stacks targeting various ITRS nodes. The estimated thickness and number of PEALD cycles for each insulator pair are included in the legend.

Table 2.1: Comparison of Al_2O_3/SiO_2 Stacks Meeting Incremental ITRS Nodes

ITRS Node	Al_2O_3/SiO_2 (nm)	C/A (fF/µm^2)	αVCC (ppm/V^2)	J at 1V (A/cm^2)	J at -1V (|A|/cm^2)
2023	3.1 / 1.5	12.8	- - -	1.22×10^{-8}	1.43×10^{-8}
2020	3.7 / 1.9	10.1	-20	6.79×10^{-9}	8.65×10^{-9}
2017	5.0 / 2.7	7.9	20	2.75×10^{-9}	5.24×10^{-9}
2014	6.8 / 3.9	5.6	14	1.34×10^{-9}	2.83×10^{-9}

In Fig. 2.4 the 3.7 nm / 1.9 nm (40c/17c) Al_2O_3/SiO_2 device shows little variation with positive constant voltage stress time at fields below 9 MV/cm which, as seen in the inset with voltage ramped breakdown, is close to the breakdown strength of this stack. The difference in breakdown between positive and negative polarities is due to the built-in field of the electrodes. The negative polarity requires higher field to overcome the built-in field.

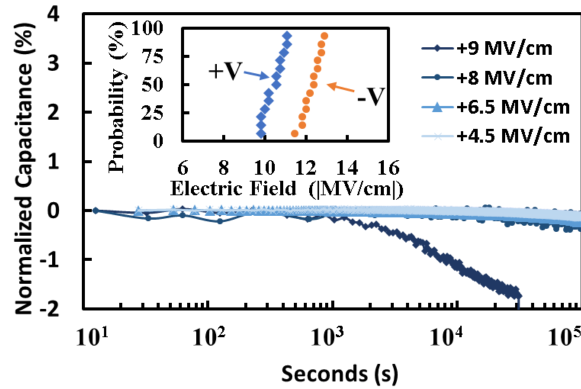

Figure 2.4: Capacitance variation vs. positive constant voltage stress time. Inset shows plot of voltage ramped breakdown for positive and negative polarity.

Table 2.2: Comparison of Low Voltage Nonlinearity MIIM Capacitors

Dielectric Stack	Film Thickness (nm)	C_{ox} (fF/μm^2)	αVCC (ppm/V^2)	J at 1V (A/cm^2)	Deposition Method	Dep/Anneal Temperature (℃)
HfO_2/SiO_2 [7]	12/4	6	14	$2.0\text{x}10^{-9}$	ALD/ PECVD	420
Sm_2O_3/SiO_2 [8]	7.5/4	7.3	-46	$1.8\text{x}10^{-8}$	Sputter/ PECVD	420
Er_2O_3/SiO_2 [9]	8.8/3.0	7	-73	$4.2\text{x}10^{-9}$	Sputter/ PEALD	400
STO/ZrO_2 [6]	20/20	11.5	-60	$3.5\text{x}10^{-8}$ (at 2V)	Sputter/ MOCVD	550
$STO/Al_2O_3/STO$ [10]	25.5/1.0/25.5	19.1	610	$1.0\text{x}10^{-9}$	ALD	600
ZTO/BZTO [11]	17/7	13.4	14	$7.5\text{x}10^{-9}$	E-Beam	400
$SiO_2/HfO_2/SiO_2$ [12]	3/4/3	12.4	32	$1.0\text{x}10^{-9}$	ALD	300
Al_2O_3/SiO_2 This Work	3.7/1.9	10.1	-20	$6.8\text{x}10^{-9}$	PEALD	200
ITRS 2020	- - -	10	< 100	$< 1.0\text{x}10^{-8}$	- - -	400 [2]

2.4 Conclusions

Al_2O_3/SiO_2 bilayers deposited via PEALD at 200℃ are investigated for applications in MIIM capacitors. An insulator stack consisting of 3.7 nm of Al_2O_3 and 1.9 nm of SiO_2 demonstrates a capacitance density of 10.1 fF/μm^2, a leakage current density

of 6.8 nA/cm^2 at 1V, and an α_{VCC} of -20 ppm/V^2. Benchmarking our results against the ITRS roadmap, it is seen that the Al_2O_3/SiO_2 stack simultaneously meets the 2020 node for capacitance density, leakage current density, and voltage nonlinearity projections with mainstream materials and low temperature processing.

2.5 Acknowledgments

Devices fabricated at the OSU Materials Synthesis and Characterization (MaSC) Facility.

2.6 References

[1] The International Technology Roadmap for Semiconductors (ITRS), On-Chip Passives Technology Requirements (Semiconductor Industry Association, 2013).

[2] A. Farcy, J.-F. Carpentier, M. Thomas, J. Torres, and P. Ancey, Microelectron. Eng. 85, 1940 (2008).

[3] M.D. Groner, J.W. Elam, F.H. Fabreguette, and S.M. George, Thin Solid Films 413, 186 (2002).

[4] C. Wenger, G. Lupina, M. Lukosius, O. Seifarth, H.-J. Müssig, S. Pasko, and C. Lohe, J. Appl. Phys. 103, 104103 (2008).

[5] N. Alimardani, S.W. King, B.L. French, C. Tan, B.P. Lampert, and J.F. Conley Jr., J. Appl. Phys. 116, 024508 (2014).

[6] C. Jorel, C. Vallée, P. Gonon, E. Gourvest, C. Dubarry, and E. Defay, Appl. Phys. Lett. 94, 253502 (2009).

[7] S.J. Kim, B.J. Cho, M.-F. Li, S.-J. Ding, C. Zhu, M.B. Yu, B. Narayanan, A. Chin, and D.-L. Kwong, IEEE Electron Device Lett. 25, 538 (2004).

[8] J.-J. Yang, J.-D. Chen, R. Wise, P. Steinmann, Y.-C. Yeo, and C. Zhu, IEEE Electron Device Lett. 30, 1033 (2009).

[9] T.H. Phung, D.K. Srinivasan, P. Steinmann, R. Wise, M.-B. Yu, Y.-C. Yeo, and C. Zhu, J. Electrochem. Soc. 158, H1289 (2011).

[10] J.H. Lee, Y.C. Lin, B.H. Chen, and C.Y. Tsai, in Solid-State Integr. Circuit Technol. ICSICT 2010 10th IEEE Int. Conf. On (IEEE, 2010), pp. 1024–1026.

[11] C.-C. Lin, Y.-H. Wu, R.-S. Jiang, and M.-T. Yu, IEEE Electron Device Lett. 34, 1418 (2013).

[12] S.-U. Park, C.-Y. Kang, H.-M. Kwon, B.-S. Park, W.-H. Choi, I.-S. Han, G. Bersuker, R. Jammy, and H.-D. Lee, Microelectron. Eng. 88, 3389 (2011).

[13] K.C. Chiang, C.H. Cheng, H.C. Pan, C.N. Hsiao, C.P. Chou, A. Chin, and H.L. Hwang, IEEE Electron Device Lett. 28, 235 (2007).

[14] C. Vallée, P. Gonon, C. Jorel, and F. El Kamel, Appl. Phys. Lett. 96, 233504 (2010).

3 ATOMIC LAYER DEPOSITION OF BISMUTH OXIDE USING $Bi(OCMe_2{}^iPr)_3$ AND H_2O

Dustin Z. Austin, Derryl Allman, David Price, Sallie Hose, Mark Saly, and John F. Conley, Jr.

Journal of Vacuum Science & Technology A 32, 01A113 (2014)

3.1 Introduction

Bismuth oxide (Bi_2O_3) has a number of useful material properties which include a high refractive index of n = 2.5 at 632 nm, optical nonlinearity, a bulk density of 8.9 g/cm^3, and a high dielectric constant of κ = 18-32.[1-5] As result, Bi_2O_3 has been utilized in many applications such as gas sensors, photovoltaic cells, solid oxide fuel cells, and optics.[6-12] In addition, Bi_2O_3 is known to readily form solid solutions with rare earth metals and has led to mixed metal films gaining interest for applications such as ferroelectrics, phase change memories, superconductors, and high-κ metal-insulator-metal (MIM) capacitors.[13-21] To date, most reports of thin film Bi_2O_3 have involved deposition using RF magnetron sputtering, pulsed laser deposition, or metal organic chemical vapor deposition (MOCVD). Atomic layer deposition (ALD) is a chemical vapor deposition (CVD) technique in which the precursor and oxidizing agent are introduced sequentially into the chamber with separation by inert gas purges. Deposition is based on self-limiting surface reactions, which allows for inherent atomic scale thickness control and excellent non-uniformity over large areas or high aspect ratio structures. A robust ALD process would enhance existing applications of thin film Bi_2O_3 and potentially enable new practical uses. However, ALD of Bi_2O_3 has typically only been incorporated into multicomponent oxide thin films because of the requirement for a catalyst to drive the ALD reaction or very low growth rates of approximately 0.01 nm/cycle.[22-28] Hatanpää et al. compared several Bi precursors and concluded that $Bi(OCMe_2{}^iPr)_3$ showed the highest potential for Bi_2O_3 growth due to its low melting point, high volatility, and high thermal stability.[29] Although Hatanpää et al. briefly discussed precursor stability and thick film growth, the Bi_2O_3 films were not fully

characterized. In this work, the growth per cycle, non-uniformity, crystal structure, density, interfacial roughness, composition, refractive index, and band gap of Bi_2O_3 deposited via ALD using $Bi(OCMe_2{}^iPr)_3$ and H2O are reported as a function of deposition temperature and post deposition annealing.

3.2 Experimental

Bi_2O_3 thin films were deposited on $Si/SiO_2/Si_3N_4$, $Si/SiO_2/TaN$, and $Si/SiO_2/TiN$ substrates. Prior to ALD, chemical mechanical polishing (CMP) was used on the insulating SiO_2 layer to form planar substrates. ALD of Bi_2O_3 was performed using alternating pulses of $Bi(OCMe_2{}^iPr)_3$ and H_2O in a Picosun SUNALE R-150B shower head reactor. The $Bi(OCMe_2{}^iPr)_3$ metal precursor was synthesized according to the literature procedure of Hatanpää et al.[29] $Bi(OCMe_2{}^iPr)_3$ was delivered to the reaction chamber using a Picosolid Booster delivery system. The N_2 flow rate was set to 150 sccm in all source lines and the pressure in the deposition chamber was approximately 1 Torr. Deposition temperatures between 90°C to 270°C, $Bi(OCMe_2{}^iPr)_3$ precursor temperatures between 85°C to 110°C, and $Bi(OCMe_2{}^iPr)_3$ pulse times between 0 s to 2 s were investigated. 120 s N_2 purges were used to produce low film non-uniformity. For most depositions, 500 ALD cycles were used to target a thickness of approximately 18 nm. Post deposition anneals, when performed, were conducted in a tube furnace using a nitrogen ambient of 5 Torr for 30 minutes.

Thermal gravimetric analysis (TGA) was performed on a TA Instruments Model Q50 system with a temperature ramp rate of 10°C/min under a nitrogen ambient at atmospheric pressure. Film morphology, density, thickness, and interfacial roughness were investigated via x-ray reflectivity (XRR) and grazing incidence x-ray diffraction

(GIXRD), using a Rigaku Ultima IV with Cu Kα radiation (λ = 1.5406 Ǻ) at a step size of 0.02° in the range of 10° to 90° and performed at room temperature. Microstructure was analyzed via high-resolution transmission electron microscopy (HRTEM) using a FEI Tecnai F20 with 200 KV accelerating voltage. Index of refraction, non-uniformity, and thickness measurements were conducted using a J.A. Woollam Co., Inc. M2000 spectroscopic ellipsometer in the range of 450-1000 nm and fit using a Cauchy model. Elemental oxygen, bismuth, hydrogen, carbon, nitrogen and silicon content of the Bi_2O_3 films were determined via Rutherford backscattering spectrometry (RBS) using a NEC Pelletron 3SDH. The band gap was measured by transmission and reflection measurements in the range of 200-1100 nm using an Ocean Optics HR4000 spectrometer.

3.3 Results and Discussion

3.3.1 Structural and Thermal Properties of $Bi(OCMe_2{}^iPr)_3$

$Bi(OCMe_2{}^iPr)_3$ is an alkoxide that contains three 2,3-dimethyl-2-butoxide ligands bonded to the bismuth metal center through a bridging oxygen atom, as shown in the inset of Fig. 3.1. The material is a white, low melting solid with sensitivity to air and moisture.[29] From the TGA weight loss curve also shown in Fig. 3.1, $Bi(OCMe_2{}^iPr)_3$ begins to evaporate near 90°C and is stable up to 236°C with less than 1% residue remaining. The TGA curve has a smooth decrease with no ledges or bumps, which is indicative of a good ALD precursor. A precursor temperature of 90°C was set as the operating point for this research.

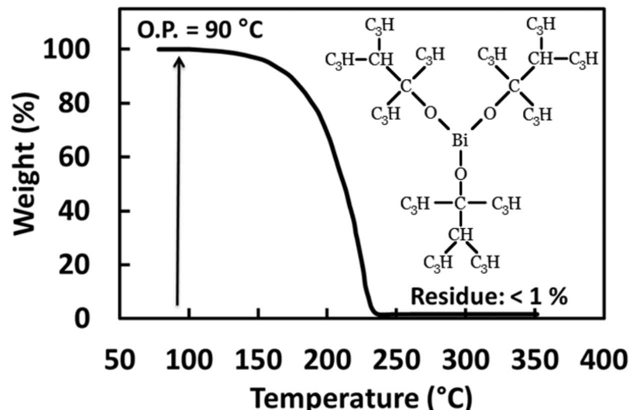

Figure 3.1: TGA and molecular structure of Bi(OCMe$_2$^{i}Pr)$_3$.

3.3.2 Bi(OCMe$_2$^{i}Pr)$_3$ Pulse Time and Growth per Cycle

Shown in Fig. 3.2 is a spectroscopic ellipsometry film thickness wafer map of a 2 s Bi(OCMe$_2$^{i}Pr)$_3$ pulse time performed at 150°C with 0.1 s H_2O pulses and 120 s N_2 purges repeated for 500 cycles. The deposition pattern in this figure is produced when Bi(OCMe$_2$^{i}Pr)$_3$ and H_2O are introduced from opposing ports in the reaction chamber. Unless otherwise noted, depositions in the rest of the paper will be performed using the above parameters.

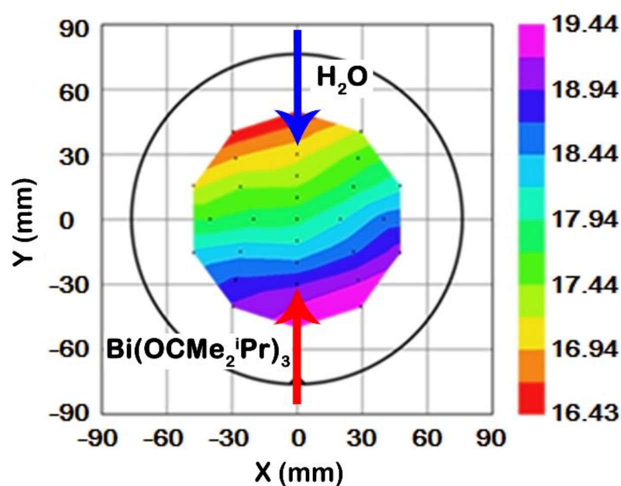

Figure 3.2: Film thickness wafer map for a 2 s pulse time of Bi(OCMe$_2$^{i}Pr)$_3$ (measured in units of nm).

Utilizing the film thickness wafer maps, non-uniformity has been calculated using the standard deviation divided by the average film thickness of all data points measured. In Fig. 3.3 is a plot of film thickness (blue diamonds) and non-uniformity (red squares) as a function of $Bi(OCMe_2{}^iPr)_3$ pulse time. The saturating ALD regime begins at approximately 0.5 s $Bi(OCMe_2{}^iPr)_3$ pulses, with longer pulse times up to 2 s leading to decreased non-uniformity. For a circular area with diameter of 100 mm, the non-uniformity is calculated to be less than 5%.

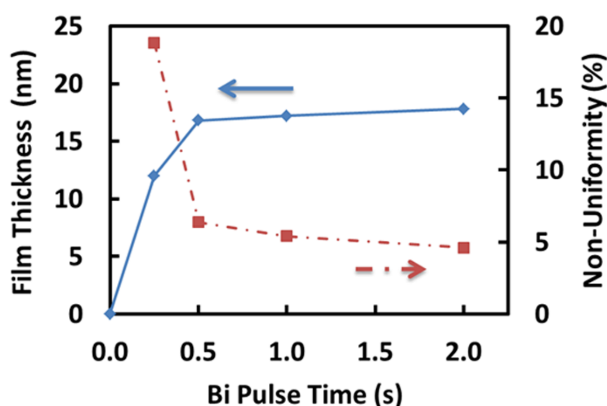

Figure 3.3: Bi_2O_3 film thickness (blue diamonds) and non-uniformity (red squares) as a function of $Bi(OCMe_2{}^iPr)_3$ pulse time.

Using a 2 s $Bi(OCMe_2{}^iPr)_3$ pulse time for best non-uniformity and a Si_3N_4 substrate, a plot of film thickness vs. number of cycles is shown in Fig. 3.4. From the x-axis intercept, there appears to be a nucleation delay of approximately 35 cycles. From the slope, the growth per cycle (GPC) was found to be 0.039 nm/cycle, when film thickness measurements are taken from the center of the wafer. This GPC is consistent with that reported by Hatanpää et al. and four times larger than other currently available bismuth precursors such as triphenylbismuth (TPB) and $Bi(thd)_3$, which may help with industrialization of ALD Bi_2O_3.

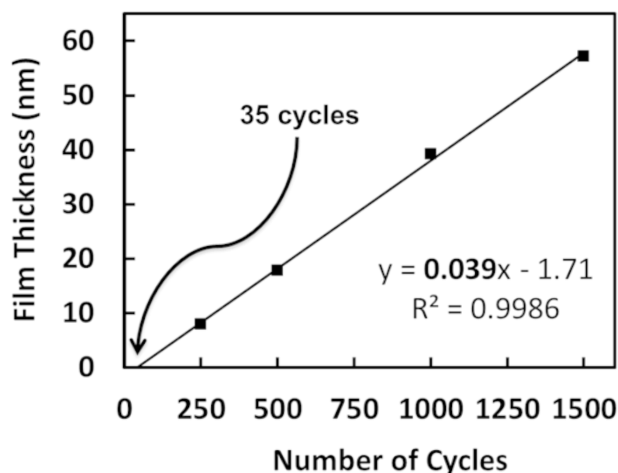

Figure 3.4: Bi_2O_3 film thickness vs. number of cycles for a 2 s $Bi(OCMe_2{}^iPr)_3$/120 s N_2/0.1 s H_2O/120 s N_2 sequence.

3.3.3 The Effect of Deposition Temperature on Bi_2O_3 Properties

The crystallographic structure of Bi_2O_3 is known to have a large influence over film properties. Bi_2O_3 forms four crystallographic phases, α, β, γ, and δ, which can be an oxide ionic, p-type, or n-type transparent semiconductor.[30-35] The deposition method as well as the deposition rate can influence whether Bi_2O_3 films are deposited in the monoclinic α phase (fast deposition rate) or the tetragonal β phase (slow deposition rate). Shown in Fig. 3.5 are GIXRD spectra of Bi_2O_3 films deposited between 90°C to 270°C. Amorphous Si_3N_4 substrates were used to obtain a featureless reference scan. ALD is known for slow deposition rates and it is observed that films deposited at 90°C through 150°C all show the β phase with a (201) preferred crystal orientation. At a deposition temperature of 210°C, the film still shows the β phase, but the grains no longer have a single preferred crystal orientation. At 270°C, the (201) peak has almost completely faded into the background.

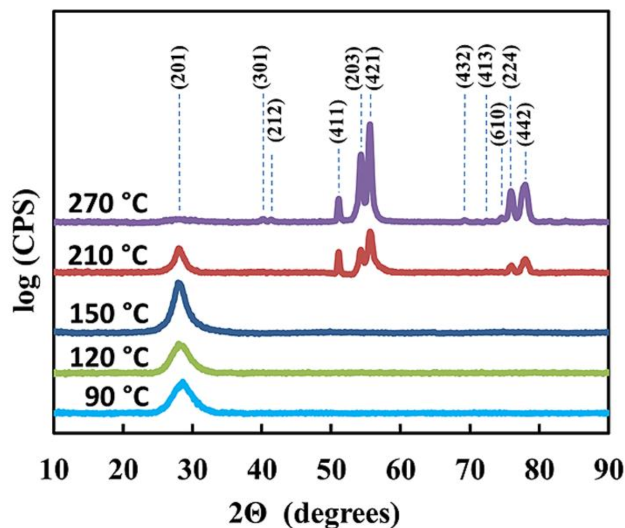

Figure 3.5: GIXRD spectra of Bi_2O_3 films with deposition temperatures between 90 and 270°C. Dashed vertical lines indicate various peaks of Bi_2O_3 β phase (PDF: 00-027-0050).

Further examining the deposition temperature dependence, shown in Fig. 3.6(a) is a plot of film thickness (blue diamonds), density (red squares), and interfacial roughness (green triangles) obtained from modeling the XRR data in Fig. 3.6(b). For deposition temperatures up to 210°C, as deposited films have an interfacial roughness of less than 5 Å, a density of 8.3 g/cm^3 (which is slightly lower than the bulk density of 8.9 g/cm^3), and have an average film thickness ranging between 16.7 and 17.8 nm. Films deposited at 270°C show a dramatic increase in both interfacial roughness and average film thickness, which may be explained by the film having enough energy to coalesce into islands as it grows.[36] In addition, density appears to decrease at 270°C, although it should be noted that due to the accompanying increased roughness in these films, the measurement model accuracy is reduced.

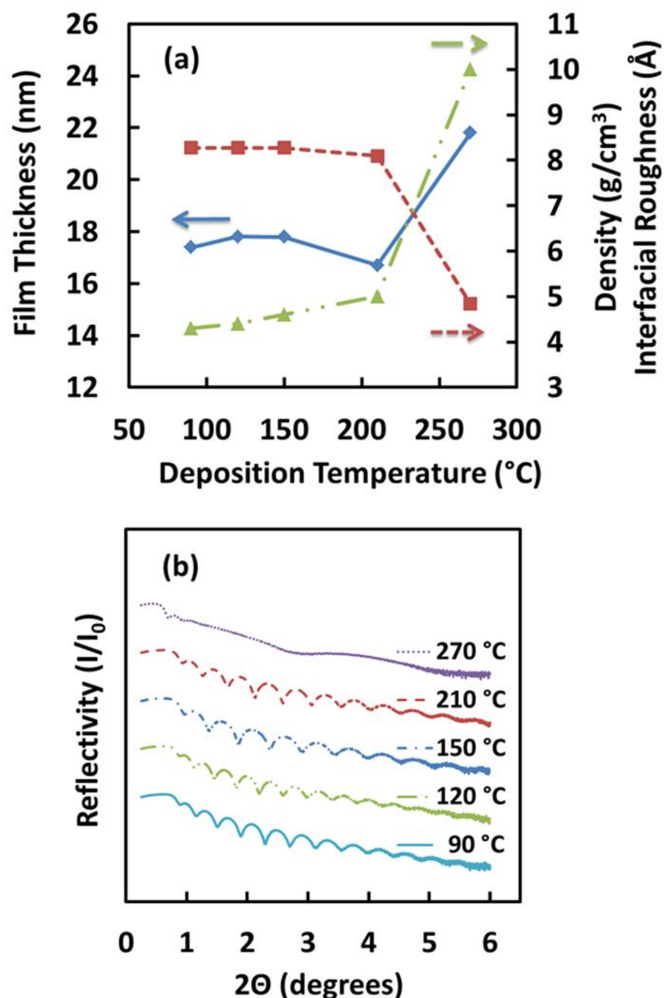

Figure 3.6: (a) Extracted film thickness (blue diamonds, left axis), density (red squares, right axis), and interfacial roughness (green triangles, right axis) plotted as a function of deposition temperature. (b) XRR spectrum of Bi_2O_3 films with deposition temperatures between 90 and 270°C.

Due to high thermal expansion coefficients, Bi_2O_3 films are known to show increased volume with increased deposition temperature.[30-31] Shown in Fig. 3.7 are TEM images of a Bi_2O_3 film deposited at (a) 150°C and (b) 270°C. In agreement with the XRR data from Fig. 3.6, the 150°C film has low interfacial roughness, while the film deposited at 270°C has a dramatic increase in both interfacial roughness and average film thickness, consistent with increased volume.

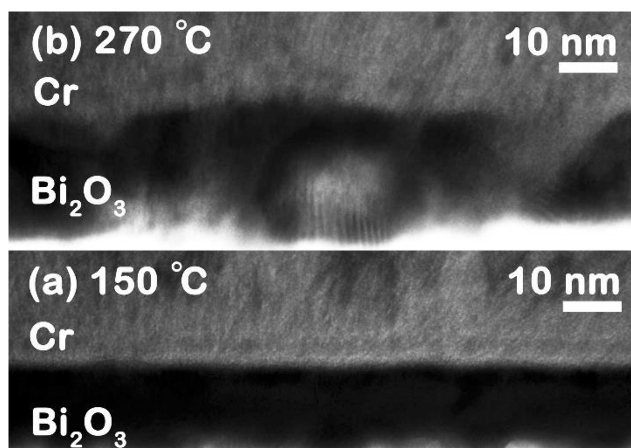

Figure 3.7: HRTEM of Bi_2O_3 films deposited at (a) 150°C and (b) 270°C.

A similar comparison is made characterizing the optical properties for deposition temperatures between 90°C to 270°C. Shown in Fig. 3.8 are spectra of the index of refraction, *n,* vs. wavelength for the various deposition temperatures. The index of refraction was measured via spectroscopic ellipsometry and is taken as n^2. Shown in Fig. 3.9(a) is a semi-log plot of absorption coefficient (α) vs. energy. The band gap is taken as the energy at which the absorption coefficient abruptly increases.[37] Next in Fig 3.9(b) is a plot of $(\alpha h\upsilon)^{1/2}$ vs. energy from which the optical band gap may also be estimated by extrapolating the linear portion of each curve to the x-axis. Similar values for the band gap are obtained from both plots, suggesting that the electronic structure has indirect-allowed transitions.[38] The same general trend is observed in which the largest measured band gap is 2.9 eV for a deposition temperature of 150°C. As deposition temperature increased to 270°C, the band gap became indeterminable.

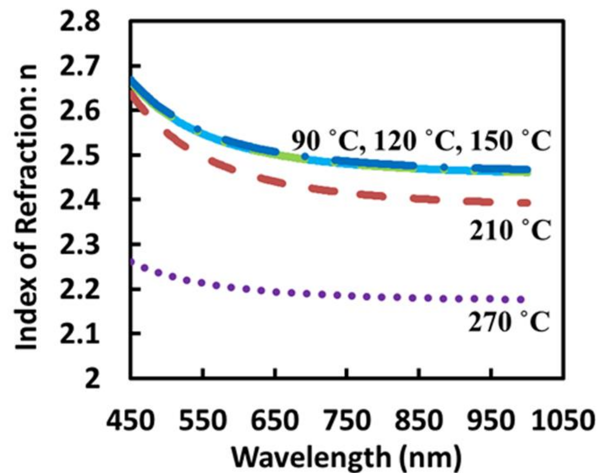

Figure 3.8: Index of refraction vs. wavelength for Bi2O3 films with deposition temperatures between 90 and 270°C.

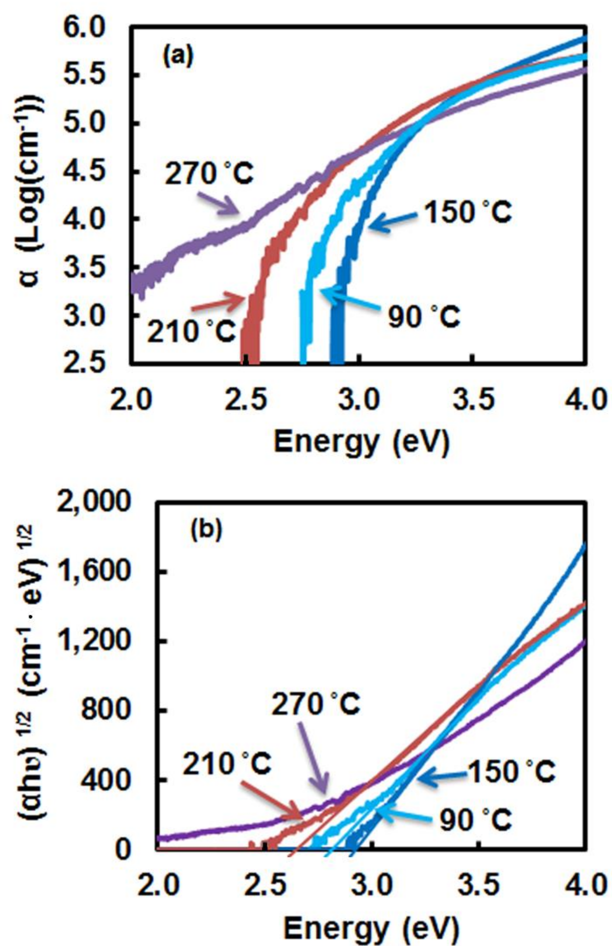

Figure 3.9: (a) Absorption coefficient (a) vs. energy and (b) band gap estimation, $(\alpha h\nu)^{1/2}$ vs. energy, of Bi_2O_3 films deposited between 90 and 270°C.

The band gap, index of refraction, derived optical dielectric constant, and density for a range of deposition temperatures are compiled in Table 3.1. Each parameter indicates the same general dependence on temperature with a maximum at 150°C. The decrease in these parameters may be explained by the introduction of defect bands as the films become less ordered. As seen previously via GIXRD spectra, there is peak narrowing as the deposition temperature increases to 150°C but a shift away from a single preferred crystal orientation above 150°C.

Table 3.1: Tabulated Values for Optical and Physical Properties of Bi_2O_3 films.

T_{Dep} (˚C)	E_g (eV)	n (632 nm)	ε_r (632 nm)	ρ (g/cm^3)
90	2.8	2.50	6.29	8.3
150	2.9	2.51	6.32	8.3
210	2.5	2.45	5.99	8.1
270	-	2.20	4.83	4.8

Shown in Fig. 3.10 is the RBS atomic concentration vs. depth profiles for elemental oxygen, bismuth, hydrogen, carbon, nitrogen, and silicon content in a Bi_2O_3 film deposited at 150°C on a silicon nitride substrate. The elemental bismuth content is deficient at 31 at% and appears to be replaced by hydrogen, which suggests there could be unreacted sites left on surface after each $Bi(OCMe_2{}^iPr)_3$ pulse. The carbon content is not shown in Fig. 3.10 as it was below the detectable limit in all films. The RBS data showed roughly consistent composition for deposition temperatures of 90°C to 270°C.

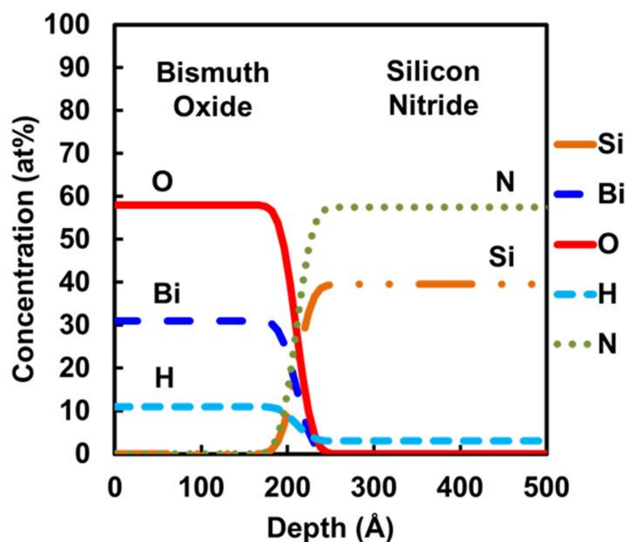

Figure 3.10: Elemental content obtained from RBS of Bi_2O_3 films deposited at 150°C.

3.3.4 Substrate Impact on Film Morphology

The crystallographic orientation of the substrate is known as a potential source of influence on the morphology of overlying films. In addition to amorphous Si_3N_4, conductive polycrystalline substrates of TaN and TiN are investigated for their influence on the growth of Bi_2O_3 films. TiN and TaN substrates were chosen for their prominent role in back end of line (BEOL) applications in microelectronics. Displayed in Fig. 3.11 is GIXRD intensity vs. 2θ spectra for various substrates with and without overlying ALD Bi_2O_3 films. Bare TaN and TaN / Bi_2O_3 are grouped together at the top, bare TiN and TiN / Bi_2O_3 are grouped in the middle, and the reference silicon nitride / Bi_2O_3 is at the bottom. First focusing on the TaN group at the top, the only difference between the two spectra is the appearance of the β-phase related (201) peak at 2θ = 28.6° in the Bi_2O_3 coated sample. Next, considering the TiN group in the middle, the results are very similar with the additional (201) peak in the Bi_2O_3 coated sample being the only difference. For all three substrates, only the same (201) peak of the Bi_2O_3 β-phase is

observed, indicating that these substrates produce little influence on the overlying Bi_2O_3 film morphology.

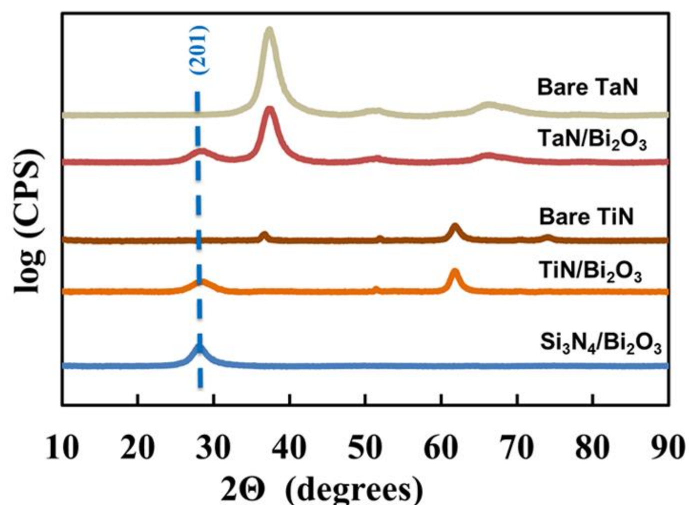

Figure 3.11: GIXRD spectra of Bi_2O_3 films deposited on Si_3N_4, TaN, and TiN substrates. The dashed vertical line indicates (201) peak of Bi_2O_3 β phase (PDF: 00-027-0050).

3.3.5 Impact of Annealing

Shown in Fig. 3.12 are GIXRD spectra of Bi_2O_3 thin films annealed for 30 minutes at 5 Torr in N_2 at 450°C and 800°C, with measurements made post cooling at 30°C. The 450°C spectrum has a strong peak at 28.6° corresponding to the (201) peak of the β phase with weaker peaks from the α phase. The 800°C spectrum appears to fully transition into the α phase upon cooling. In Fig. 3.13, a post 450°C anneal HRTEM image reveals that the Bi_2O_3 film exhibits large uneven volumetric expansion, which is in agreement with literature reports for Bi_2O_3.[30-31] Finally, the 800°C annealed films were observed to delaminate from the substrate.

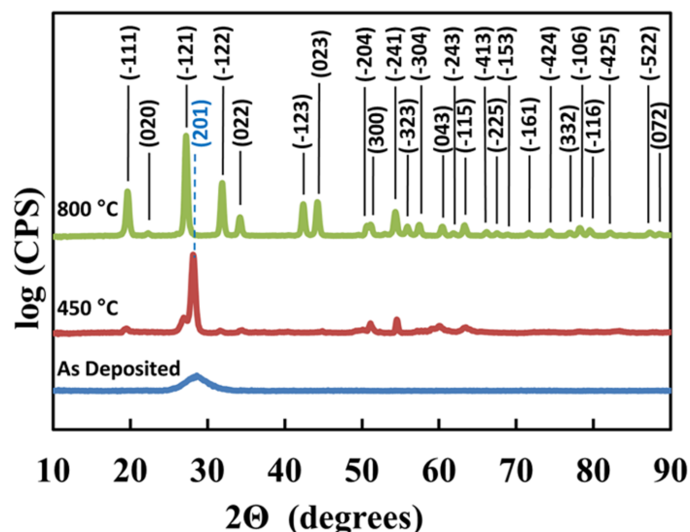

Figure 3.12: GIXRD spectra of as-deposited and annealed Bi_2O_3 films. Dashed vertical blue line indicates Bi_2O_3 β phase (PDF: 00-027-0050); solid vertical black lines indicate Bi_2O_3 α phase (PDF: 01-071-0465).

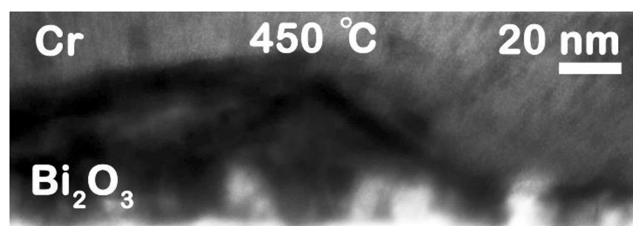

Figure 3.13: HRTEM of 450°C annealed Bi_2O_3.

3.4 Conclusions

In conclusion, Bi_2O_3 thin films were deposited by ALD using $Bi(OCMe_2{}^iPr)_3$ and H_2O at deposition temperatures between 90°C to 270°C on Si_3N_4, TaN, and TiN substrates. For films deposited at 90°C to 150°C, the Bi_2O_3 β phase with single preferred crystal orientation of (201) was observed and found to be independent of the underlying substrates. RBS indicates films are carbon free but contain excess hydrogen. Films with deposition temperatures greater than 150°C and post deposition annealed resulted in increased interfacial roughness with reduced band gap, density, and refractive index. Bi_2O_3 films deposited at 150°C showed the best film properties with a density of 8.3

g/cm^3, a band gap of 2.9 eV, a refractive index of 2.51 at 632 nm, an optical dielectric constant of 6.32, the lowest interfacial roughness, and a GPC of 0.039 nm/cycle. Due to these film properties combined with high GPC and low C content, $Bi(OCMe_2{}^iPr)_3$ appears to be a candidate for ALD of Bi_2O_3 and multi-component Bi based oxide thin films.

3.5 Acknowledgments

The authors would like to thank graduate students R. Ravichandran (OSU) and S. Smith (OSU) for assistance with optical and XRR measurements, respectively, C. Tasker (Manager OSU cleanroom) for equipment support, T. Mueller (ON Semiconductor) for assistance with TEM imaging, Dr. C. Dezelah (Picosun) for technical discussions, ON Semiconductor for financial support, and SAFC Hitech for providing $Bi(OCMe_2{}^iPr)_3$.

3.6 References

[1] V. Dolocan and F. Iova, Phys. Status Solidi A 64, 755 (1981).

[2] L. Leontie, M. Caraman, A. Visinoiu, and G. I. Rusu, Thin Solid Films 473, 230 (2005).

[3] V. Dimitrov and S. Sakka, J. Appl. Phys. 79, 1736 (1996).

[4] H. Frederikse, CRC Handbook of Chemistry and Physics (CRC, Boca Raton, 2003).

[5] S. Condurache-Bota, N. Tigau, A. P. Rambu, G. G. Rusu, and G. I. Rusu, Appl. Surf. Sci. 257, 10545 (2011).

[6] D. Shan, J. Zhang, H.-G. Xue, Y.-C. Zhang, S. Cosnier, and S.-N. Ding, Biosens. Bioelectron. 24, 3671 (2009).

[7] B. Sirota, J. Reyes-Cuellar, P. Kohli, L. Wang, M. E. McCarroll, and S. M. Aouadi, Thin Solid Films 520, 6118 (2012).

[8] K. Kobayashi, J. Non-Cryst. Solids 316, 403 (2003).

[9] H. Weidong, Q. Wei, W. Xiaohong, D. Xianbo, C. Long, and J. Zhaohua, Thin Solid Films 515, 5362 (2007).

[10] K. L. Chopra and S. R. Das, Thin Film Solar Cells (Plenum, New York, 1983).

[11] T. P. Gujar, V. R. Shinde, C. D. Lokhande, and S.-H. Han, Mater. Sci. Eng. B 133, 177 (2006).

[12] X. Gou, R. Li, G. Wang, Z. Chen, and D. Wexler, Nanotechnology 20, 495501 (2009).

[13] W. H. Dumbaugh and J. C. Lapp, J. Am. Ceram. Soc. 75, 2315 (1992).

[14] Y. Zeng and Y. S. Lin, J. Catal. 182, 30 (1999).

[15] D. Barreca, G. A. Rizzi, and E. Tondello, Thin Solid Films 333, 35 (1998).

[16] E. M. Dianov, J. Lightware Technol. 31, 681 (2013).

[17] C. D. Ling, R. L. Withers, S. Schmid, and J. G. Thompson, J. Solid State Chem. 137, 42 (1998).

[18] K.-H. Cho, C.-H. Choi, Y. H. Jeong, S. Nahm, C.-Y. Kang, S.-J. Yoon, and H.-J. Lee, J. Electrochem. Soc. 155, G148 (2008).

[19] B. H. Park, B. S. Kang, S. D. Bu, T. W. Noh, J. Lee, and W. Jo, Nature 401, 682 (1999).

[20] M. Vehkamaki, T. Hatanpaa, M. Kemell, M. Ritala, and M. Leskela, Chem. Mater. 18, 3883 (2006).

[21] M. Karimi, R. Tu, J. Peng, W. Lennard, G. H. Chapman, and K. L. Kavanagh, Thin Solid Films 515, 3760 (2007).

[22] Y. D. Shen, Y. W. Li, W. M. Li, J. Z. Zhang, Z. G. Hu, and J. H. Chu, J. Phys. Chem. C 116, 3449 (2012).

[23] M. Vehkamaki, T. Hatanpaa, M. Ritala, and M. Leskela, J. Mater. Chem. 14, 3191 (2004).

[24] S. J. A. Moniz, C. S. Blackman, C. J. Carmalt, and G. Hyett, J. Mater. Chem. 20, 7881 (2010).

[25] M. Mehring, Coord. Chem. Rev. 251, 974 (2007).

[26] S. W. Kang and S. W. Rhee, Thin Solid Films 468, 79 (2004).

[27] G. Bandoli, D. Barreca, E. Brescacin, G. A. Rizzi, and E. Tondello, Chem. Vap. Deposition 2, 238 (1996).

[28] M. Putkonen and L. Niinisto, Precursor Chemistry of Advanced Materials (Springer-Verlag, Berlin, 2005), Vol. 9, pp. 125–145.

[29] T. Hatanpaa, M. Vehkamaki, M. Ritala, and M. Leskela, Dalton Trans. 39, 3219 (2010).

[30] P. Shuk, H.-D. Wiemhofer, U. Guth, W. Gopel, and M. Greenblatt, Solid State Ionics 89, 179 (1996).

[31] M. Yashima, D. Ishimura, and K. Ohoyama, J. Am. Ceram. Soc. 88, 2332 (2005).

[32] H. A. Harwig and A. G. Gerards, J. Solid State Chem. 26, 265 (1978).

[33] E. Oniyama and P. G. Wahlbeck, J. Phys. Chem. B 102, 4418 (1998).

[34] D. Risold, B. Hallstedt, L. J. Gauckler, H. L. Lukas, and S. G. Fries, J. Phase Equilib. 16, 223 (1995).

[35] R. B. Patil, R. K. Puri, and V. Puri, Arch. Phys. Res. 2, 31 (2011).

[36] R. L. Puurunen and W. Vandervorst, J. Appl. Phys. 96, 7686 (2004).

[37] Y. Hishikawa, N. Nakamura, S. Tsuda, S. Nakano, Y. Kishi, and Y. Kuwano, Jpn. J. Appl. Phys., Part 1 30, 1008 (1991).

[38] S. Adachi, Optical Properties of Crystalline and Amorphous Semiconductors: Materials and Fundamental Principles, 1st ed. (Kluwer Academic, Boston, 1999).

4 ATOMIC LAYER DEPOSITION OF RUTHENIUM AND RUTHENIUM OXIDE USING A ZERO OXIDATION STATE PRECURSOR

Dustin Z. Austin, Melanie A. Jenkins, Derryl Allman, Sallie Hose, David Price,

Charles L. Dezelah, and John F. Conley, Jr.

Chemistry of Materials 29, 1107-1115 (2017)

4.1 Introduction

Atomic layer deposition (ALD) is a technique that has received a considerable and growing amount of attention because of its ability to provide uniform and conformal layers of solid materials, often with subnanometer control over thickness. In particular, ALD has found important applications in the microelectronics industry, where dielectrics are now well established and conductive films, including ruthenium-containing layers, have become the focal point of much research. Ruthenium metal has a low bulk resistivity (7.1 μΩ cm), a high work function (4.7 eV), and a low solid solubility with strong adhesion to Cu, making Ru an attractive barrier metal or seed layer for Cu electroplating.[1] Ruthenium oxide (RuO_2) also has a low resistivity (46 μΩ cm), an even higher work function (5.1eV), and a good chemical stability, making RuO_2 of interest as an electrode for CMOS transistors and high-κ metal−insulator−metal capacitors.[2-4] Its relatively high chemical stability makes RuO_2 less likely to form an interfacial layer during dielectric deposition than commonly used bottom electrodes such as TaN and TiN. Unwanted interfacial layers can comprise a substantial percentage of the dielectric thickness and reduce the maximal achievable capacitance.[5] In addition, prior work with RuO_2 has demonstrated that it may be used to template the high-κ rutile phase of TiO_2 at reduced deposition temperatures.[2-4] Because of its inherent advantages relative to traditional film growth methods, ALD processes for Ru and RuO_2 are strongly desired for coating the high-aspect ratio structures encountered in the back end of line of ultra largescale integration (ULSI) process flows.

A key limiting factor in the implementation of ALD for emerging applications is the development of new process chemistry that affords optimal film growth

characteristics. For example, $Ru(EtCp)_2$, currently the most widely reported Ru ALD precursor and commonly used in CVD processes, lacks a clear thermal ALD deposition window and shows very long nucleation delays on SiO_2 and TaN surfaces for both Ru and RuO_2 deposition.[6-15] Although the incorporation of NH_3 plasma has been shown to improve the nucleation and growth problems, the process is not ideal because of the toxicity, added expense, and intrinsic aspect ratio limitations of plasma-based processes.[12,13] As Ru and RuO_2 films in ULSI applications are generally only a few to tens of nanometers thick, nucleation delay is a critical growth parameter. When a large number of cycles is required to obtain a continuous film, it not only can dramatically increase the deposition time, decreasing throughput and increasing cost considerably in manufacturing, but also can result in rougher interfaces because of island-like nucleation. Other Ru precursors with non-zero oxidation states also typically exhibit long nucleation delays for Ru and RuO_2 when grown by thermal ALD.[6,9,16-27] More recent work has shown Ru(0) complexes can significantly reduce nucleation delays for O_2-based thermal ALD processes.[28-34] Most Ru(0) ALD precursors contain an η^6-arene ligand, while most higher-oxidation state precursors contain one or more cyclopentadienyl ligands, or a substituted variant thereof.[35] Herein, we report a previously unexplored Ru(0) precursor, η^4-2,3-dimethylbutadiene ruthenium tricarbonyl [$Ru(DMBD)(CO)_3$], which is unusual in that it contains neither arene nor cyclopentadienyl ligands. Only a small number of ALD studies have used zero-oxidation state Ru precursors containing a butadiene type ligand.[28-34,36,37] Alkene ligands, including butadiene derivatives, may help stabilize low-oxidation state metal complexes because of their ability to engage in π backbonding. However, in all but two cases, the previously reported butadiene-bearing Ru(0)

precursors also contain an η^6-arene ligand.[36,37] $Ru(DMBD)(CO)_3$ also possesses carbonyl ligands, which are known to readily undergo dissociation from metal centers.[38] We propose that the lability of carbonyl together with the stabilizing influence of DMBD allows the precursor to facilitate rapid nucleation on a surface, while also delivering a robust process capable of performing ALD at temperatures in excess of 300°C.

In this work, we develop and characterize a thermal ALD process for Ru metal as well as both thermal ALD and PEALD processes for RuO_2 using $Ru(DMBD)(CO)_3$ and oxygen.

4.2 Experimental Procedure

$Ru(DMBD)(CO)_3$ was obtained from EMD Performance Materials and was used for deposition experiments as received without further purification. $Ru(DMBD)(CO)_3$ can be synthesized on laboratory scale from $Ru_3(CO)_8$ and DMBD using a method reported previously for Ru diene complexes.[39] Thermal gravimetric analysis (TGA) of $Ru(DMBD)(CO)_3$ was performed in a TA Instruments Model Q50 system with a temperature ramp rate of 10°C/min under a nitrogen ambient at atmospheric pressure. Vapor pressure was determined from isothermal TGA measurements using a method described previously.[40]

ALD of Ru and RuO_2 was performed in a Picosun SUNALE R-200 reactor at 6 Torr using alternating N_2-purge-separated pulses of $Ru(DMBD)(CO)_3$ and either molecular O_2 or oxygen plasma on Si substrates with 100 nm of thermally grown SiO_2. All depositions followed a reactor conditioning process that coated the chamber with ~50 nm of either Ru or RuO_2, depending on the intended film. Flow rates in all source lines

were held at 150 sccm, except for the O_2 line, which used 180 sccm of O_2 with either 150 or 50 sccm N_2 carrier gas for ruthenium metal or ruthenium oxide, respectively. As reported previously for Ru processes, the O_2 partial pressure is important for determining the composition of the deposited film.[7,8]

Ru(DMBD)$(CO)_3$, shown in the inset of Figure 4.1a, is a zero-oxidation state precursor that is liquid at room temperature. A vapor pressure between 1 and 2 Torr is achieved over a wide temperature range of 35−60°C, shown in Figure 4.1a. In Figure 4.1b, the TGA curve and the associated derivative reveal a single weight loss event from ~80 to 130°C, after which <1% of the original precursor mass remains. This observation is consistent with complete clean volatilization without nonvolatile residues remaining. TGA alone, however, cannot rule out decomposition products that may evaporate concurrently with the precursor. Although a decomposition event concurrent with volatilization could result in a derivative curve with multiple peaks, this was not observed for this compound. On the basis of the vapor pressure and TGA, a precursor temperature of 45°C was chosen to give a sufficient dose while limiting aging of the Ru(DMBD)$(CO)_3$ due to temperature stressing.

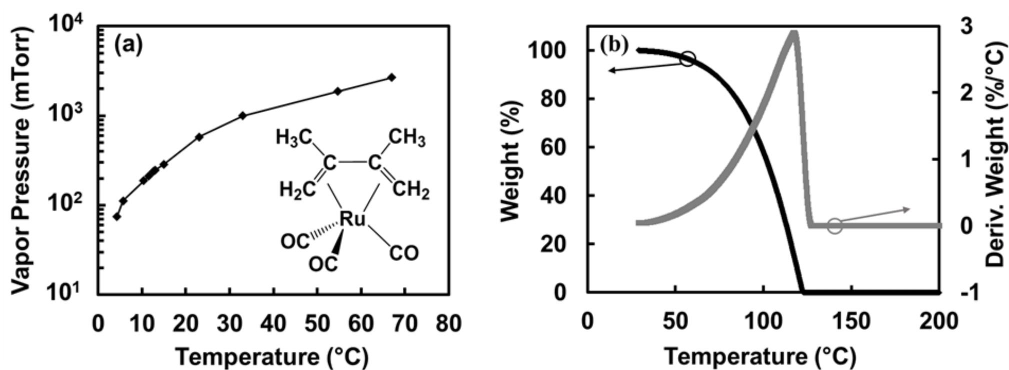

Figure 4.1: (a) Vapor pressure vs. temperature for Ru(DMBD)$(CO)_3$ with the inset showing molecular structure. (b) TGA % weight remaining vs. temperature and derivative for Ru(DMBD)$(CO)_3$.

Film morphology, density, thickness, and interfacial roughness were investigated via X-ray reflectivity (XRR) and grazing incidence X-ray diffraction (GIXRD) using a Rigaku Ultima IV instrument with Cu Kα radiation (λ = 1.5406 Å). RuO_2 film thickness was measured using a J. A. Woollam M2000 spectroscopic ellipsometer (SE) in the range of 400−1000 nm. Surface roughness was measured via atomic force microscopy (AFM) using an Asylum Research MFP-3D instrument in tapping mode with a 1 Hz scan rate. Resistivity was measured via a four-point probe. Compositional analysis was performed using a combination of X-ray photoelectron spectroscopy (XPS) and Auger electron spectroscopy (AES) via a PHI VersaProbe II with excitation from monochromatic Al Kα X-ray radiation (hν = 1486.6 eV), with a 15 keV X-ray beam voltage, and sputtered with 2 keV argon ions.

4.3 Results

4.3.1 ALD Ru

The growth of Ru films was studied using a thermal ALD process in which $Ru(DMBD)(CO)_3$ and O_2 were alternately pulsed into the deposition chamber. Shown in Figure 4.2 is a plot of Ru film thickness, measured via XRR, versus deposition temperature. Using 2.0 s O_2 pulses and 1.5 s $Ru(DMBD)(CO)_3$ pulses separated by 30 s N_2 purges, an ALD window (defined here as a relatively constant film thickness) was found between 290 and 320°C. The film deposited at 320°C has a density of 12.2 g/cm^3, which is just below the bulk value of Ru (12.37 g/cm^3).[41] Also shown in Figure 4.2, the resistivity slightly decreased with an increase in deposition temperature, ranging from ~18 μΩ cm at 290°C to ~14 μΩ cm at 320°C.

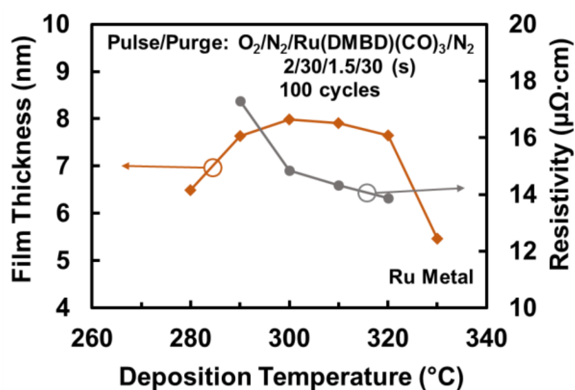

Figure 4.2: Film thickness and resistivity vs. deposition temperature for ALD Ru metal.

The effect of Ru(DMBD)$(CO)_3$ pulse time on film thickness, while all other variables are held constant, is shown in Figure 4.3a. Self-limited saturating growth was observed with Ru pulse times of >1.5 s. Shorter pulse times resulted in either less growth (0.6 and 0.9 s) or more growth (1.2 s). With respect to O_2 pulse time, shown in Figure 4.3b, the deposition rate showed a soft saturation between 2 and 3 s with a large increase observed when longer O_2 exposures were used. As discussed below, this is suggestive of an increase in the rate of uptake of oxygen into films when using O_2 doses beyond the amount needed for the reaction to form metallic Ru. To rule out growth due to possible precursor decomposition, a control run with 200 ALD cycles of Ru(DMBD)$(CO)_3$ without the oxygen co-reactant (1.2, 30, 0, and 30 s for Ru, N_2, O_2, and N_2, respectively) at 300°C resulted in no measurable deposition on the SiO_2/Si substrate.

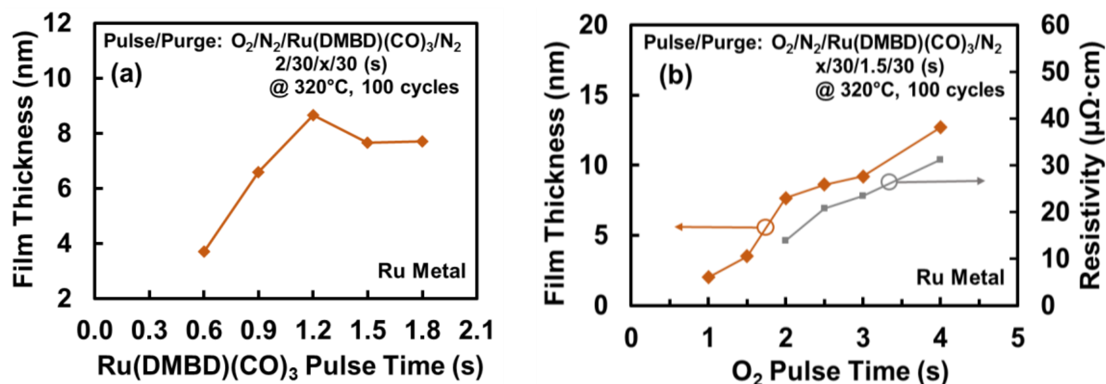

Figure 4.3: Film thickness vs. (a) $Ru(DMBD)(CO)_3$ pulse time and (b) O_2 pulse time for ALD Ru metal.

Shown in Figure 4.4 is a plot of Ru film thickness as a function of the number of deposition cycles. ALD Ru metal was found to have a linear growth per cycle (GPC) of 0.067 nm/cycle at 320°C with a negligible nucleation delay. Nucleation delay was estimated by extrapolating the linear fit to the x-axis. Because the x-intercept of the best-fit line crossed very near the origin, it can be surmised that the initial stages of growth proceeded at a rate having very little deviation from that observed with a larger number of deposition cycles, a good indication that a significant nucleation delay did not occur.

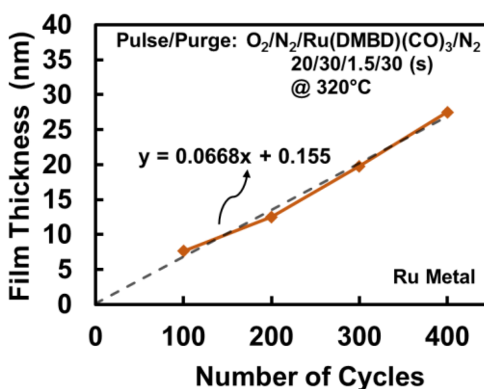

Figure 4.4: Film thickness vs. the number of ALD cycles for ALD Ru metal.

Compositional analysis of a 20 nm thick Ru film deposited at 320°C was performed using a combination of XPS and AES and is shown in Figure 4.5. The film was sputtered using 2 keV argon ions for 30 s to the approximate midpoint depth of the

film. Peaks for the Ru $3d_{5/2}$ and Ru $3d_{3/2}$ ionizations were observed at 280.1 and 284.3 eV, respectively, and are consistent with metallic Ru but are also similar to the reported values for RuO_2.[42] The oxygen content was below the detection limits of the instrument (<0.1%). Because of the overlap of the C 1s region with the Ru $3d_{3/2}$ region, carbon could not be easily quantified by XPS. Inspection of the AES spectrum in the region of the C KLL transition revealed that carbon was below the detection limit.

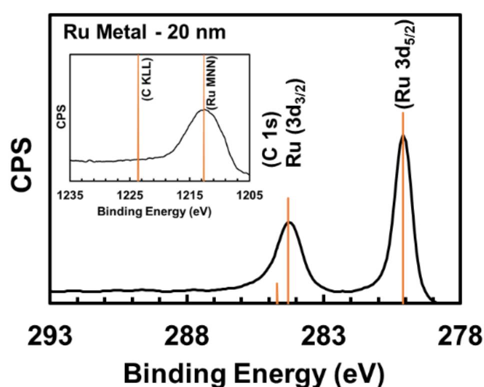

Figure 4.5: High-resolution XPS spectrum of Ru $3d_{5/2}$ and Ru $3d_{3/2}$ ionizations for ALD Ru metal film with an inset of high-resolution AES regions for C KLL and Ru MNN.

GIXRD confirmed a polycrystalline hexagonal microstructure with no preferred orientation for an 8 nm thick Ru film deposited at 320°C (Figure 4.6). An average crystal size of ~7.6 nm was estimated using the Scherrer formula. In Figure 4.7, AFM measurement of the same film showed 0.6 nm RMS surface roughness.

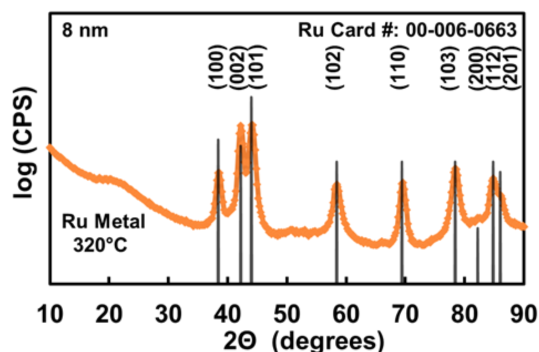

Figure 4.6: GIXRD plot of log intensity vs. 2θ for an 8 nm thick ALD Ru metal film deposited at 320°C with a reference card pattern overlay.

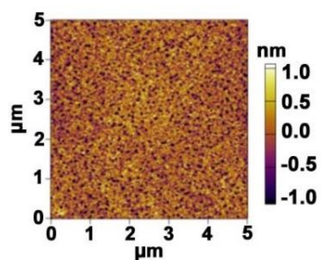

Figure 4.7: AFM surface roughness measurements of an 8 nm thick ALD Ru metal film deposited at 320°C.

4.3.2 ALD RuO_2

Using the same $Ru(DMBD)(CO)_3$ precursor, RuO_2 was investigated via (a) thermal ALD with molecular O_2 and (b) PEALD using plasma-generated oxygen radicals as the co-reactant. Plots of film thickness versus deposition temperature are shown in Figure 4.8 for both ALD processes. Clear ALD temperature windows were evident for both thermal and plasma processes. Both RuO_2 process windows required lower temperatures and much longer (20 s) oxidant exposures, as compared to the Ru process (2 s O_2 exposures) discussed previously. For thermal ALD, a 20°C wide RuO_2 window with a nearly constant film thickness was observed between 220 and 240°C, with the best nonuniformity (~2.8% across a 6 in. wafer) observed at a deposition temperature of 240°C. In comparison, the PEALD RuO_2 process exhibited an ALD window with a range

of 30°C, shifted to slightly lower temperatures (200−230°C). PEALD films showed a degraded nonuniformity of 4.5% at 230°C. For both processes, the deposition rate dropped off at temperatures below the ALD window and increased at temperatures above the ALD window.

Also included in Figure 4.8 are plots of resistivity versus deposition temperature for both the (a) ALD and (b) PEALD processes. Within the respective ALD windows, resistivity for both processes decreased slightly with increasing temperature. The thermal ALD RuO_2 films had a resistivity as low as ~62 μΩ cm, while that of the PEALD films was much higher (~377 μΩ cm).

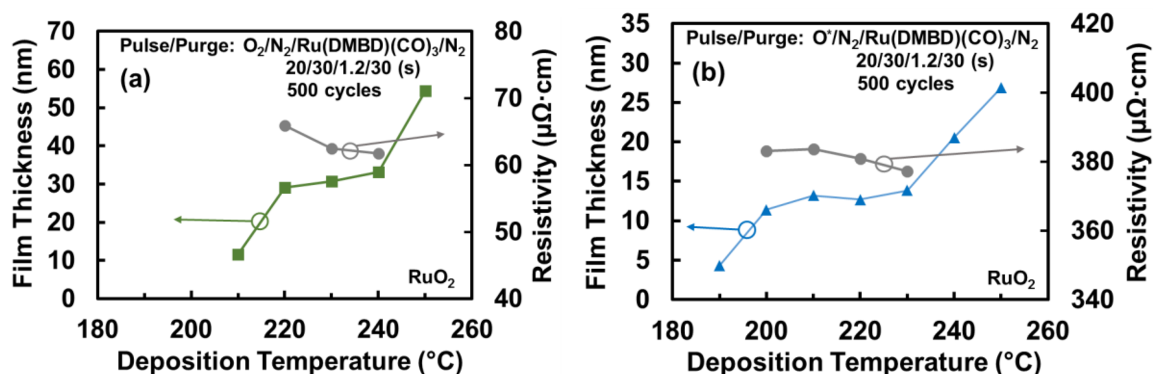

Figure 4.8: Film thickness and resistivity vs. deposition temperature for (a) thermal ALD and (b) PEALD of RuO_2.

$Ru(DMBD)(CO)_3$ pulse saturation curves for both thermal and PEALD processes using 20 s O_2 pulses are shown in Figure 4.9a. Saturation occurred at roughly the same precursor pulse length for both processes, at around 0.8 s for the thermal O_2 process and approximately 1.0 s for the PEALD process. The $Ru(DMBD)(CO)_3$ saturation behavior was not substantially different at 20 or 30 s O_2 pulse lengths. Experiments were also performed to examine the O_2 pulse saturation, as shown in Figure 4.9b for the thermal O_2 process. Saturation of the O_2 pulse time occurred at approximately 20 s. Films deposited

with a shorter 5 s pulse time exhibit reduced resistivity (~40 μΩ cm), indicating a more metallic character.

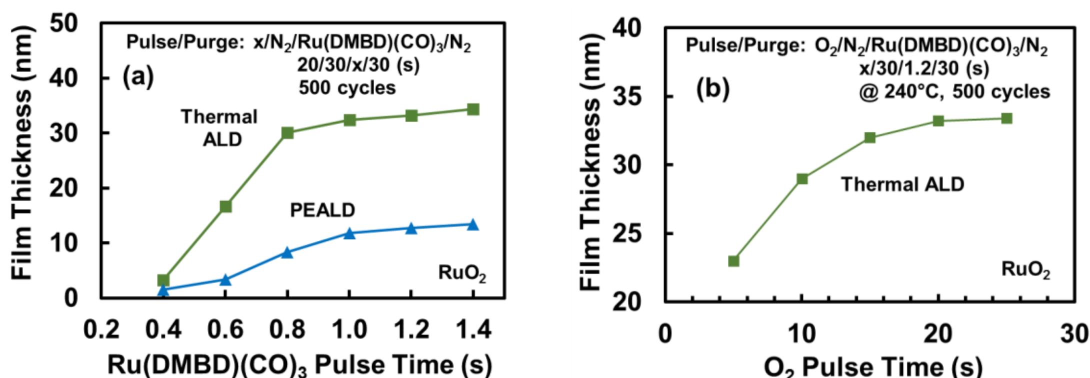

Figure 4.9: (a) Ru(DMBD)$(CO)_3$ pulse time saturation curve for thermal ALD (green squares) and PEALD (blue triangles) of RuO_2 and (b) O_2 pulse time saturation curve for thermal ALD of RuO_2.

The deposition rates for the two processes were found to be significantly different. Shown in Figure 4.10 is a plot of RuO_2 film thickness versus the number of ALD cycles for both ALD and PEALD. Thermal ALD (0.065 nm/cycle) had more than double the GPC of PEALD (0.029 nm/cycle). The nucleation delay, estimated by extrapolating a linear fit back to the x-axis, was also better for the thermal ALD process, being approximately 35 cycles for thermal ALD and roughly 76 cycles for PEALD.

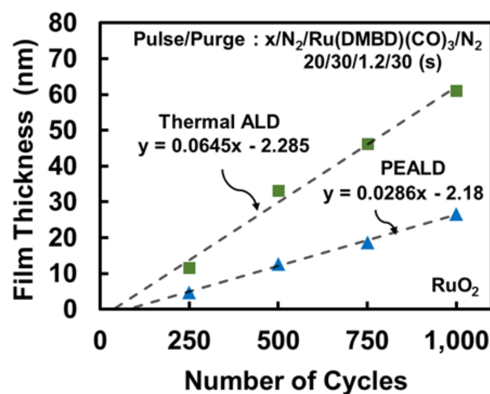

Figure 4.10: Film thickness vs. the number of ALD cycles for thermal ALD (green squares) and PEALD (blue triangles) of RuO_2.

The analysis of a 20 nm thick RuO_2 film deposited at 240°C was performed using XPS and AES, shown in Figure 4.11. The film was sputtered using 2 keV argon ions for 30 s to the approximate the midpoint depth of the film. Peaks for the Ru $3d_{5/2}$ and Ru $3d_{3/2}$ ionizations were observed at 280.3 and 284.5 eV, respectively, which are consistent with RuO_2 and distinct from other oxides of Ru.[42] The O 1s peak was detected at 529.7 eV. The film composition was measured at 34.7% Ru and 65.2% O, which indicates slightly Ru-rich films. Preferential sputtering of oxygen is the likely cause of deviation from the expected RuO_2 stoichiometry. Because of the overlap of the C 1s region with the Ru $3d_{3/2}$ region, carbon could not be easily quantified by XPS. Inspection of the AES spectrum in the region of the C KLL transition revealed that carbon was below the detection limit.

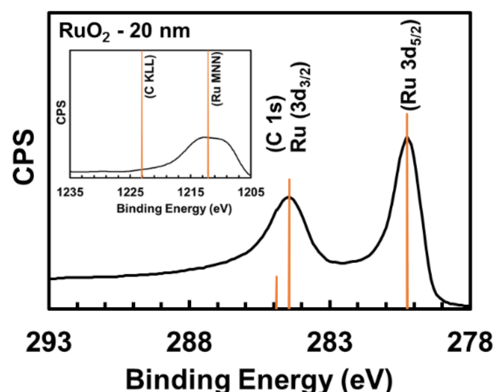

Figure 4.11: High-resolution XPS spectrum of Ru $3d_{5/2}$ and Ru $3d_{3/2}$ ionizations of an ALD RuO_2 film with an inset of the high-resolution AES region for C KLL and Ru MNN.

Shown in Figure 4.12 are GIXRD scans of intensity versus 2θ for ~12 nm thick RuO_2 films deposited using either thermal ALD at 240°C or PEALD at 230°C. The crystal structure of the films showed significant differences. The thermal ALD RuO_2 film exhibited a strong set of peaks corresponding to the rutile (tetragonal) phase with an

average Scherrer estimated grain size of ~3.6 nm, whereas the PEALD RuO_2 showed only one minor peak, the 54° (211) peak of the rutile phase. In Figure 4.13, AFM images of the same films showed that the thermal ALD film has a surface RMS roughness (0.6 nm) slightly higher than that of the PEALD film (0.4 nm). XRR measurements of the same films also showed the ALD RuO_2 to be at 6.77 g/cm^3, just below bulk rutile (tetragonal) RuO_2 (6.97 g/cm^3), while the PEALD RuO2 was at 7.91 g/cm^3.

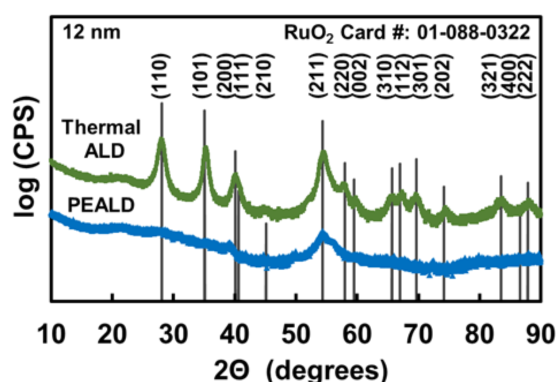

Figure 4.12: GIXRD plots of log intensity vs. 2θ for 12 nm thick RuO_2 films via thermal ALD (green squares) and PEALD (blue triangles) deposited at 240 and 230°C, respectively.

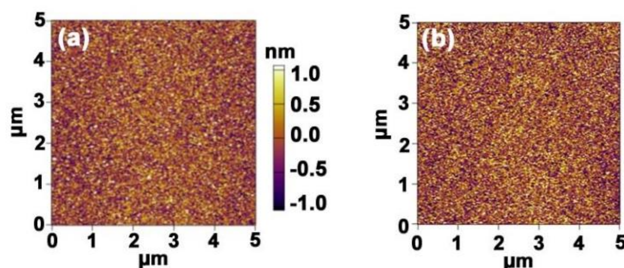

Figure 4.13: AFM images of 12 nm thick (a) thermal ALD and (b) PEALD RuO_2 films deposited at 240 and 230°C, respectively.

4.4 Discussion

4.4.1 Ru Process

The Ru process pulse saturation behavior in Figure 4.3a exhibited a higher deposition rate at a 1.2 s Ru(DMBD)$(CO)_3$ pulse length, prior to eventual saturation at

1.5 s. This sort of behavior is sometimes an indication of self-etching of the deposited film.[43] However, the increased deposition rate was accompanied by an increased resistivity (~30 μΩ cm at 1.2 s). Depending on the surface morphology, oxygen can penetrate beneath Ru film surfaces at temperatures as low as 250°C.[44] As described by Aaltonen et al., this subsurface oxygen that is incorporated during the O_2 pulse (and remains through the N_2 purge) is mobile and can participate in oxidative decomposition of ligands during the subsequent Ru(DMBD)$(CO)_3$ pulse.[45] If this subsurface O_2 is completely consumed during the Ru precursor pulse, Ru may be deposited. If it is not completely consumed, then RuO_2 (thermodynamically favored at the deposition temperature[46]) may result. The increased deposition rate and resistivity at 1.2 s Ru precursor pulse lengths thus point toward incorporation of oxygen into the film to form substoichiometric RuO_x, likely due to incomplete consumption of the subsurface oxygen during the Ru precursor pulse.[10,17,45] This is consistent with the O_2 pulse time dependence (Figure 4.3b), which exhibited an increasing film thickness accompanied by an increasing resistivity. For fixed 1.5 s Ru precursor pulses, the continued increase in deposition rate at 4 s of O_2 pulse time could have been due to a larger O_2 reservoir in the subsurface available for reaction during the Ru precursor pulse, again resulting in RuO_x.

Table 4.1 contains a summary of thermal ALD Ru processes to date that have used O_2 as a co-reactant, including the precursor, nucleation delay, GPC, ALD temperature window, and film resistivity. In this work, Ru films were deposited using Ru(DMBD)$(CO)_3$ and O_2. A saturating growth rate of 0.067 nm/cycle with a negligible nucleation delay on SiO_2 was observed within an ALD temperature window of 290-320°C. The GPC and ALD windows were comparable to or higher than the other Ru(0)

ALD precursors listed in Table 4.1. The negligible nucleation delay found for $Ru(DMBD)(CO)_3$ was much less than the ~210 cycles observed for $Ru(EtCp)_2$ when it was deposited without NH_3 plasma and also shorter than the long nucleation delays reported for other higher-oxidation state Ru precursors.[6-9,16-27] The negligible nucleation delay for $Ru(DMBD)(CO)_3$ is as good as or better than those of previously reported Ru(0) precursors.[28-33] The generally short nucleation delays observed using Ru(0) precursors versus higher-oxidation state precursors in Table 4.1 are possibly due to a lower thermodynamic activation energy barrier.[28-33] A smaller barrier could be the result of the lack of reduction needed for the metal to achieve the Ru(0) form present in the final thin film material. It could also be due to the exclusively neutral ligands present on Ru(0) complexes, which are more susceptible to dissociation than the anionic ligands that are found on higher-oxidation state Ru precursors.

Table 4.1: Comparison of Ruthenium Precursors for Thermal ALD Ru Processes Using O_2 as a Co-Reactant

Precursor	Metal Oxidation	Nucleation (Cycles)	Growth Rate (nm/Cycle)	ALD Window (°C)	Resistivity (μΩ·cm)	Reference Number
$Ru(thd)_3$	+3	~250	0.036	325-450	15-20	(17)
$Ru(EtCp)_2$	+2	~210(13)	0.049(13)	Uncertain(7)	15(13)	(6-9),(12),(13)
$Ru(Cp)_2$	+2	~250(16)	0.045(16)	325-375(16)	13(16)	(16),(18)
ECPR	+2	~25(20)	0.09(20)	Uncertain(20)	22-26(20)	(19),(20)
DMPR	+2	~60	0.022	250-320	18-24	(21)
Cyprus	+2	~20	0.05	250-310	20	(22)
$Ru(DMPD)_2$	+2	~40(23)	0.012(23)	185-210(23)	17(24)	(23),(24)
$Ru(Cp)(CO)_2Et$	+2	~85(25)	0.1(25)	300-325(26)	16(25)	(25),(26)
$(HD)^iPrMePhRu$	0	3	0.076	270-350	29-36	(28)
IMBCHDRu	0	~10(29)	0.089(29)	225-270(29)	30-40(29)	(29),(30)
EBCHDRu	0	3	0.1	200-275	18	(31)
EBECHDRu	0	3	0.042	175-275	20	(32)
EBBDRu	0	15	0.056	N/A	26	(33)
$Ru(DMBD)(CO)_3$	0	~0	0.067	290-320	14	This Work

Abbreviation: N/A, not available

The hexagonal Ru microstructure exhibits no RuO_2- associated peaks and an average crystal size of roughly 7.6 nm for an 8 nm thick film (Figure 4.5). Crystallite size has been shown to increase with film thickness because of a columnar microstructure that grows vertically.[23,37,47] The Ru film resistivity at 320°C was approximately 14 μΩ cm, roughly double the bulk Ru resistivity, but lower than or comparable to values from other reports of thin film ALD Ru, as indicated in Table 4.1. The low resistivity is consistent with phase purity and low carbon content (found to be below the detection limit of AES analysis). Finally, the RMS roughness of 0.6 nm for an 8 nm thick film (Figure 4.7) was also comparable to values from other reports.[28]

4.4.2 RuO_2 Process

Table 4.2 contains a summary of ALD RuO_2 processes to date, including the precursor, nucleation delay, GPC, ALD temperature window, and film resistivity. Using long (20 s) oxygen pulses and lower temperatures, RuO_2 films were deposited by both thermal and PEALD using $Ru(DMBD)(CO)_3$ and either O_2 or O_2 plasma, respectively. The temperature window for thermal ALD RuO_2 (220−240°C) is slightly higher than that of PEALD RuO_2 (200−230°C). Thermal RuO_2 exhibits a GPC higher than and a nucleation delay on SiO_2 substrates shorter than those of PEALD RuO_2, with 0.065 and 0.029 nm/cycle and 35 and 76 cycles, respectively. Many of the previous RuO_2 processes listed in Table 4.2 report growth rates that are greater than that typically observed for ALD (GPC $\lesssim$ 0.15 nm/cycle). As such, it is likely that they contain a CVD component. The GPC reported here is more typical of the submonolayer per cycle growth expected for a well-behaved ALD process. RuO_2 films grown in this work by thermal ALD show a

distinct rutile phase microstructure, a resistivity of ~62 μΩ cm, and a close to bulk density (6.97 g/ cm^3), whereas the PEALD RuO_2 films have less distinct crystallinity, much higher resistivity (~377 μΩ cm), and increased density (7.91 g/cm^3). This resistivity for thermal ALD RuO_2 is approximately half of what is reported for many of the other available RuO_2 capable precursors, listed in Table 4.2. Considering morphology, thermal ALD RuO_2 is preferred for templating the high-k rutile phase of TiO_2. Unlike other Ru(0) precursors, the thermal ALD RuO_2 grown using Ru(DMBD)$(CO)_3$ has no Ru metal peaks, which may improve its ability to template TiO_2. The reduced GPC and increased nucleation delay for the PEALD process are likely due to the use of oxygen plasma, which is known to etch RuO_2.[48] Likewise, the lack of crystal structure in the PEALD films may be also be due to the interruption of grain growth by oxygen plasma etching during deposition. This lack of crystal structure in turn likely accounts for the much higher resistivity and reduced surface roughness.

Table 4.2: Comparison of Ruthenium Precursors for RuO_2

Precursor	Metal Oxidation	Nucleation (Cycles)	Growth Rate (nm/Cycle)	ALD Window (°C)	Resistivity (μΩ·cm)	Reference Number
Ru(EtCp)$_2$	+2	~700$^{(6)}$	0.175$^{(9)}$	N/A	70$^{(9)}$	(6),(8),(9)
Ru(Cp)$_2$	+2	NA	0.32	N/A	270	(18)
Ru(DMPD)$_2$	+2	~125	0.023	N/A	NA	(23)
(HD)^{i}PrMePhRu	0	-50	0.15	180-200	275	(28)
EBCHDRu	0	2	0.186	N/A	118	(34)
EBBDRu	0	6	0.09	N/A	~140	(33)
Ru(DMBD)(CO)$_3$	0	35	0.065	220-240	62	This Work

Abbreviation: N/A, not available

4.4.3 Comparing Ru and RuO_2 Processes

In this work, both Ru and RuO_2 were deposited using the same Ru(DMBD)$(CO)_3$ precursor and O_2 reactant. To improve our understanding of why this is possible, the GPC

and resistivity versus temperature data from Figures 4.2 and 4.8 are combined in Figure 4.14. Whereas the window for the Ru process is from 290 to 320°C, the window for the RuO_2 process is from 220 to 240°C. The lower-temperature ALD window for RuO_2 as compared to Ru metal is consistent with the findings of Jung et al. for (1,5-hexadiene)(1-isopropyl-4-methylbenzene)Ru(0).[28] It has been reported previously that the formation of Ru films versus RuO_x films by CVD is dependent on both the temperature of deposition and the partial pressure of oxygen available at the surface of the growing film, where a clear delineation exists between the conditions necessary for the metal and the oxide.[46] Although it is perhaps not surprising for such a phase diagram to exist for CVD-grown materials, few examples of such reactivity occurring in an ALD process with a single precursor over a narrow temperature window exist.35This behavior, however, may be general for all metals for which the reduction potential from the oxide to the metallic form is positive relative to the standard hydrogen electrode.

With respect to the O_2 pulse time, the RuO_2 GPC saturates (as shown in Figure 4.9b) whereas the Ru GPC does not (Figure 4.3b). This is consistent with an ALD system in which the O_2 dose is a key determinant, along with temperature as described above, for whether Ru or RuO_2 is obtained. As predicted by Kang et al.[46], a large oxygen dose at lower temperatures provides RuO_2 films, whereas an oxygen-poor environment at higher temperatures result in low-resistivity Ru metal.

The growth rate and film properties for either process outside the ALD window also are informative. Again with respect to Figure 4.14, for Ru, the deposition rate decreases at temperatures below the ALD window. This decrease in deposition rate is accompanied by an increase in film resistivity, indicating formation of RuO_x. As the O_2

pulse is only 2 s long, the GPC of RuO_x is much lower than that for the 20 s O_2 pulse RuO_2 process. The deposition rate for RuO_2 increases above the ALD window. As oxygen becomes mobile above 250°C in RuO_2, longer O_2 pulses lead to an increased concentration of subsurface oxygen that can escape the film and react at the surface, causing CVD-like growth during the Ru pulse. It can be surmised that because carbonyl ligands are well-known to be labile and can dissociate from metals under mild conditions, a probable mechanism for reaction would involve loss of CO and the formation of a metal−surface bond. The fact that DMBD is both chelating and π-backbonding would help otherwise stabilize this surface functionalization between Ru precursor and O_2 exposures. It is proposed that the DMBD ligand would be retained on the ruthenium metal center subsequent to chemisorption and should be liberated or consumed only upon the subsequent co-reactant pulse. Thus, it is the supply of the co-reactant (O_2) from the subsurface that allows additional reaction during the Ru pulse.

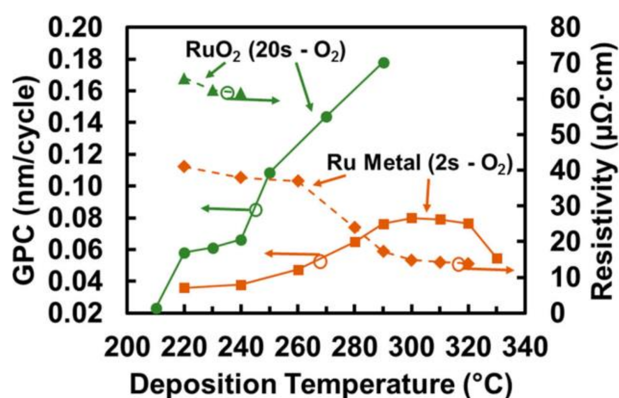

Figure 4.14: Comparison of GPC and resistivity vs. temperature for Ru and RuO_2 thermal ALD processes. The 20 s O_2 pulses are shown as green circles (GPC) and green triangles (resistivity) and the 2 s O_2 pulses as orange squares (GPC) and orange diamonds (resistivity).

4.5 Summary and Conclusions

We have investigated the suitability of a zero-oxidation state precursor, η^4-2,3-dimethylbutadiene ruthenium tricarbonyl [Ru(DMBD)$(CO)_3$], with regard to both Ru and RuO_2 film growth. Ru films were successfully deposited with thermal ALD. Using 2 s pulses of O_2, a saturating growth rate of 0.067 nm/cycle with negligible nucleation delay is observed within an ALD temperature window of 290−320°C. The Ru metal shows a strong hexagonal crystal structure with a low resistivity of approximately 14 μΩ cm at 20°C and a fairly smooth surface roughness of ~0.6 nm for 8 nm thick films.

Using 20 s long oxygen pulses and lower temperatures, RuO_2 films were deposited by both thermal and PEALD using O_2 or O_2 plasma. The temperature window for thermal ALD RuO_2 (220−240°C) is slightly higher than that of PEALD RuO_2 (200−230°C). Thermal RuO_2 exhibits a GPC higher than and a nucleation delay on SiO_2 substrates shorter than those of PEALD RuO_2, with 0.065 and 0.029 nm/cycle and 35 and 76 cycles, respectively. RuO_2 films grown by thermal ALD also show distinct rutile phase microstructure with a resistivity of ~62 μΩ cm, a density close to bulk, and RMS roughness of 0.6 nm for 12 nm thick films. PEALD RuO_2 films exhibit less distinct crystallinity with much higher resistivity. The lower growth rate, longer nucleation delay, and higher resistivity are likely due to O_2 plasma etching of the growing RuO_2 film.

Overall, Ru(DMBD)$(CO)_3$ appears to be a promising precursor for thermal ALD of both Ru and RuO_2 thin films. Processes based on this precursor offer the advantages typical for ALD but also provide improvements over many of the known processes for these materials, including resistivity and nucleation behavior. In addition, the potential ability of the deposited morphology to be used as a template for rutile TiO_2 may facilitate

fabrication of high-k MIM capacitors. Considering the emerging applications for Ru-containing thin film materials for various architectures anticipated in future ULSI device nodes, the work presented here is an important addition to the existing reported methods.

4.6 Acknowledgments

The authors thank J. McGlone for AFM characterization, C. Tasker for equipment support, T. Mueller for performing XPS analysis, and ON Semiconductor and the Oregon Nanoscience and Microtechnologies Institute (ONAMI) for partial financial support. Part of this work was conducted at the Materials Synthesis and Characterization (MaSC) Center, a National Nanotechnology Coordinated Infrastructure (NNCI) Northwest Nanotechnology Infrastructure (NWNI) user facility at Oregon State University, which is supported in part by the National Science Foundation (Grant ECC-1542101) and Oregon State University.

4.7 References

[1] M.W. Lane, C.E. Murray, F.R. McFeely, P.M. Vereecken, and R. Rosenberg, Appl. Phys. Lett. 83, 2330 (2003).

[2] J.H. Han, S. Han, W. Lee, S.W. Lee, S.K. Kim, J. Gatineau, C. Dussarrat, and C.S. Hwang, Appl. Phys. Lett. 99, 022901 (2011).

[3] B. Hudec, K. Hušeková, E. Dobročka, J. Aarik, R. Rammula, A. Kasikov, A. Tarre, A. Vincze, and K. Fröhlich, J. Vac. Sci. Technol. B Microelectron. Nanometer Struct. 29, 01AC09 (2011).

[4] K. Frohlich, B. Hudec, M. Tapajna, K. Husekova, A. Rosova, P. Elias, J. Aarik, R. Rammula, A. Kasikov, T. Arroval, L. Aarik, K. Murakami, M. Rommel, and A.J. Bauer, ECS Trans. 50, 79 (2013).

[5] A.O. Ibidunni, Oxid. Met. 40, 5 (1993).

[6] A. Salaün, S.B. Newcomb, I.M. Povey, M. Salaün, L. Keeney, A. O'Mahony, and M.E. Pemble, Chem. Vap. Depos. 17, 114 (2011).

[7] W.-H. Kim, S.-J. Park, D. Kim, and H. Kim, J. Korean Phys. Soc. 55, 32 (2009).

[8] O.-K. Kwon, J.-H. Kim, H.-S. Park, and S.-W. Kang, J. Electrochem. Soc. 151, G109 (2004).

[9] S.-H. Kwon, O.-K. Kwon, J.-H. Kim, S.-J. Jeong, S.-W. Kim, and S.-W. Kang, J. Electrochem. Soc. 154, H773 (2007).

[10] J.-H. Kim, D.-S. Kil, S.-J. Yeom, J.-S. Roh, N.-J. Kwak, and J.-W. Kim, Appl. Phys. Lett. 91, 052908 (2007).

[11] J.W. Kim, K.S. Son, B. Kim, W. Kim, and J.H. Shim, ECS Trans. 50, 165 (2013).

[12] S.-J. Park, W.-H. Kim, H.-B.-R. Lee, W.J. Maeng, and H. Kim, Microelectron. Eng. 85, 39 (2008).

[13] S.-S. Yim, D.-J. Lee, K.-S. Kim, S.-H. Kim, T.-S. Yoon, and K.-B. Kim, J. Appl. Phys. 103, 113509 (2008).

[14] T. Aoyama and K. Eguchi, Jpn. J. Appl. Phys. 38, L1134 (1999).

[15] Y. Matsui, M. Hiratani, T. Nabatame, Y. Shimamoto, and S. Kimura, Electrochem. Solid-State Lett. 5, C18 (2002).

[16] T. Aaltonen, P. Alén, M. Ritala, and M. Leskelä, Chem. Vap. Depos. 9, 45 (2003).

[17] T. Aaltonen, M. Ritala, K. Arstila, J. Keinonen, and M. Leskelä, Chem. Vap. Depos. 10, 215 (2004).

[18] S.-J. Park, W.-H. Kim, W.J. Maeng, Y.S. Yang, C.G. Park, H. Kim, K.-N. Lee, S.-W. Jung, and W.K. Seong, Thin Solid Films 516, 7345 (2008).

[19] K. Kukli, M. Kemell, E. Puukilainen, J. Aarik, A. Aidla, T. Sajavaara, M. Laitinen, M. Tallarida, J. Sundqvist, M. Ritala, and M. Leskelä, J. Electrochem. Soc. 158, D158 (2011).

[20] M. Knaut, M. Junige, M. Albert, and J.W. Bartha, J. Vac. Sci. Technol. Vac. Surf. Films 30, 01A151 (2012).

[21] K. Kukli, J. Aarik, A. Aidla, I. Jõgi, T. Arroval, J. Lu, T. Sajavaara, M. Laitinen, A.-A. Kiisler, M. Ritala, M. Leskelä, J. Peck, J. Natwora, J. Geary, R. Spohn, S. Meiere, and D.M. Thompson, Thin Solid Films 520, 2756 (2012).

[22] K. Gregorczyk, L. Henn-Lecordier, J. Gatineau, C. Dussarrat, and G. Rubloff, Chem. Mater. 23, 2650 (2011).

[23] R. Methaapanon, S.M. Geyer, H.-B.-R. Lee, and S.F. Bent, J. Mater. Chem. 22, 25154 (2012).

[24] O. van der Straten, S.M. Rossnagel, J.P. Doyle, and K.P. Rodbell, ECS Trans. 1, 51 (2006).

[25] N. Leick, R.O.F. Verkuijlen, L. Lamagna, E. Langereis, S. Rushworth, F. Roozeboom, M.C.M. van de Sanden, and W.M.M. Kessels, J. Vac. Sci. Technol. Vac. Surf. Films 29, 021016 (2011).

[26] S.K. Park, R. Kanjolia, J. Anthis, R. Odedra, N. Boag, L. Wielunski, and Y.J. Chabal, Chem. Mater. 22, 4867 (2010).

[27] N. Leick, S. Agarwal, A.J.M. Mackus, and W.M.M. Kessels, Chem. Mater. 24, 3696 (2012).

[28] H.J. Jung, J.H. Han, E.A. Jung, B.K. Park, J.-H. Hwang, S.U. Son, C.G. Kim, T.-M. Chung, and K.-S. An, Chem. Mater. 26, 7083 (2014).

[29] S.-H. Choi, T. Cheon, S.-H. Kim, D.-H. Kang, G.-S. Park, and S. Kim, J. Electrochem. Soc. 158, D351 (2011).

[30] T.-K. Eom, W. Sari, K.-J. Choi, W.-C. Shin, J.H. Kim, D.-J. Lee, K.-B. Kim, H. Sohn, and S.-H. Kim, Electrochem. Solid-State Lett. 12, D85 (2009).

[31] S. Yeo, S.-H. Choi, J.-Y. Park, S.-H. Kim, T. Cheon, B.-Y. Lim, and S. Kim, Thin Solid Films 546, 2 (2013).

[32] T.E. Hong, S.-H. Choi, S. Yeo, J.-Y. Park, S.-H. Kim, T. Cheon, H. Kim, M.-K. Kim, and H. Kim, ECS J. Solid State Sci. Technol. 2, P47 (2013).

[33] S. Yeo, J.-Y. Park, S.-J. Lee, D.-J. Lee, J.H. Seo, and S.-H. Kim, Microelectron. Eng. 137, 16 (2015).

[34] J.-Y. Park, S. Yeo, T. Cheon, S.-H. Kim, M.-K. Kim, H. Kim, T.E. Hong, and D.-J. Lee, J. Alloys Compd. 610, 529 (2014).

[35] J. Hämäläinen, M. Ritala, and M. Leskelä, Chem. Mater. 26, 786 (2014).

[36] Y.W. Song, J. Lee, K. Lee, Y. Lee, and H.K. Jang, ECS Trans. 2, 1 (2006).

[37] T. Cheon, S.-H. Choi, S.-H. Kim, and D.-H. Kang, Electrochem. Solid-State Lett. 14, D57 (2011).

[38] F. Basolo, Polyhedron 9, 1503 (1990).

[39] I. Noda, H. Yasuda, and A. Nakamura, J. Organomet. Chem. 250, 447 (1983).

[40] K. L. Amos and N. G. Connelly, J. Organomet. Chem. 194, C57 (1980).

[41] O. Gambino, M. Valle, S. Aime, and G.A. Vaglio, Inorganica Chim. Acta 8, 71 (1974).

[42] D.M. Price, Thermochim. Acta 367–368, 253 (2001).

[43] F. Cardarelli, *Materials Handbook: A Concise Desktop Reference*, 2nd ed (Springer, London, 2008).

[44] M. Ritala, K. Kukli, A. Rahtu, P.I. Raisanen, M. Leskela, T. Sajavaara, and J. Keinonen, Science 287, 319 (2000).

[45] A. Böttcher and H. Niehus, J. Chem. Phys. 110, 3186 (1999).

[46] T. Aaltonen, A. Rahtu, M. Ritala, and M. Leskelä, Electrochem. Solid-State Lett. 6, C130 (2003).

[47] S.Y. Kang, K.H. Choi, S.K. Lee, C.S. Hwang, and H.J. Kim, J. Electrochem. Soc. 147, 1161 (2000).

[48] J. Choi, Y. Choi, J. Hong, H. Tian, J.-S. Roh, Y. Kim, T.-M. Chung, Y.W. Oh, Y. Kim, C.G. Kim, and K. No, Jpn. J. Appl. Phys. 41, 6852 (2002).

[49] W. Pan and S.B. Desu, Phys. Status Solidi A 161, 201 (1997).

5 ATOMIC LAYER DEPOSITION OF TiO_2/Al_2O_3 METAL-INSULATOR-METAL CAPACITORS

Dustin Z. Austin, Konner Holden, Michael Hayes, and John F. Conley, Jr.

In preparation for submission

5.1 Introduction

Back end of line (BEOL) metal-insulator-metal capacitors (MIMCAPs) are critical components in modern integrated circuits. Scaling for analog and mixed signal (AMS) applications require an increasing capacitance density (C) while maintaining low current density (J) and low voltage nonlinearity (characterized by the quadratic voltage coefficient of capacitance, α_{VCC}). The α_{VCC} is empirically determined by fitting a parabolic expression to the capacitance versus voltage measurement:

$$\Delta C/C_0 = \alpha_{VCC} V^2 + \beta_{VCC} V, \tag{5.1}$$

where C_0 is the parallel plate capacitance at 0 V, $C_0 = \frac{\varepsilon_0 \kappa}{d_{ox}}$, ε_0 is the permittivity of vacuum, κ is the relative dielectric constant, d_{ox} is the dielectric thickness, $\Delta C = C(V) - C_0$ is the change in capacitance at a given applied bias, and β_{VCC} is the linear voltage coefficient of capacitance. As projected by the 2020 node of the International Technology Roadmap for Semiconductors (ITRS), a C of 10 fF/μm^2 is needed, while simultaneously meeting J at 1 V less than 10 nA/cm^2 and an α_{VCC} less than 100 ppm/V^2.[1] Additionally BEOL processing requires temperatures of no more than ~400ºC in order to preserve front end of line dopant profiles.[2]

It has been demonstrated that single insulators are incapable of meeting future ITRS C_0 targets while simultaneously maintaining low α_{VCC} and low J.[3–5] This is because decreasing the d_{ox} or introducing high-κ materials both lead to increased leakage current and increased voltage nonlinearity (α_{VCC} scales with d_{ox}^{-2} and linearly with the κ).[6–8] A promising method for scaling in MIMCAPs is the use of multi-insulator stacks.[6] Multi-insulator stacks combine complementary insulating materials that target separate device

parameters. One of the primary advantages of this technique is the "cancelling effect," the use of two or more dielectrics with opposing α_{VCC} signs to control the overall device α_{VCC}. For example, a bi-layer insulator stack may be optimized by pairing a dielectric with high-κ and positive α_{VCC} but with high leakage with a second insulator that has low leakage and a negative α_{VCC} but a lower κ.

Previous literature has reported several multi-insulator stacks that successfully employ the cancelling technique to meet all three device parameters for future ITRS node. Many of these studies, however, use either uncommon materials, non-industry standard deposition methods, or are processed above the BEOL temperature limit.[6,8–13] Optimization of α_{VCC} via the cancelling technique requires precise thickness control. Atomic layer deposition (ALD), based on purge separated self-limiting half reactions provides inherent atomic scale thickness control at low temperatures. We recently demonstrated that bi-layer stacks of Al_2O_3 and SiO_2, deposited at 200°C via plasma enhanced atomic layer deposition (PEALD), are able to meet the ITRS 2020 node with J (1 V) = 6.79 nA/cm^2, α_{VCC} = -20 ppm/V^2, and C_0 = 10.1 fF/μm^2. However, the Al_2O_3/SiO_2 stack could not be scaled further as the leakage J for the device targeting the ITRS 2023 node of C_0 = 12 fF/μm^2 exceeded the J = 10 nA/cm^2 at 1 V limit.[3] In addition, as the individual layer thicknesses for this bi-layer stack were only 3.7 nm (Al_2O_3) and 1.9 nm (SiO_2), subnanometer variations in the thickness of either layer produced significant variation in C and α_{VCC}. Thus, to increase total d_{ox} and push beyond the 2020 node, complementary insulator stacks utilizing higher-κ materials are needed. Rutile TiO_2 is particularly attractive as it is one of only a few materials to exhibit a negative sign α_{VCC} and it possesses a large κ of ~100.[14,15] As rutile TiO_2 can be difficult

to deposit within the BEOL temperature limit, rutile RuO_2 lower electrodes are needed to template and promote rutile morphology at lower deposition temperatures. Replacing the negative α_{VCC} SiO_2 layer ($\kappa = 4.7$) with TiO_2 should enable greater capacitance densities, while still taking advantage of the large bandgap of Al_2O_3.

In the present work, ALD is used to fabricate TiO_2 and TiO_2/Al_2O_3 bi-layers for use in BEOL MIMCAPs. The impact of TaN vs. RuO_2 bottom electrodes on the dielectric constant and morphology of the single layer TiO_2 devices is investigated. The C_0, J at 1V, and α_{VCC} of TiO_2/Al_2O_3 MIIMCAPs are benchmarked against future ITRS projections.

5.2 Experimental

MIM devices were fabricated on Si/SiO_2 (550 nm)/Ta (20 nm)/TaN (150 nm) substrates with the TaN layer planarized via chemical mechanical polishing. ALD RuO_2 lower electrodes were deposited on TaN to reduce the series resistance of the contact, as RuO_2 was only approximately 10 nm thick to maintain low surface roughness. ALD of RuO_2 was performed at 220°C using 200 cycles of alternating N_2-purge-separated pulses of O_2 and η^4-2,3-dimethylbutadiene ruthenium tricarbonyl [Ru(DMBD)$(CO)_3$].[16] PEALD of TiO_2 was performed using alternating N_2-purge-separated pulses of oxygen plasma and titanium tetrachloride ($TiCl_4$) at 400°C. ALD of Al_2O_3 was performed using alternating N_2-purge-separated pulses of H_2O and trimethylaluminum (TMA) at 250°C. Both ALD and PEALD processes were performed in a Picosun SUNALE R-200 reactor at ~5 Torr. TiO_2 was deposited first to take advantage of substrate templating from rutile RuO_2. PEALD was chosen over thermal ALD to deposit TiO_2 as the extra energy from plasma may help to promote the growth of TiO_2 in the rutile phase over anatase phase at lower deposition temperatures. Post-deposition annealing of TiO_2 was performed in a tube

furnace at 400°C for 30 min while flowing 40 sccm of O_2. It is worth noting that the best results were observed with anneals conducted after TiO_2 deposition but before Al_2O_3 deposition. 150 nm thick top contacts were evaporated with ~0.05 mm^2 area dots defined via shadow mask. Al was used with bi-layer devices, but Ag was used with single layer TiO_2 devices as Al was found to form an interfacial layer with TiO_2 which modified the electrical properties. The area of each device was measured and used for area normalizations. The average error in the area measurement is found to be +/- 1.8%. Film thickness was measured using a J.A. Woollam M2000 spectroscopic ellipsometer (SE) in the range of 400-1000 nm. Film morphology was investigated via grazing incidence X-ray diffraction (GIXRD) using a Rigaku Ultima IV instrument with Cu Kα radiation (λ = 1.5406 Å). Electrical measurements were taken in a probe station in a dark box using a B1500A semiconductor device parameter analyzer and an E4980A LCR meter. All electrical tests were conducted with the bottom electrode held at ground. CV measurements were taken at 100 kHz and swept to approximately one-half the dielectric breakdown voltage to avoid excessive stress during testing. CV and IV measurements were performed at sweep rates of 0.2 V/s.

5.3 Results and Discussion

The preferred phase of TiO_2 for MIMCAP applications is rutile, as it has a lower J and a much higher κ than the anatase phase, ~50 vs. ~100, respectively.[14] Rutile TiO_2 is typically stable only above ~600ºC, which exceeds the thermal budget of most BEOL processes. Recently, however, it has been shown that due to a small lattice mismatch, a rutile RuO_2 or IrO_2 bottom electrode may be used to template the rutile phase of TiO_2 at a reduced temperature.[17] As TTIP begins to decompose above ~350ºC, $TiCl_4$ was chosen to

deposit TiO_2 due to decomposition temperatures greater than 400ºC. Below 400ºC TiO_2 was found to be more anatase phase TiO_2 with either precursor.

Shown in Fig. 5.1 are GIXRD scans of 400 cycle PEALD TiO_2 films on (a) TaN and (b) RuO_2 electrodes, as well as reference scans for each metal electrode. Immediately after TiO_2 deposition, films were annealed at 400°C for 30 min in O_2. In Fig. 5.1(a), the TiO_2 on TaN scan (grey) matches up well with anatase TiO_2, with various peaks from the TaN (blue) lower electrode also appearing. In Fig. 5.1(b), the TiO_2 on RuO_2 scan (orange) matches well with rutile TiO_2 but is difficult to discern from the rutile RuO_2 lower electrode reference scan (green). One peak stands out at ~44°, which lines up with rutile TiO_2 and not directly with either rutile RuO_2 or any of the anatase TiO_2 peaks. From ellipsometry measurements, it was found that the 400 PEALD cycles resulted in ~21 nm of TiO_2 on RuO_2, but only ~16 nm of TiO_2 on TaN. The difference in thicknesses between the two substrates is consistent with reported TiO_2 rutile versus anatase phase growth rates of 0.055 nm/cycle versus 0.035 nm cycle, respectively.[18,19] Taken together, the XRD and ellipsometry results strongly suggest that ALD RuO_2 using $Ru(DMBD)(CO)_3$[16] is able to effectively template the rutile phase of TiO_2 within the BEOL temperature limit of 400ºC, whereas for the same deposition parameters using a TaN bottom electrode produces the anatase phase of TiO_2. Note that if the 400°C post deposition anneal is performed after Al_2O_3 deposition or after metallization, then rutile phase is not formed.

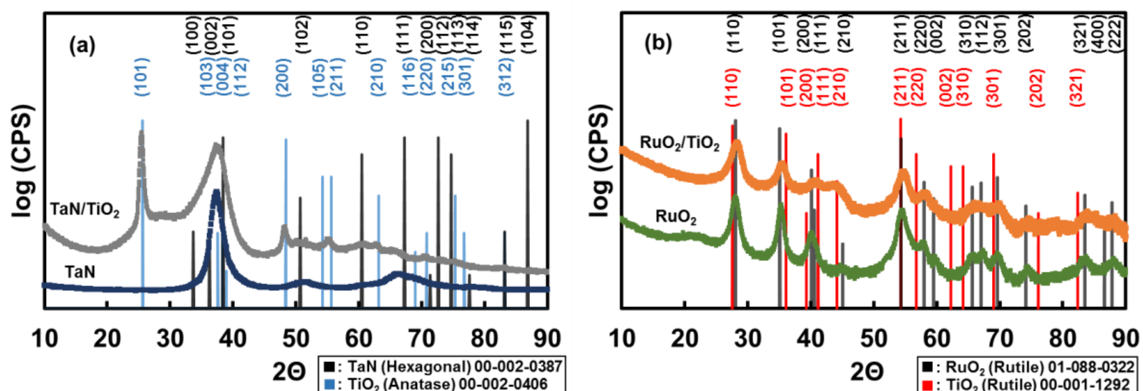

Figure 5.1: GIXRD of annealed 400 cycle TiO_2 on either (a) TaN or (b) RuO_2 lower electrodes, with reference spectra included for each metal.

Shown in Fig. 5.2 are plots of (a) C vs. V and (b) J vs. E comparing the 400 cycle PEALD TiO_2 films deposited on either TaN or RuO_2 bottom electrodes. Again, structures were annealed at 400°C for 30 min in O_2 immediately following TiO_2 deposition but prior to top Al electrode metallization. Looking first at capacitance in Fig. 5.2 (a), the RuO_2 templated TiO_2 exhibits a C_0 of ~37.5 fF/µm^2, corresponding to $\kappa \approx 89$ which is roughly in line with expectations for rutile TiO_2. The negative α_{VCC} of approximately -35,000 ppm/V^2 is also consistent with rutile TiO_2. On the other hand, the TiO_2 deposited directly on TaN has a lower C_0 of ~28.5 fF/µm^2 ($\kappa \approx 52$) and shows a positive α_{VCC} of approximately 29,000 ppm/V^2, with the κ consistent with anatase TiO_2. It should be noted that only roughly approximate α_{VCC} values could be estimated because the parabolic fit was poor in both instances.

Considering Fig. 5.2 (b), the leakage current density for the RuO_2 templated TiO_2 is lower than the leakage shown by TiO_2 deposited on TaN. The difference in leakage is also consistent with rutile vs. anatase for the TiO_2 deposited on RuO_2 vs. TaN, respectively. In addition, the considerably larger work function of RuO_2 (~5.1 eV)

compared to that of TaN (~4.6 eV) should lead to a larger metal-oxide barrier height at the RuO_2/TiO_2 interface as compared to the TaN/TiO_2 interface, according to the Schottky-Mott rule.[20] The larger barrier height reduces any thermionic emission contributions to electron flow at low electric fields and also accounts for some of the reduced leakage. The greater top-bottom electrode work function difference in the RuO_2 device is also likely responsible for the greater asymmetry in the I-V characteristics. The negative current is much lower because it must overcome a much larger built-in voltage in the TiO_2.

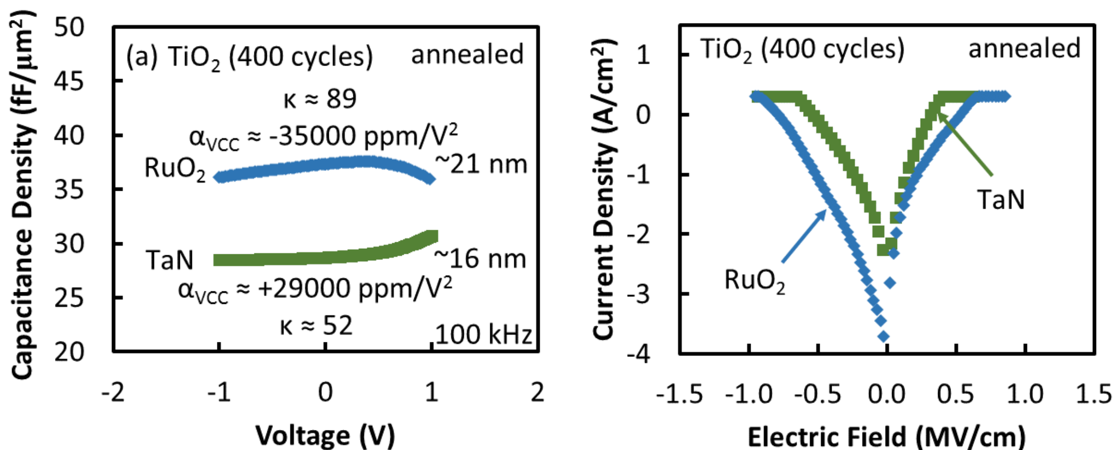

Figure 5.2: (a) Capacitance density vs. voltage and (b) Leakage current density vs. electric field for 400 PEALD cycles of annealed TiO_2 on either RuO_2 or TaN lower electrodes.

Having established the rutile phase, high-κ, low leakage, and negative α_{VCC} of TiO_2 on RuO_2, we next attempt to fabricate an ultralow α_{VCC} device via the canceling effect using Al_2O_3 as the positive α_{VCC} material. Shown in Fig. 5.3(a) are C vs. V plots for multiple devices of $RuO_2/TiO_2/Al_2O_3/Al$ MIMCAPs consisting of 400 cycles (roughly 21 nm) of TiO_2 and either 70, 75, or 80 cycles (roughly 4, 4.5, and 5 nm) of Al_2O_3. Annealing is once again performed immediately after the TiO_2 deposition. Summarized

in Table 5.1, C_0 ranges between roughly 11 fF/μm^2 for the 80 cycle Al_2O_3 device to 17 fF/μm^2 for the 70 cycle Al_2O_3 device. The device with 75 cycles of Al_2O_3 has a C_0 of 14.3 fF/μm^2 with an α_{VCC} of roughly 450 ppm/V^2 (however, a parabola does not characterize the voltage nonlinearity for these devices well). With only 5 additional Al_2O_3 cycles, the 80 cycle device has a C_0 of 11.2 fF/μm^2 with an α_{VCC} of approximately -580 ppm/V^2.

To better visualize α_{VCC}, a baseline adjusted (β_{VCC} removed) plot of normalized capacitance (C/C_0) vs. voltage for the 400c/70c device is shown in Fig. 5.3(b). This "w" shape has been observed in other multi-insulator stacks and has been explained by an opposing polarization contribution from each dielectric at different volages.[21] However, in dielectric pairs with significantly different κ and opposite sign α_{VCC}, it also found that this shape can be roughly reproduced by accounting for both the α_{VCC} dependence on layer thickness as well as the dependence of α_{VCC} on the voltage dropped across each layer, which in turn depends on the capacitance of that layer at a given applied voltage. The fact that neither a smooth positive or negative α_{VCC} is observed around 0 V suggests that other influences, such as the metal-dielectric interfaces (further investigated in chapter 6) and/or the internal dielectric-dielectric interface should be considered when α_{VCC} is close to being minimized.

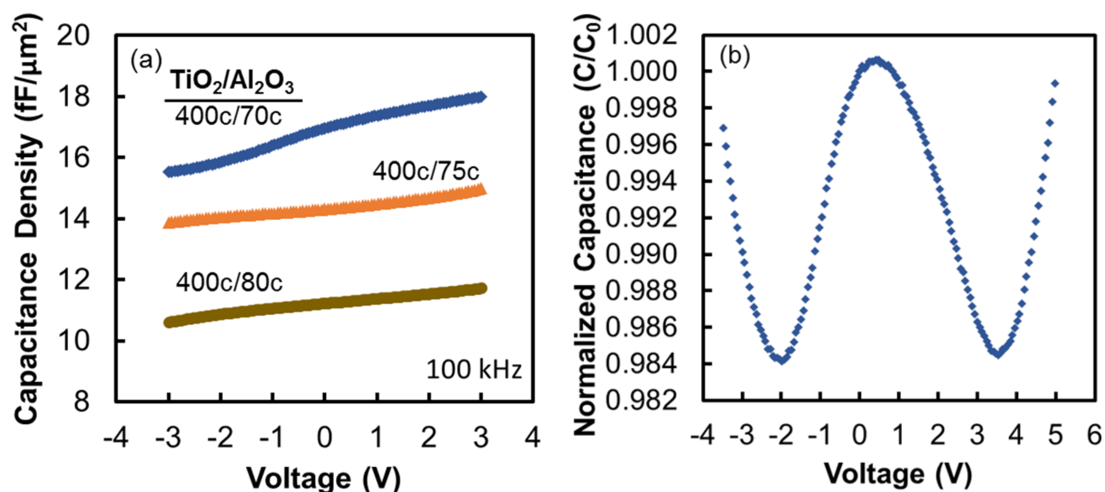

Figure 5.3: (a) Capacitance density vs. voltage for bi-layer stacks of TiO_2/Al_2O_3 with varying Al_2O_3 thicknesses and (b) Normalized capacitance (β_{VCC} removed) of the 400c/70c device clearly illustrating the 'w' curvature.

Shown in Fig. 5.4 are plots of J vs. V for MIMCAPS similar to those in Fig. 5.3 (summarized in Table 5.1). First, note that all the bilayer devices have approximately seven orders of magnitude lower leakage in the positive polarity as compared to single layer TiO_2 MIMCAPs. The 400c/75c device exhibits a J of 6.98 nA/cm^2 at 1 V, which meets the ITRS targets. There is a strong Fowler Nordheim tunneling component beyond ~3.25 V, which is commonly observed in ALD Al_2O_3 but not in ALD TiO_2.[22] The leakage J is controlled by the Al_2O_3 layer and very sensitive to its thickness. Reducing the Al_2O_3 layer by only 5 cycles to 70 cycles caused the J to exceed the 10 nA/cm^2 at 1 V limit, indicated by the black dashed lines. Increasing the Al_2O_3 layer by only 5 cycles to 80 cycles reduces the leakage further to 4.7 nA/cm^2 at 1 V, but results in a reduction of C_0 to 11.2 fF/μm^2. The 80 cycle device meets the ITRS 2023 capacitance density target and the 75 cycle device meets the 2020 target. Although neither device meets the +/- 100 ppm/V^2 α_{VCC} requirement, the fact that the 75 cycle devices has positive α_{VCC} and the 80

cycle device has negative α_{VCC} suggests that the Al_2O_3 thickness could be further optimized to reach that target.

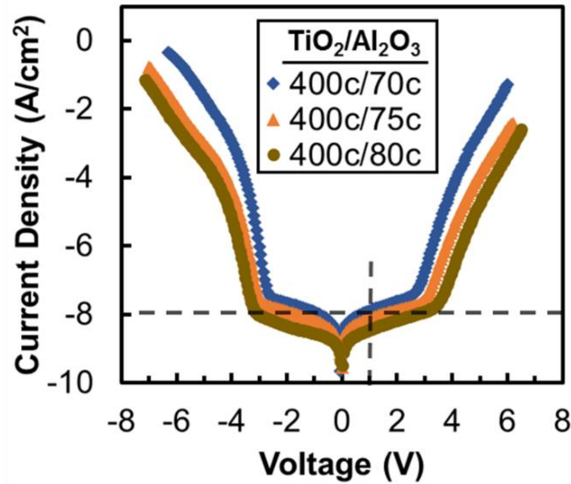

Figure 5.4: Leakage current density vs. voltage for bi-layer stacks of TiO_2/Al_2O_3 on RuO_2 lower electrodes.

Table 5.1: Summary of Devices Measurements

Cycles TiO_2/Al_2O_3	C/A ($fF/\mu m^2$)	α_{VCC} (ppm/V^2)	J at 1V (nA/cm^2)
ITRS 2023	12	< 100	< 10 .
ITRS 2020	10	< 100	< 10
400/70	17.0	770	15.7
400/75	14.3	~450	6.98
400/80	11.2	~-580	4.7

The stability of the rutile TiO_2 film is not generally discussed in previous studies.[15,23] Shown in Fig. 5.5 are C vs. V plots for 400 cycle / 75 cycle TiO_2/Al_2O_3 devices measured the same day as processing and again after two and three weeks at room temperature in an N_2 ambient (summarized in Table 5.2). Immediately after processing, this $RuO_2/TiO_2/Al_2O_3/Al$ device meets 2023 targets for both C_0 and J. The same device tested after two weeks of storage in an N_2 ambient exhibits reduced C_0 of

10.4 fF/μm^2, after which C_0 remains stable. This corresponds to an effective decrease in κ from 42 to 31, suggesting a partial phase transition from rutile to anatase TiO_2. Shown in Fig. 5.6, this phase transition is confirmed by GIXRD. After the 2-week stabilization, the device shows peaks for both rutile and antase phase TiO_2. Although C_0 drops significantly, the J is unchanged, indicating that the Al_2O_3 layer is unaffected and further illustrating the dominant limiting effect of the Al_2O_3 layer on charge transport. The 70 and 80 cycle devices exhibit a similar drop in C_0 with stable J. As α_{VCC} scales roughly linearly with κ, the negative α_{VCC} contribution of the TiO_2 layer is reduced with the reduction in κ, resulting in a reduction of α_{VCC} of the overall device to -45 ppm/V^2 in the range of -1 to 1.5 V. Thus, despite the reduction in C_0, this device meets 2020 ITRS nodes for C_0, J, and α_{VCC}, as well as the BEOL temperature limits. It is likely that the stabilization period could be significantly accelerated by optimal elevated temperature anneal.

To extend this stack into further out ITRS nodes, several potential strategies exist. One possibility is to stabilize the high-κ rutile TiO_2 phase by identifying a suitable dopant and concentration, as for doped HfO_2.[24] Our attempt to dope TiO_2 with Al, however, resulted in interruption of rutile growth and an effective device κ more in line with anatase TiO_2. Another possibility is reducing the thickness of TiO_2, which for ZrO_2 has been shown an effective method for stabilizing the high-κ phase against anneals.[25] Finally, since leakage is primarily dependent on the Al_2O_3 layer, it may be possible to reach the desired capacitance densities with a reduced thickness of the current stabilized mixed rutile-anatase phase TiO_2, which still exhibits a relatively high-κ.

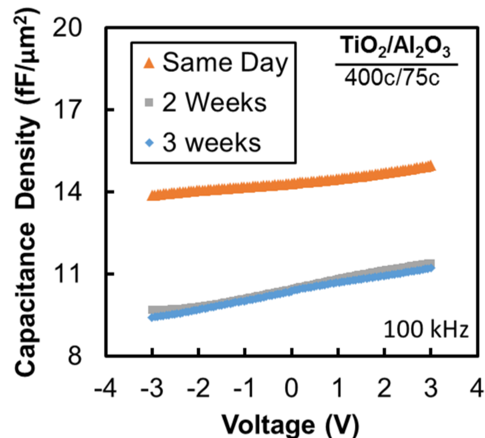

Figure 5.5: Capacitance density vs. voltage for the same TiO_2/Al_2O_3 (400 cycles / 75 cycles) device tested on the same day as deposition and again after two weeks.

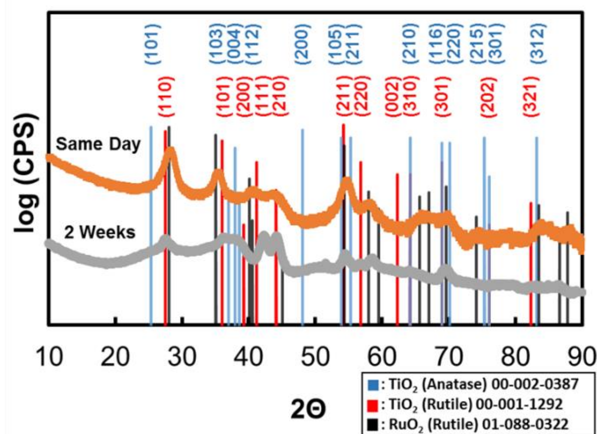

Figure 5.6: GIXRD of 400c/75c TiO_2/Al_2O_3 with device test same day as deposition and 2 weeks later.

Table 5.2: TiO_2/Al_2O_3 Stability

	C/A ($fF/\mu m^2$)	α_{VCC} (ppm/V^2)	J at 1V (nA/cm^2)
ITRS 2020	10	< 100	< 10
Same Day	14.3	~450	6.98
2 Weeks	10.4	-45	7.10
3 Weeks	10.3	-88	7.15

5.4 Conclusions

In this work, rutile TiO_2 was deposited via PEALD at 400°C using template assistance with PEALD rutile RuO_2 as the lower electrode. TiO_2 deposited under the same conditions on a TaN electrode was found to be anatase. Whereas the anatase TaN/TiO_2/Ag devices had a $\kappa \approx 52$ and a positive α_{VCC}, the rutile RuO_2/TiO_2/Ag devices exhibit $\kappa \approx 89$ and a negative α_{VCC}. The high-κ, negative α_{VCC} rutile TiO_2 was combined with positive α_{VCC}, wide band gap Al_2O_3 into a bilayer-insulator MIIM stack designed to maximize C_0, minimize J, and minimize α_{VCC} through the canceling effect. A RuO_2/TiO_2(~21 nm)/Al_2O_3(~4.5 nm)/Al device immediately after fabrication showed C_0 of 14.3 fF/μm^2, α_{VCC} of ~450 ppm/V^2, and J of 6.98 nA/cm^2 at 1 V. Room temperature stabilization resulted in a reduction in overall κ (C_0) and α_{VCC}, due to a partial phase transformation of the TiO_2 from rutile to anatase. Despite the reduction in C_0, leakage current density is limited by the Al_2O_3 layer and remained unchanged so that after stabilization the devices showed C_0 of 10.4 fF/μm^2, a leakage density of 7.11 nA/cm^2 at 1V, and an α_{VCC} of -45 ppm/V^2, meeting the projected requirements for the ITRS 2020 node. Further optimization of the film stack or stabilization of the rutile phase through doping may allow this device to meet ITRS 2023 projected requirements.

5.5 Acknowledgments

The authors thank C. Tasker for equipment support and the Oregon Nanoscience for partial financial support of this work. This work was conducted at the Materials Synthesis and Characterization (MaSC) Center, a National Nanotechnology Coordinated Infrastructure (NNCI) Northwest Nanotechnology Infrastructure (NWNI) user facility at

the Oregon State University which is supported in part by the National Science Foundation (grant ECC-1542101) and Oregon State University.

5.6 References

[1]The International Technology Roadmap for Semiconductors (ITRS), On-Chip Passives Technology Requirements (Semiconductor Industry Association, 2013).

[2] A. Farcy, J.-F. Carpentier, M. Thomas, J. Torres, and P. Ancey, Microelectron. Eng. **85**, 1940 (2008).

[3] D.Z. Austin, D. Allman, D. Price, S. Hose, and J.F. Conley Jr., IEEE Electron Device Lett. **36**, 496 (2015).

[4] X. Yu, C. Zhu, H. Hu, A. Chin, M.F. Li, B.J. Cho, D.-L. Kwong, P.D. Foo, and M.B. Yu, IEEE Electron Device Lett. **24**, 63 (2003).

[5] S.-Y. Lee, H. Kim, P.C. McIntyre, K.C. Saraswat, and J.-S. Byun, Appl. Phys. Lett. **82**, 2874 (2003).

[6] S.J. Kim, B.J. Cho, M.-F. Li, S.-J. Ding, C. Zhu, M.B. Yu, B. Narayanan, A. Chin, and D.-L. Kwong, IEEE Electron Device Lett. **25**, 538 (2004).

[7] N. Alimardani, S.W. King, B.L. French, C. Tan, B.P. Lampert, and J.F. Conley Jr., J. Appl. Phys. **116**, 024508 (2014).

[8] C. Jorel, C. Vallée, P. Gonon, E. Gourvest, C. Dubarry, and E. Defay, Appl. Phys. Lett. **94**, 253502 (2009).

[9] J.-J. Yang, J.-D. Chen, R. Wise, P. Steinmann, Y.-C. Yeo, and C. Zhu, IEEE Electron Device Lett. **30**, 1033 (2009).

[10] T.H. Phung, D.K. Srinivasan, P. Steinmann, R. Wise, M.-B. Yu, Y.-C. Yeo, and C. Zhu, J. Electrochem. Soc. **158**, H1289 (2011).

[11] J.H. Lee, Y.C. Lin, B.H. Chen, and C.Y. Tsai, in Solid-State Integr. Circuit Technol. ICSICT 2010 10th IEEE Int. Conf. On (IEEE, 2010), pp. 1024–1026.

[12] C.-C. Lin, Y.-H. Wu, R.-S. Jiang, and M.-T. Yu, IEEE Electron Device Lett. **34**, 1418 (2013).

[13] S.-U. Park, C.-Y. Kang, H.-M. Kwon, B.-S. Park, W.-H. Choi, I.-S. Han, G. Bersuker, R. Jammy, and H.-D. Lee, Microelectron. Eng. **88**, 3389 (2011).

[14] K. Frohlich, B. Hudec, M. Tapajna, K. Husekova, A. Rosova, P. Elias, J. Aarik, R. Rammula, A. Kasikov, T. Arroval, L. Aarik, K. Murakami, M. Rommel, and A.J. Bauer, ECS Trans. **50**, 79 (2013).

[15] J. Aarik, B. Hudec, K. Hušeková, R. Rammula, A. Kasikov, T. Arroval, T. Uustare, and K. Fröhlich, Semicond. Sci. Technol. **27**, 074007 (2012).

[16] D.Z. Austin, M.A. Jenkins, D. Allman, S. Hose, D. Price, C.L. Dezelah, and J.F. Conley Jr., Chem. Mater. **29**, 1107 (2017).

[17] M. Popovici, A. Delabie, C. Adelmann, J. Meersschaut, A. Franquet, M. Tallarida, J. van den Berg, O. Richard, J. Swerts, K. Tomida, M.-S. Kim, H. Tielens, H. Bender, T. Conard, M. Jurczak, S. Van Elshocht, and D. Schmeisser, ECS J. Solid State Sci. Technol. **2**, N23 (2012).

[18] G.-J. Choi, S.K. Kim, S.-J. Won, H.J. Kim, and C.S. Hwang, J. Electrochem. Soc. **156**, G138 (2009).

[19] J. Aarik, T. Arroval, L. Aarik, R. Rammula, A. Kasikov, H. Mändar, B. Hudec, K. Hušeková, and K. Fröhlich, J. Cryst. Growth **382**, 61 (2013).

[20] T. Tung, Appl. Phys. Rev. **1**, 011304 (2014).

[21] B. Zhu, W.-J. Liu, L. Wei, and S.-J. Ding, J. Phys. Appl. Phys. **49**, 135106 (2016).

[22] M.D. Groner, J.W. Elam, F.H. Fabreguette, and S.M. George, Thin Solid Films **413**, 186 (2002).

[23] K. Fröhlich, M. Ťapajna, A. Rosová, E. Dobročka, K. Hušeková, J. Aarik, and A. Aidla, Electrochem. Solid-State Lett. **11**, G19 (2008).

[24] T.S. Böscke, S. Govindarajan, P.D. Kirsch, P.Y. Hung, C. Krug, B.H. Lee, J. Heitmann, U. Schröder, G. Pant, B.E. Gnade, and W.H. Krautschneider, Appl. Phys. Lett. **91**, 072902 (2007).

[25] S. Abermann, C. Henkel, O. Bethge, G. Pozzovivo, P. Klang, and E. Bertagnolli, Appl. Surf. Sci. **256**, 5031 (2010).

6 ELECTRODE MODULATED CAPACITANCE-ELECTRIC FIELD NONLINEARITY IN METAL-INSULATOR-METAL CAPACITORS

Dustin Z. Austin, Konner Holden, Josh Hinz, and John F. Conley, Jr.

Accepted for publication in Applied Physics Letters

6.1 Introduction

Future nodes of back-end-of-line (BEOL) metal-insulator-metal capacitors (MIMCAPs) for use in analog and mixed signal (AMS) applications require ever-increasing capacitance density (C) while maintaining low leakage current density (J) and low nonlinearity (characterized by the quadratic voltage coefficient of capacitance, α_{VCC}), as projected by the International Technology Roadmap for Semiconductors (ITRS).[1] Scaling down the size of these MIMCAPs has proven challenging as C, J, and α_{VCC} are all inversely related to the dielectric thickness (d_{ox}).[2–4] AMS applications are particularly sensitive to α_{VCC}, which is determined empirically by fitting a parabolic expression to the capacitance vs. voltage measurement:

$$\Delta C/C_0 = \alpha_{VCC} V^2 + \beta_{VCC} V, \quad (6.1)$$

where C_0 is the capacitance density at 0 V, $\Delta C = C(V) - C_0$ is the change in capacitance at a given applied bias, and β_{VCC} is the linear voltage coefficient of capacitance. C_0 is characterized by the parallel plate capacitor equation, $C_0 = \frac{\varepsilon_0 \kappa}{d_{ox}}$, where ε_0 is the permittivity of vacuum and κ is the dielectric constant. It is well established that the "bulk" dielectric material has a dominant effect, where α_{VCC} increases with increasing dielectric constant and roughly with $1/d_{ox}^2$.[4–6] However, despite its technological importance, the fundamental mechanisms responsible for α_{VCC} are not fully understood. The mechanisms that have been proposed include non-linear metal-oxygen bond polarizability,[5,6] dielectric thermal expansion,[7] free carrier injection into oxygen vacancies creating a double layer,[8–12] and induced film strain from electrostriction and Maxwell stress.[3,13,14] Of the few studies that have considered the impact of the electrodes

on α_{VCC}, most have focused on interfacial layer oxides (ILOs).[8,9,12,3,13] Although they may play a substantial role when present, ILOs alone cannot fully explain the variation between electrodes. For example, metals that are unlikely to form significant oxides, those that have low enthalpy of oxide formation (ΔH_{ox}), still exhibit differing α_{VCC} values for the same dielectric.[9] Thus, in addition to ILOs, the metal electrodes themselves must exert an influence on α_{VCC}. An increased understanding of the role of the electrode interfaces in influencing α_{VCC} is needed to enable development and optimization of low α_{VCC} MIMCAPs for future technology generations.

In this work, metals with low ΔH_{ox} are used to examine the influence of the top electrode interface, in the absence of a significant ILO, on the nonlinearity of MIMCAPs with the same bottom electrode and atomic layer deposited (ALD) dielectrics of various thickness. Comparison is made with relatively high ΔH_{ox} Al electrode devices to look at the impact of ILOs on voltage nonlinearity. Finally, the observed dependence of α_{ECC} on electrode material and dielectric thickness is qualitatively explained with interfacial stress and metal-dielectric lattice mismatch.

6.2 Experimental

For the MIM devices used in this work, substrates of Si/SiO_2 (550 nm)/Ta (20 nm)/TaN (150 nm) with the TaN layer planarized via chemical mechanical polishing were provided by ON Semiconductor and used as the bottom electrodes. ALD of amorphous Al_2O_3 and HfO_2 thin films was performed in Picosun SUNALE R-200 and R-150 reactors, respectively, at a chamber temperature of 250°C using alternating N_2-purge-separated pulses of H_2O and either trimethylaluminum (TMA) or tetrakis[ethylmethylamino]hafnium (TEMA-Hf). The TMA source was at ~17°C and

TEMA-Hf was held at 90°C. The growth per cycle (GPC) of Al_2O_3 and HfO_2 were 0.92 nm/cycle and 0.77 nm/cycle, respectively. Au, Ag, Pd, Ni, and Al top metal electrodes were deposited via thermal evaporation. Film thickness was measured using a J.A. Woollam M2000 spectroscopic ellipsometer (SE) in the range of 400-1000 nm. Electrical measurements were taken using a B1500A semiconductor device parameter analyzer and an E4980A LCR meter. All electrical tests were conducted with the bottom electrode held at ground and performed in the dark at room temperature.

6.2 Results and Discussion

Shown in Fig. 6.1(a) is a plot of normalized capacitance (C/C_0) vs. voltage for TaN/Al_2O_3/Ag MIMCAPs with 10, 21, and 41.5 nm of Al_2O_3. In this figure, the linear baseline (β_{VCC} term from Eqn. 1) has been removed. ALD Al_2O_3 shows a positive α_{VCC} (C increases with V) value that increases in magnitude as dielectric thickness decreases, which is a trend commonly displayed by dielectric materials.[15–17] In theory, if nonlinearity is purely a "bulk" dielectric effect then normalizing using electric field (E), via the *electric field* coefficient of capacitance (α_{ECC}), should result in α_{ECC} values that are approximately constant for each d_{ox} of Al_2O_3. However, when the same data is plotted vs. E, as in Fig. 6.1(b), we find that α_{ECC} *decreases* with decreasing d_{ox}. This behavior is not predicted by existing models and indicates either (i) the presence of an ILO or (ii) the influence of a non-bulk interfacial mechanism.[3,5,7,10]

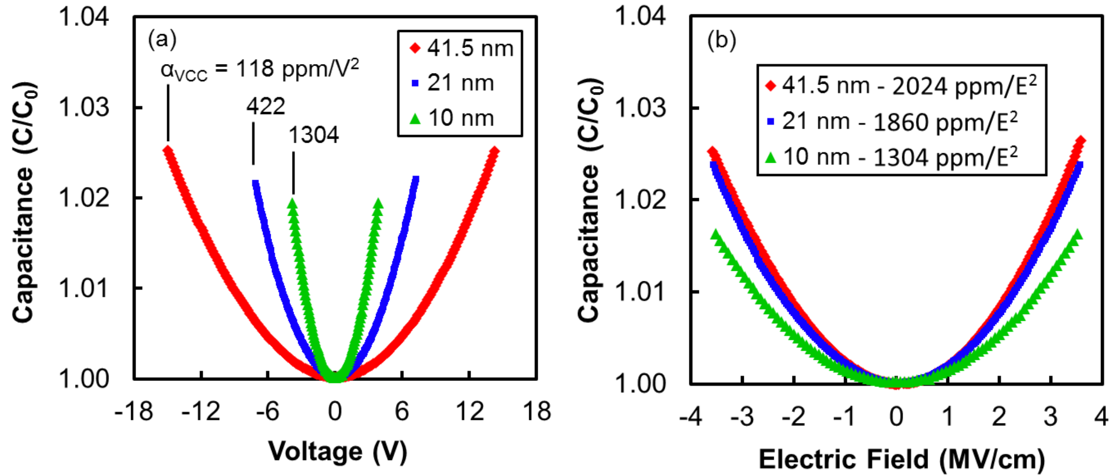

Figure 6.1: Baseline adjusted (β term removed) normalized capacitance density vs. (a) voltage and (b) electric field for various thickness Al_2O_3 devices with ~320 nm Ag top contacts.

A dielectric thickness dependence of α_{ECC} can be generated by an ILO. If the thickness of the hypothetical ILO stays relatively constant with respect to the thickness of the deposited dielectric, then the ILO acts as a constant series capacitance, with the total capacitance, C_{TOT}, calculated via:

$$C_{TOT} = \frac{C_d * C_{ILO}}{C_d + C_{ILO}}, \tag{6.2}$$

where C_d is the capacitance of the deposited dielectric and C_{ILO} is the capacitance of the ILO. To determine whether an ILO is present, the zero-bias capacitance equivalent oxide thickness (CET, defined as $\varepsilon_{SiO2}/C_{TOT}$) is plotted vs. the measured optical thickness in Fig. 6.2. Assuming a constant thickness ILO, the slope of this plot is proportional to the κ of the deposited dielectric and the y-intercept of a linear extrapolation indicates the CET of the ILO. The slope of a linear fit indicates $\kappa_{Al2O3} = 7.88$ and extrapolates approximately back to the origin, suggesting the absence of a *capacitive* ILO (any ILO that is present must be conductive and not contribute to capacitance).[18] Note that TaN was chosen as a lower electrode as it is commonly used in industry for MIM capacitors.

Within the temperature limits of BEOL processing, TaN is an effective diffusion barrier to copper, exhibits small metal diffusion into dielectrics, and displays relatively small changes in resistance when oxidized.[19–21] Therefore, any ILO that develops at the TaN interface is likely conductive. For the top electrode, ~320 nm of Ag is used. Ag has a very small ΔH_{ox} and should not introduce an ILO at the top interface.[22] Thus, the α_{ECC} dependence on d_{ox} observed in Fig. 6.1(b) is unlikely to be the result of an ILO at either electrode, but rather due to another interaction at the metal-dielectric interface.

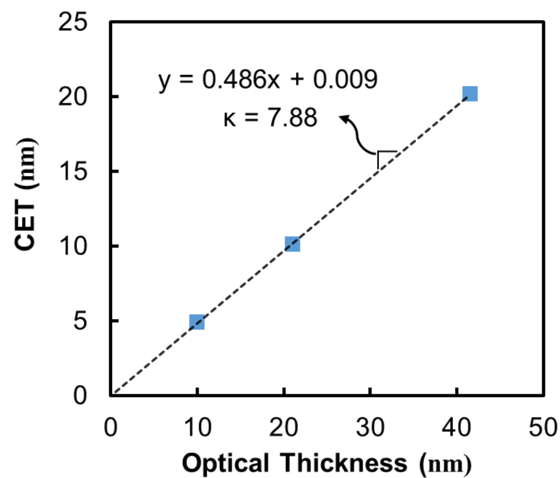

Figure 6.2: CET (zero-bias) versus measured optical thickness for TaN/Al_2O_3/Ag devices.

Shown in Fig. 6.3 are plots of α_{ECC} versus dielectric film thickness for ALD (a) Al_2O_3 and (b) HfO_2 with various ~320 nm thick low ΔH_{ox} metal electrodes. As nonlinearity scales linearly with κ, the ratio of α_{ECC} values between Al_2O_3 and HfO_2 is approximately equal to the ratio of their dielectric constants, ~8 and ~14, respectively.[3] As discussed above, if the interfaces do not play a role in determining nonlinearity, then α_{ECC} should be independent of d_{ox}. However, the influence of the metal-dielectric interface is clearly seen with α_{ECC} decreasing as d_{ox} decreases. Additionally, different

metals show different α_{ECC} values for the same d_{ox}. The influence of the metal-dielectric interface, indicated by the spread in α_{ECC} values between the various metals, is largest for the thinnest dielectrics and decreases with increasing d_{ox}. For the thickest dielectrics of both types, the dependence of α_{ECC} on d_{ox} saturates and the measured α_{ECC} values of the various metals are closely grouped, indicating reduced influence of the interfaces. As α_{ECC} decreases with decreasing dielectric thickness, the interfaces must be acting to oppose or mitigate α_{ECC} due to the dielectric bulk.

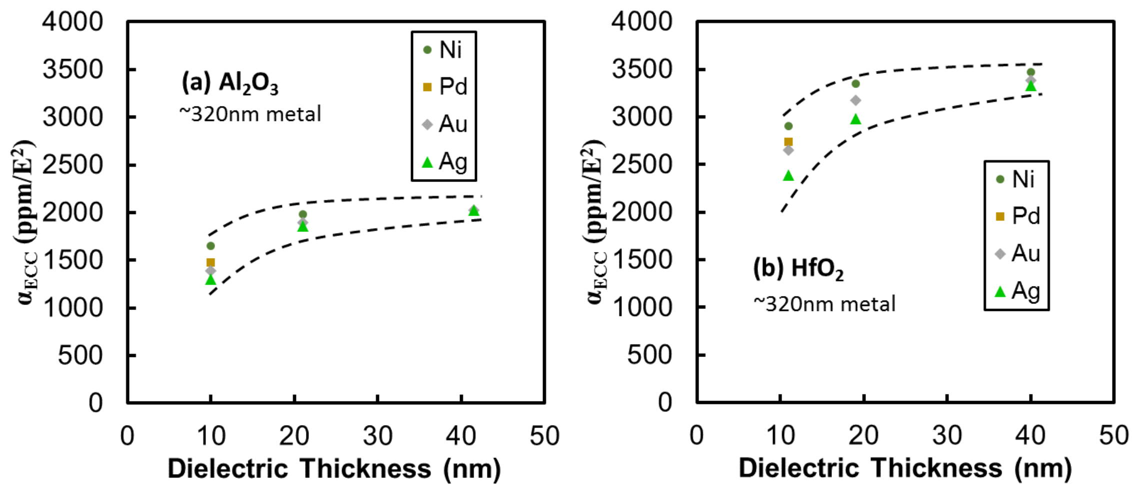

Figure 6.3: α_{ECC} versus dielectric film thickness for ALD (a) Al_2O_3 and (b) HfO_2 with various ~320 nm thick low ΔH_{ox} metal electrodes.

To further investigate the influence of the metal-dielectric interface and the spread in α_{ECC} values between the various metals, plots of C/C_0 versus E are shown in Fig. 6.4 for the devices with the thinnest dielectrics: (a) 10 nm Al_2O_3 and (b) 11 nm HfO_2. The α_{ECC} values for each metal are tabulated in the insets. The general trend observed for both Al_2O_3 and HfO_2 is the same, with Ag exhibiting the lowest α_{ECC}, followed in increasing order by Au, Pd, and Ni. Although there is no clear agreement in literature as to the detailed physical mechanisms responsible for α_{ECC}, a general feature of most models is that the nonlinear changes in capacitance are due to corresponding field induced elastic

changes in dielectric thickness, Δd_{ox}. The Δd_{ox} as a function of electric field may be calculated by modifying the parallel plate capacitor equation:

$$\Delta d_{ox}(E) = \frac{\varepsilon_0 \kappa_0 A}{C(E)} - d_{ox}(0\,V), \tag{6.3}$$

and is shown on the right axis of the plots in Fig. 6.4. Δd_{ox} values at 2.5 MV/cm are also tabulated in the insets. The ΔC observed for Ni at E = 2.5 MV/cm equates to an effective Δd_{ox} of ~1 Å for Al_2O_3 and ~2 Å for HfO_2, which again is roughly proportional to the ratio between their relative κ. The calculated Δd_{ox} range for the various metals is only ~0.2 Å for Al_2O_3 and ~0.3 Å for HfO_2 at 2.5 MV/cm, which corresponds to an α_{ECC} range of ~350 ppm/E^2 and ~500 ppm/E^2, respectively. We propose that the variation in α_{ECC} observed between the various low ΔH_{ox} metal electrodes in this study is due to an interaction between stress at the metal-oxide interface, caused by the decrease in bulk dielectric thickness, and physical differences between the metal electrodes.

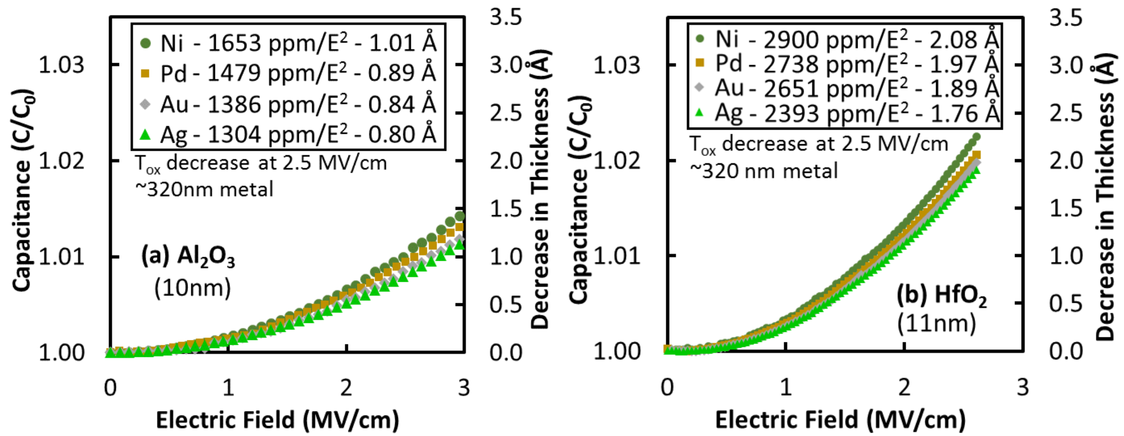

Figure 6.4: Normalized capacitance and calculated decrease in dielectric film thickness vs. electric field for (a) 10 nm Al_2O_3 and (b) 11 nm HfO_2 with various ~320 nm thick low ΔH_{ox} top metal electrodes.

One promising model for positive α_{ECC} materials that predicts an elastic decrease in d_{ox} with applied field was proposed by Wenger *et al.* and employs electrostriction

(displacement of ions in the lattice) and Maxwell stress (coulombic interaction of charge between electrodes).[3,23] Under an applied electric field, these mechanisms combine to create a vertical (out of plane) compressive stress which results in a decrease in d_{ox}. The Wenger / compression model is qualitatively consistent with the observation that α_{ECC} scales with κ (as seen in Figs. 6.3 and 6.4). The ionic bond strength is related to the κ through Coulomb's law. For a given electric field, ionic bonds in high-κ materials are more pliable and thus experience a greater change than bonds in lower κ materials, resulting in a greater Δd_{ox} and thus greater α_{ECC}.

The compressive deformation within a MIM capacitor for positive α_{VCC} dielectrics is illustrated in Fig. 6.5 with (a) zero-bias and (b) applied bias. We propose that in addition to vertical compression, the dielectric will attempt to expand horizontally in the x-y plane in order to maintain overall volume.[24,25] This horizontal expansion is not considered by Wenger et al. Deformation in non-crystalline solids is by viscous flow[25] and the horizontal (in-plane) expansion will be inhibited or opposed by the metal-oxide (or even oxide-oxide) interfaces.[22] This results in a horizontal in-plane compressive stress in the dielectric (illustrated by the dashed blue lines in Fig. 6.5) and a tensile stress in the metal, both concentrated near the interface.

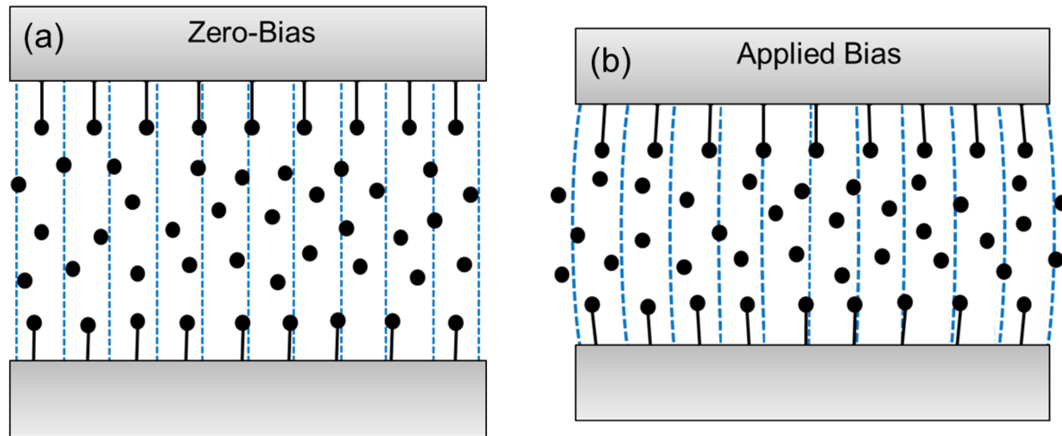

Figure 6.5: Cross sectional schematic illustrating elastic deformation (exaggerated) as result of applied bias to a positive α_{VCC} (α_{ECC}) dielectric. Dashed blue lines represent lateral expansion of the dielectric.

We further propose that restriction of the in-plane expansion in turn restricts the thickness reduction of the dielectric due to applied bias, effectively reducing α_{ECC}. Due to the dielectric stress being concentrated close to the interface, thinner films will exhibit a greater percentage of the dielectric being restricted to in-plane expansion than that of thicker films and thus show even less thickness reduction and further reduced α_{ECC}.[26] The α_{ECC} thickness dependence in Fig. 6.1(b) and Fig. 6.3, where thinner dielectrics show lower α_{ECC}, is consistent with this interpretation. Because Wenger *et al.* consider only the influence of ILOs, rather than the direct impact of the metal/oxide interfaces, they do not predict the thickness dependence of α_{ECC} we observe and cannot account for the differences observed between the various low ΔH_{ox} metals in this study.

Based on this interfacial expansion restriction model, we suggest that the variation in α_{ECC} among the low ΔH_{ox} metal electrodes is the result of differences in the lateral stresses within the dielectric near the electrodes. To explain the small α_{ECC} differences observed between Ag, Au, Pd, and Ni, we must consider the details of the individual

metal-dielectric interfaces. The inherent lattice mismatch present at hetero-interfaces may be characterized by a percent lattice mismatch (f),:

$$f \equiv \frac{a_d - a_m}{a_m}, \qquad (6.4)$$

where a_d and a_m are the dielectric and metal lattice constants, respectively.[27] In layers that exceed the necessary critical thickness to form an extra half plane of atoms, lattice mismatch typically results in edge dislocations near the interface that relieve strain and reduce surface energy.[26,27] The density of these defects is proportional to the percent lattice mismatch of the interface. Shown in Fig. 6.6 is a simple schematic of an interface between dissimilar materials. Edge dislocations result in localized compression zones (orange) in the smaller lattice constant material (metal electrode) and localized tension zones (blue) in the larger lattice constant material (dielectric). The stress in these localized zones is opposite to the global in-plane stresses induced by the out-of-plane compression of the dielectric and thus relieves or reduces some of the in-plane stress. Consequently, the differences in α_{ECC} among the low ΔH_{ox} metal electrodes in this study are likely the result of differences in cumulative stress relief due to differing densities of edge dislocations. It is expected that interfaces with increased defect density will experience increased stress relief, allowing more lateral expansion and thus more vertical compression of the dielectric which results in increased α_{ECC}. At the limit, this would mean that a dielectric with no restriction by the electrodes would exhibit the largest α_{ECC}, as there is no restriction to the in-plane expansion of the dielectric as it attempts to maintain volume under applied bias.

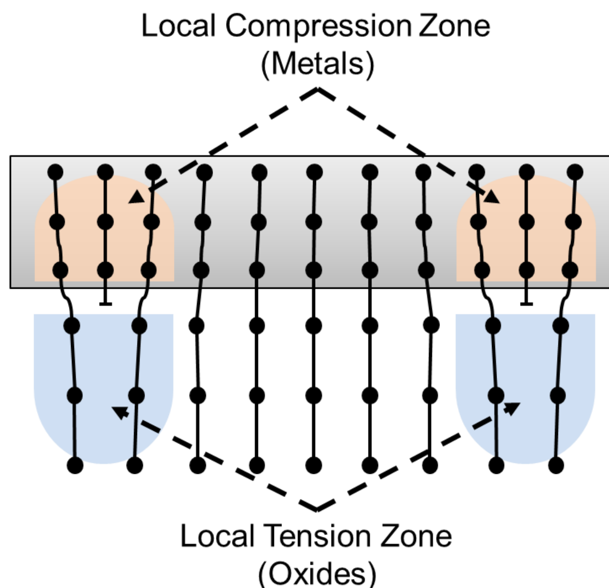

Figure 6.6: Schematic of residual stress and edge dislocations at a metal-oxide interface due to lattice mismatch.

Shown in Fig. 6.7 is a plot of α_{ECC} vs. f for Al_2O_3 and HfO_2 with Ag, Au, Pd, and Ni top metal electrodes. f and measured α_{ECC} values are tabulated in Table 6.1 for both Al_2O_3 and HfO_2 along with ΔH_{ox} for the metals used in this study.[28,29] For both Al_2O_3 and HfO_2, Ag exhibits the least f and smallest α_{ECC} value, followed by Au, Pd, and Ni in increasing order, revealing a direct correlation between f and α_{ECC} for low ΔH_{ox} metals.

For comparison, Al is also included in Fig. 6.7. Al fits the trend for Al_2O_3 but not for HfO_2. This is likely due to the relatively high ΔH_{ox} of Al, which in part drives the formation of an ILO. As discussed earlier, ILO layers can dominate overall α_{ECC}. Due to the high field dropped across a very thin ILO, the α_{VCC} contribution can be very large and lead to a very large overall device α_{ECC} (equation 6.2). Indeed, Vallée et al. reported that the α_{VCC} of HfO_2 and $BaTiO_3$ devices had roughly a direct relationship with the ΔH_{ox} of the metal electrodes, which is likely the result of ILO formation.[9]

For the case of HfO_2 in this work, α_{ECC} for the Al electrode devices is quite large due to the larger percentage of the electric field dropped across the thin reduced-k ILO formed at the Al/HfO_2 interface. For the Al_2O_3 devices, the formation of an Al_2O_3 ILO at the Al interface is limited[30] and any additional Al_2O_3 that does form will act as single dielectric with slightly increased dielectric thickness. Our results demonstrate that in the absence of ILO, the *f* can play a critical role in determining α_{ECC}, especially for the ultrathin dielectrics used for scaling in MIM capacitors for future ITRS nodes.

Table 6.1: *f*, α_{ECC}, and ΔH_{ox} for Al_2O_3 and HfO_2 for Various Metals Electrodes.

	f - Al_2O_3 (%)	α_{ECC} - Al_2O_3 (ppm/E^2)	*f* - HfO_2 (%)	α_{ECC} - HfO_2 (ppm/E^2)	Metal ΔH_{ox} (eV/Oxygen)
Ni	25.95	1653	31.11	2900	-2.53
Pd	18.25	1479	23.94	2738	-0.886
Al	*14.91*	*1357*	*20.84*	*3874*	*-5.8*
Au	14.31	1386	20.28	2651	-0.007
Ag	14.16	1304	20.14	2393	-0.311

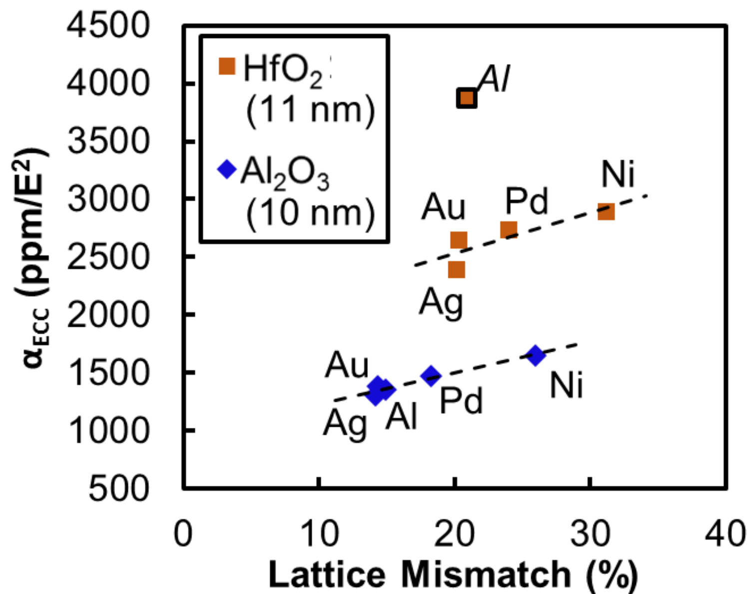

Figure 6.7: α_{ECC} vs. lattice mismatch for Al_2O_3 and HfO_2 with various top metal electrodes.

6.3 Summary and Conclusions

It is well established that α_{VCC}, the voltage coefficient of capacitance, increases with κ and with decreasing d_{ox}. Most current models of nonlinearity consider only the influence of the "bulk" dielectric and any ILOs that may be present and typically do not focus on the direct influence of the electrodes. These models predict that in the absence of an ILO, α_{ECC}, the electric field coefficient of capacitance, ought to be independent of d_{ox}. For all of the low ΔH_{ox} metals investigated in this study, we find that α_{ECC} actually *decreases* with decreasing d_{ox}. In addition, different α_{ECC} values are observed for each metal for otherwise identical device structures. Ag exhibits the lowest α_{ECC}, followed in increasing order by Au, Pd, and Ni. Differences between the metals become more pronounced as the dielectric thickness decreases. In order to explain these differences, one must consider the details of the metal/dielectric interfaces. For positive α_{VCC} materials, recent models predict that vertical compression of the dielectric under applied field is responsible for the increased capacitance. We propose that as the dielectric must also expand horizontally to maintain volume, this induces compressive stress in the dielectric and tensile stress in the metal, concentrated near the interface. We further propose that one of the roles of the electrode then is effectively to inhibit the lateral expansion of the dielectric and thus reduce overall α_{ECC}. In confirmation of this theory, the α_{ECC} values for both ~10 nm HfO_2 and Al_2O_3 are found to increase roughly linearly with the f of the metal/dielectric interfaces. The interfaces with higher mismatch contain a greater density of edge dislocations that provide increased localized stress relief, which results in a greater cumulative reduction in global interfacial stress and thus allows for increased lateral expansion of the dielectric under applied bias. Finally, a comparison was

made with high ΔH_{ox} Al electrodes. While Al fits the trend for Al_2O_3, due to the formation of a thin lower-k ILO at the HfO_2/Al interface, α_{ECC} is much higher than for the rest of the HfO_2 devices.

The ITRS roadmap requires α_{VCC} below 100 ppm/V^2. One way to achieve this is to use multiple dielectrics with complementary material properties, each targeting one or more device attributes.[2,4,31–35] Using this approach, increased C with low leakage J can be obtained while simultaneously minimizing α_{VCC} through the "cancelling effect".[2] The cancelling technique uses two or more dielectrics in a stack with at least one dielectric exhibiting a positive sign α_{VCC} and another exhibiting a negative sign α_{VCC}. By carefully controlling the thickness of each dielectric layer so that their individual contributions to α_{VCC} cancel one another, the overall device nonlinearity may be minimized. For the low ΔH_{ox} metals in this study, α_{ECC} increases with increasing d_{ox}, saturating for thick oxides. As thinner dielectrics are used to achieve higher C, the metal electrodes exert influence over a greater percentage of d_{ox}. We have shown that even for 10 nm dielectrics, the electrode can already influence α_{VCC} by more than 500 ppm/V^2, and therefore must be considered. Thus, although secondary to the dielectric properties and thickness, the electrodes will become more critical and strategies such as the canceling approach will become more difficult to implement.

This understanding of the impact of the metal electrodes on nonlinearity should aid in rapid scaling and optimization of low α_{VCC} MIMCAPs. The lattice mismatch and mechanical influence of the electrodes has not been considered previously and may light a path to future improvements in nonlinearity. For example, our results suggest that minimizing lattice mismatch between the dielectric and metal electrodes or mechanical

pinning the interface may be strategies worth investigating to produce highly scaled devices with ultra-low α_{VCC}.

6.4 Acknowledgments

The authors thank C. Tasker for equipment support, C. Remple, and J. Kittleman for assistance with thermal evaporation, and ON Semiconductor and the Oregon Nanoscience and Microtechnologies Institute (ONAMI) for partial financial support of this work. This work was conducted at the Materials Synthesis and Characterization (MaSC) Center, a National Nanotechnology Coordinated Infrastructure (NNCI) Northwest Nanotechnology Infrastructure (NWNI) user facility at the Oregon State University which is supported in part by the National Science Foundation (grant ECC-1542101) and Oregon State University.

6.5 References

[1] The International Technology Roadmap for Semiconductors (ITRS), On-Chip Passives Technology Requirements (Semiconductor Industry Association, 2013).

[2] S.J. Kim, B.J. Cho, M.-F. Li, S.-J. Ding, C. Zhu, M.B. Yu, B. Narayanan, A. Chin, and D.-L. Kwong, IEEE Electron Device Lett. 25, 538 (2004).

[3] C. Wenger, G. Lupina, M. Lukosius, O. Seifarth, H.-J. Müssig, S. Pasko, and C. Lohe, J. Appl. Phys. 103, 104103 (2008).

[4] D.Z. Austin, D. Allman, D. Price, S. Hose, and J.F. Conley Jr., IEEE Electron Device Lett. 36, 496 (2015).

[5] S. Bécu, S. Crémer, and J.L. Autran, Microelectron. Eng. 83, 2422 (2006).

[6] S. Bécu, S. Crémer, and J.-L. Autran, Appl. Phys. Lett. 88, 052902 (2006).

[7] S. Blonkowski, Appl. Phys. Lett. 91, 172903 (2007).

[8] F. El Kamel, P. Gonon, and C. Vallée, Appl. Phys. Lett. 91, 172909 (2007).

[9] C. Vallée, P. Gonon, C. Jorel, and F. El Kamel, Appl. Phys. Lett. 96, 233504 (2010).

[10] P. Gonon and C. Vallée, Appl. Phys. Lett. 90, 142906 (2007).

[11] S. Blonkowski, M. Regache, and A. Halimaoui, J. Appl. Phys. 90, 1501 (2001).

[12] S.D. Park, C. Park, D.C. Gilmer, H.K. Park, C.Y. Kang, K.Y. Lim, C. Burham, J. Barnett, P.D. Kirsch, H.H. Tseng, R. Jammy, and G.Y. Yeom, Appl. Phys. Lett. 95, 022905 (2009).

[13] C. Wenger, M. Lukosius, H.-J. Müssig, G. Ruhl, S. Pasko, and C. Lohe, J. Vac. Sci. Technol. B Microelectron. Nanometer Struct. 27, 286 (2009).

[14] C. Wenger, M. Lukosius, G. Weidner, H.-J. Müssig, S. Pasko, and C. Lohe, Thin Solid Films 517, 6334 (2009).

[15] M. Thomas, J. Piquet, A. Farcy, C. Bermond, J. Torres, T. Lacrevaz, B. Flechet, N. Casanova, C. Perrot, P. Caubet, and B. Chenevier, Microelectron. Eng. 82, 521 (2005).

[16] X. Yu, C. Zhu, H. Hu, A. Chin, M.F. Li, B.J. Cho, D.-L. Kwong, P.D. Foo, and M.B. Yu, IEEE Electron Device Lett. 24, 63 (2003).

[17] C.B. Kaynak, M. Lukosius, I. Costina, B. Tillack, C. Wenger, G. Ruhl, and S. Rushworth, Microelectron. Eng. 87, 2561 (2010).

[18] S.P. Pavunny, P. Misra, J.F. Scott, and R.S. Katiyar, Appl. Phys. Lett. 102, 252905 (2013).

[19] J.K. Chen, C.-H. Chan, S.-W. Kuo, and F.-C. Chang, Microelectron. Eng. 86, 414 (2009).

[20] H.C. Jiang, C.J. Wang, W.L. Zhang, and X. Si, Mod. Phys. Lett. B 24, 905 (2010).

[21] A.O. Ibidunni, Oxid. Met. 40, 5 (1993).

[22] C.T. Campbell, Surf. Sci. Rep. 27, 1 (1997).

[23] I. Krakovský, T. Romijn, and A. Posthuma de Boer, J. Appl. Phys. 85, 628 (1999).

[24] T. Vreeland, A. Dommann, C.-J. Tsai, and M.-A. Nicolet, MRS Proc. 130, (1988).

[25] W.D. Callister, *Materials Science and Engineering: An Introduction*, 7th ed (John Wiley & Sons, New York, 2007).

[26] M. Liu, H. Ruan, L. Zhang, and A. Moridi, J. Mater. Res. 27, 2737 (2012).

[27] J.E. Ayers, T. Kujofsa, P. Rango, and J.E. Raphael, *Heteroepitaxy of Semiconductors: Theory, Growth, and Characterization*, Second edition (CRC Press/Taylor & Francis Group, Boca Raton, 2017).

[28] Chemical Rubber Company and D.R. Lide, editors, *CRC Handbook of Chemistry and Physics: A Ready-Reference Book of Chemical and Physical Data*, 86. ed (CRC Press, Boca Raton, 2005).

[29] I. Barin, O. Knacke, and O. Kubaschewski, Thermochemical Properties of Inorganic Substances (Springer Berlin Heidelberg, Berlin, Heidelberg, 1977).

[30] M. He and T.-M. Lu, *Metal-Dielectric Interfaces in Gigascale Electronics* (Springer New York, New York, NY, 2012).

[31] J.-J. Yang, J.-D. Chen, R. Wise, P. Steinmann, Y.-C. Yeo, and C. Zhu, IEEE Electron Device Lett. 30, 1033 (2009).

[32] T.H. Phung, D.K. Srinivasan, P. Steinmann, R. Wise, M.-B. Yu, Y.-C. Yeo, and C. Zhu, J. Electrochem. Soc. 158, H1289 (2011).

[33] J.H. Lee, Y.C. Lin, B.H. Chen, and C.Y. Tsai, in *Solid-State Integr. Circuit Technol. ICSICT 2010 10th IEEE Int. Conf. On* (IEEE, 2010), pp. 1024–1026.

[34] C.-C. Lin, Y.-H. Wu, R.-S. Jiang, and M.-T. Yu, IEEE Electron Device Lett. 34, 1418 (2013).

[35] S.-U. Park, C.-Y. Kang, H.-M. Kwon, B.-S. Park, W.-H. Choi, I.-S. Han, G. Bersuker, R. Jammy, and H.-D. Lee, Microelectron. Eng. 88, 3389 (2011).

7 CONCLUSION

In this work, ALD of both dielectrics and metals have been investigated to develop complementary multi-insulator MIMCAPs to meet future ITRS requirements. Ultra-thin multi-insulator stacks of PEALD Al_2O_3/SiO_2 bi-layers deposited at 200ºC are found to meet ITRS projected requirements for the 2020 node. The insulator stack consisting of 3.7 nm Al_2O_3 and 1.9 nm SiO_2 exhibit a C_0 of 10.1 fF/µm^2, a leakage J of 6.8 nA/cm^2 at 1V, and an α_{VCC} of -20 ppm/V^2.[1] ALD for these ultra-thin insulators was critical for optimizing the α_{VCC} via the cancelling effect, due to its self-limiting reactions to precisely control film thickness. However, the scaling limit, via d_{ox} reduction, was determined to be the IRTS 2020 node, which drove the push for replacement complementary high-κ dielectrics and high work function metals to increase C while maintaining low J and low α_{VCC}.

Novel ALD processes for Bi_2O_3, Ru metal, and RuO_2 are characterized. Bi_2O_3 thin films using $Bi(OCMe_2{}^iPr)_3$ and H_2O show an ALD window between ~90°C to ~150°C with a single preferred crystal orientation of (201) of the β phase, independent of the underlying substrates.[2] Bi_2O_3 thin films deposited at 150°C showed the best film properties with a density of 8.3 g/cm^3, a band gap of 2.9 eV, a refractive index of 2.51 at 632 nm, and a linear GPC of 0.039 nm/cycle. Thus, ALD Bi_2O_3 using $Bi(OCMe_2{}^iPr)_3$ is a potential candidate in multi-component Bi based high-κ oxide thin films.

Zero oxidation state ALD Ru precursor, η^4-2,3-dimethylbutadiene ruthenium tricarbonyl [Ru(DMBD)$(CO)_3$] was investigated for suitability to grow both Ru metal and RuO_2 thin films.[3] Using thermal ALD with short 2 s pulses of O_2 resulted in a Ru metal saturating growth rate of 0.067 nm/cycle with negligible nucleation delay within an ALD temperature window of 290 to 320°C. Ru metal exhibited a strong hexagonal

crystal structure with a low resistivity of ~14 μΩ·cm at 320°C and a smooth surface roughness of ~0.6 nm for 8 nm thick films. Then using longer 20 s O_2 pulses and lower temperatures, RuO_2 thin films were deposited by both thermal and PEALD using O_2 or O_2 plasma, respectively. However, the thermal ALD RuO_2 process generally exhibited better film properties due oxygen plasma of PEALD likely etching RuO_2 during deposition. The thermal ALD RuO_2 exhibited a linear GPC of 0.065 nm/cycle with low nucleation delay on SiO_2 of 35 cycles within the ALD deposition window of 220 to 240°C. Additionally, RuO_2 films grown by thermal ALD show distinct rutile phase microstructure, resistivity of ~62 μΩ·cm, density close to bulk of 7.91 g/cm^3, and RMS roughness of 0.6 nm for 12 nm thick films. Thus, thermal ALD of both Ru and RuO_2 thin films using Ru(DMBD)$(CO)_3$ precursor is promising for MIMCAPs as metal electrode materials. Although RuO_2 exhibits increased resistivity over Ru metal, due to the rutile phase and ability to template the high-k phase of rutile TiO_2, RuO_2 is of primary interest in multi-insulator MIMCAPs.

Building off the previous work, complementary multi-insulator bilayers of PEALD TiO_2/Al_2O_3 were investigated. Initially, 400 cycle PEALD TiO_2 via $TiCl_4$ and O_2, deposited at 400°C and then annealed at 400°C for 30 min in O_2, exhibited rutile TiO_2 on RuO_2 while anatase TiO_2 on TaN. Additionally, 400 cycle PEALD TiO_2 showed an order of magnitude less leakage J as well as increased C_0 of ~37.5 fF/μm^2 ($\kappa \approx 89$) with a negative α_{VCC} of approximately -35,000 ppm/V^2 on RuO_2 versus ~28.5 fF/μm^2 ($\kappa \approx 52$) with a positive α_{VCC} of approximately 29,000 ppm/V^2 on TaN. Then continuing with the RuO_2 lower electrode, TiO_2/Al_2O_3 MIMCAP with d_{ox} of ~21 nm and ~5 nm is demonstrated to achieve high C_0 of 14.3 fF/μm^2 with an α_{VCC} of ~450 ppm/V^2 and low

leakage J at 1 V of 8.7 nA/cm^2. However, the α_{VCC} is found to be difficult to characterize due to a higher order polynomial fit, or "w" shape. Additionally, the C_0 is found to be unstable with time, likely due to rutile TiO_2 morphology changing to a reduced κ phase. Although despite reduced κ, the device tested after stabilizing to a lower C_0 met the ITRS 2020 node projected requirements with C_0 of 10.4 fF/μm^2, a leakage J of 7.11 nA/cm^2 at 1V, and an α_{VCC} of -45 ppm/V^2.

Finally, to examine the mechanism of the influence from the top metal electrode on α_{VCC}, in the absence of an ILO, various low ΔH_{ox} metals are investigated as a function of d_{ox} with ALD Al_2O_3 and HfO_2. When normalizing for d_{ox} via electric field, it is found for each low ΔH_{ox} metal that a different α_{ECC} value is measured, for an otherwise identical device structure. For both Al_2O_3 and HfO_2 dielectrics, Ag exhibits the lowest α_{ECC}, followed in increasing order by Au, Pd, and Ni. Additionally, the difference between these metals becomes more pronounced as the d_{ox} decreases, which indicates a non-negligible interface interaction between the metal and dielectric. Thus, to explain these differences in positive α_{VCC} materials, we propose a vertical compression of the dielectric, due to applied bias, and an expansion in-plane of the dielectric to maintain volume that is restricted by the metal electrodes, which results in a concentrated stress near the interface. Therefore, modulation of α_{ECC} is likely to occur due to differences in density of edge dislocations from lattice mismatch between metal and dielectric. Edge dislocations provide increased localized stress relief and greater cumulative reduction in global interfacial stress, which allows for increased lateral expansion of the dielectric under applied bias. The trend measured between α_{ECC} values for each metal and percent lattice mismatch between metal and dielectric points to a mechanical pinning at the

interface which is reduced by edge dislocations and significantly modulates voltage nonlinearity, in the absence of an ILO. Additionally, Al, a high ΔH_{ox} metal, is found to fit the trend for Al_2O_3 but not for HfO_2, which is due to the formation of a thin Al_2O_3 ILO at the HfO_2/Al interface. This new understanding of the impact from metal electrodes on nonlinearity should aid in rapid scaling optimization of low α_{VCC} MIMCAPs.

7.1 References

[1] D.Z. Austin, D. Allman, D. Price, S. Hose, and J.F. Conley Jr., IEEE Electron Device Lett. 36, 496 (2015).

[2] D.Z. Austin, D. Allman, D. Price, S. Hose, M. Saly, and J.F. Conley Jr., J. Vac. Sci. Technol. Vac. Surf. Films 32, 01A113 (2014).

[3] D.Z. Austin, M.A. Jenkins, D. Allman, S. Hose, D. Price, C.L. Dezelah, and J.F. Conley Jr., Chem. Mater. 29, 1107 (2017).